

**Computational Studies of Olefin Polymerization and Hydroboration with *N*-Heterocyclic
Carbene Boranes**

by

Cheng Fang

B.Sc, China Pharmaceutical University, 2008

M.Sc, Peking Union Medical College & Tsinghua University, 2011

M.Sc, University of Pittsburgh, 2014

Submitted to the Graduate Faculty of
the Kenneth P. Dietrich School of Arts and Sciences in partial fulfillment
of the requirements for the degree of
Doctor of Philosophy

University of Pittsburgh

2019

UNIVERSITY OF PITTSBURGH
DIETRICH SCHOOL OF ARTS AND SCIENCES

This thesis was presented

by

Cheng Fang

It was defended on

February 26, 2019

and approved by

Krzysztof Matyjaszewski, J.C. Warner University Professor of Natural Sciences,
Department of Chemistry, Carnegie Mellon University

John Keith, Assistant Professor, Department of Chemical & Petroleum Engineering

Geoff Hutchison, Associate Professor, Department of Chemistry

Thesis Advisor: Peng Liu, Assistant Professor, Department of Chemistry
& Department of Chemical & Petroleum Engineering

Copyright © by Cheng Fang

2019

Computational Studies of Olefin Polymerization and Hydroboration with *N*-Heterocyclic Carbene Boranes

Cheng Fang, Ph.D

University of Pittsburgh, 2019

Alkenes and alkynes are two commonly starting materials to produce various valuable chemicals and bioactive organic compounds. Several chemical transformations with alkenes and alkynes will be discussed in this thesis, including copper-catalyzed and photoredox-mediated atom transfer radical polymerization (ATRP), selectivity-enhancement entropy-driven ring opening metathesis polymerization (SEED-ROMP) and hydroboration of alkynes using *N*-heterocyclic carbene (NHC) boranes. Although there are tremendous advances in the development of ATRP, the detailed mechanisms for the key steps in ATRP are not fully explored. Also, it remains challenging to investigate the catalysts and initiators effects on the ATRP reactivity. In this thesis, I applied multiple computational approaches, including DFT calculations, Marcus theory calculations, energy decomposition analysis, and multivariate linear regression, to investigate the mechanism and the catalysts and initiators effects in ATRP. Our computational studies revealed that copper-catalyzed ATRP occurs via an inner-sphere electron transfer transition state in activation/deactivation process. Detailed analysis of the ATRP transition states suggested key factors controlling the reactivities of catalysts and initiators, which were further utilized to establish predictive models for the catalyst and initiator effects via a multivariate regression approach. On the other hand, the photoredox-mediated ATRP prefers an outer-sphere electron transfer mechanism in activation/deactivation process. Furthermore, although the mechanism for ROMP is well-established, it is unclear regarding the origin of the selectivity for *cis*-macrocylic

olefin monomers over *trans*-monomers in SEED-ROMP. By integrating DFT calculations and molecular dynamics simulation, it is suggested that enhanced polymerization reactivity was due to the *cis*-macrocyclic olefin being less flexible and having a larger population of metathesis-reactive conformers. In addition, I applied DFT calculations and quasi-classical Born-Oppenheimer molecular dynamics simulations to investigate the mechanisms, dynamics effect, and the origin of reactivities and chemoselectivities in the hydroboration of alkynes and arynes with NHC-borane. Our calculations revealed that the hydroboration of alkynes occurs through a *trans*-selective hydride transfer process followed by a bifurcation pathway leading to both *trans*-alkenylborane and *trans*-borirane products. The hydroboration of arynes is a dynamically-stepwise hydride transfer process, in which the hydride prefers to attack more positively charged and more linear *sp*-hybridized carbons in substituted arynes, leading to the high levels of regioselectivity.

Table of Contents

ACKNOWLEDGEMENTS	xv
1.0 INTRODUCTION.....	1
1.1 Background	1
1.2 Computational Approaches	3
1.2.1 Density functional theory (DFT) calculations	3
1.2.2 Implicit solvation models	6
1.2.3 Marcus theory calculations	7
1.2.4 Molecular dynamics (MD) simulation.....	8
1.2.5 Energy decomposition analysis (EDA)	9
1.2.6 Multivariate linear regression.....	9
1.3 Summary	10
2.0 MECHANISTICALLY GUIDED PREDICTIVE MODELS FOR LIGAND AND INITIATOR EFFECTS IN COPPER-CATALYZED ATOM TRANSFER RADICAL POLYMERIZATION (Cu-ATRP)	12
2.1 Introduction	12
2.2 Computational methods	15
2.2.1 DFT calculations	15
2.2.2 Marcus Theory Calculations.....	16
2.3 Results and Discussion	19
2.3.1 Activation mechanisms in Cu-ATRP	19
2.3.2 Predictive Model for Initiator Effects on Reactivity	25

2.3.3 Predictive Model for Ligand Effects on Reactivity	28
2.3.3.1 Ligand electronic effect	29
2.3.3.2 Ligand Steric Effect.....	31
2.3.3.3 Ligand Backbone Flexibility Effect.....	33
2.3.3.4 Predictive model for ligand effect on reactivity	36
2.4 Conclusion	39
3.0 COMPUTATIONAL STUDY ON THE MECHANISM OF PHOTO-INDUCED METAL-FREE ATOM TRANSFER RADICAL POLYMERIZATION (<i>photo</i>ATRP)	41
3.1 Introduction	41
3.2 Computational Methods	43
3.2.1 DFT calculations	43
3.2.2 Marcus Theory Calculations.....	44
3.3 Results and Discussion	49
3.3.1 Activation Mechanism	49
3.3.2 Structures and stabilities of intermediates $Cat^{\bullet+}$ and $Cat^{\bullet+}X^-$	50
3.3.3 Benchmark calculations of dissociation energy of $2^{\bullet+}Br^-$	53
3.3.4 Deactivation Mechanism	55
3.3.5 Computed Barriers for Deactivation Processes with Different Catalysts....	58
3.4 Conclusion	60
4.0 COMPUTATIONAL STUDY ON <i>CIS</i>-SELECTIVE ENTROPY-DRIVEN RING-OPENING METATHESIS POLYMERIZATION OF MACROCYCLIC OLEFINS TOWARDS SEQUENCED POLYMERS	61

4.1 Introduction	61
4.2 Computational Methods	64
4.2.1 DFT calculations	64
4.2.2 Molecular Dynamics simulations.....	64
4.3 Results and Discussion	65
4.3.1 Deviation of Macromonomer's Conformation from Reactive Olefin Geometry.....	65
4.3.2 Estimation of Activation Energies of [2+2] Cycloaddition with Different Conformers of <i>cis</i> - and <i>trans</i> -Macromonomers	67
4.4 Conclusion	70
5.0 COMPUTATIONAL STUDY ON THE MECHANISMS, DYNMACIS, AND THE ORIGIN OF REACTIVITY AND SELECTIVITY OF HYDROBORATION OF AKYNES AND ARYNES WITH N-HETEROCYCLIC CARBENE BORANES (NHC-BORANES)	72
5.1 Introduction	72
5.2 Computational Methods	74
5.3 Results and Discussions.....	75
5.3.1 Bifurcation Trajectory of Acetylenedicarboxylate Hydroboration with NHC-Borane	75
5.3.2 Formation of <i>cis</i> -alkenylborane and borirane and the origin of <i>trans</i> - selectivity	81
5.3.3 Other mechanisms in acetylenedicarboxylate hydroboration	83
5.3.4 Mechanisms of the hydroboration of benzyne with NHC-boranes	88

5.3.5 Molecular dynamics of the hydride transfer mechanism: concerted or stepwise?	95
5.3.6 Regioselectivity for substituted aryne hydroboration with NHC-boranes ..	98
5.3.7 Reactivity difference between alkynes and arynes.....	103
5.4 Summary	105
PUBLICATION LIST	107
PRESENTATION LIST (SELECTED).....	109
REFERENCES.....	111

List of Tables

Table 1-1 DFT methods and solvation models used in different projects of this thesis	5
Table 2-1 Electronic effects of the TPMA family ligands. ^a	30
Table 2-2 Steric effects of the TREN family ligands ^a	32
Table 2-3 Flexibility effects of the Cyclam family ligands ^a	34
Table 2-4 Calculated electronic (E_{HOMO}), steric ($V_{\text{bur}}\%$), and backbone flexibility (ΔE_{dist}) parameters for all 18 ligands ^a	38
Table 3-1 Thermodynamic, kinetic and geometric parameters for the homogenous electron transfer to R-X.....	45
Table 3-2 Parameters used for the determination of energy barriers for the deactivation pathways.	47
Table 3-3 Computed reaction energies, and activation free energies in the activation process, with the existed catalysts, 2*, 3*, and 4*.....	50
Table 3-4 The relative stabilities of $2^{\bullet+}\text{Br}^{-}\text{-C}$ and $2^{\bullet+}$ at different levels of theory.	55
Table 3-5 Computed activation energies for possible deactivation pathways in metal-free ATRP with photoredox catalysts 2, 3, and 4.....	58
Table 5-1 Calculated pre-distorted angles and charges for C-1 and C-2 in arynes*	102

List of Figures

Figure 2-1 Ligand effects on the activation/deactivation of Cu-ATRP	13
Figure 2-2 Workflow of establishing predictive models for reactivity of Cu-ATRP catalysts	15
Figure 2-3 Computed energy profiles of Cu-ATRP activation pathways in MeCN at 25 °C with tris(2-pyridylmethyl)amine (TPMA) ligand	20
Figure 2-4 Optimized geometries, energies, Mulliken charges, and spin densities of computed structures in the ISET pathway	22
Figure 2-5 The origin of the bent geometry in TS1	23
Figure 2-6 Optimized geometries of ISET TS of 15 initiators with $[\text{Cu}^{\text{I}}(\text{TPMA})]^+$ catalyst. The initiators highlighted in blue are reported in Section 2.3.2.....	24
Figure 2-7 Initiator effect in Cu-ATRP with the Cu^{I} -TPMA catalyst	26
Figure 2-8 Correlation of distortion energies with experimental reactivities of alkyl halide initiators	26
Figure 2-9 Correlation of interaction energies (ΔE_{int}) with experimental reactivities of alkyl halide initiators	26
Figure 2-10 Predictive model for initiator reactivity in Cu-ATRP.....	27
Figure 2-11 Representative ligands for Cu-ATRP catalyst. Experimentally k_{act} are provided in parentheses.....	29
Figure 2-12 Optimized geometries of ISET transition states with TPMA family ligands	30
Figure 2-13 Correlation of experimental reactivities and the HOMO energies of five $[\text{Cu}^{\text{I}}\text{L}]^+$ catalysts with TPMA family ligands.....	31
Figure 2-14 Optimized geometries of ISET transition states with TREN family ligands	32

Figure 2-15 Optimized geometries of Cu ^I catalysts and ISET transition states with Cyclam family ligands	35
Figure 2-16 Correlation of $\Delta E_{\text{dist(TS)}}$ and $\Delta E_{\text{dist(BrCu II}_L)}$ for 9 ligands in the training set	35
Figure 2-17 Predictive model for ligand effect on Cu-ATRP reactivity	36
Figure 3-1 Structures of photoredox catalyst 1 and 2 and a Cu-catalyzed ATRP catalyst 3	42
Figure 3-2 Simplified activation/deactivation mechanism for photoredox-mediated ATRP reactions	42
Figure 3-3 The structures, ATRP reactivities, and the dispersity of polymerization for representative photoredox catalysts.	43
Figure 3-4 ^a Optimized geometries of the radical cation $2^{\bullet+}$ and the zwitterionic radical complex $2^{\bullet+}\text{Br}^-$	52
Figure 3-5 HOMO, spin densities, NPA charges, and Wiberg bond indices of $\text{Cat}^{\bullet+}\text{X}^-$	53
Figure 3-6 Possible deactivation mechanisms in photoinduced metal-free ATRP.....	56
Figure 3-7 Computed reaction energy profiles for the reaction of $2^{\bullet+}\text{Br}^-$ -C with MMA^\bullet	57
Figure 3-8 Homolytic cleavage of the $11^{\bullet+}\text{Br}^-$ complex indicates the instability of $4^{\bullet+}$	59
Figure 4-1 Advantages of SEED-ROMP Preparation of Sequenced Polyesters Relative to ED-ROMP	62
Figure 4-2 <i>Cis</i> -Selective Ring-Closing Metathesis and SEED-ROMP to Generate a Sequenced Copolymer.....	62
Figure 4-3 Computational study on the conformations and reactivity of <i>cis</i> - and <i>trans</i> -macromonomers. (A) Optimized transition states of model substrates. (B) Molecular dynamic simulations of <i>cis</i> - and <i>trans</i> -macromonomers. (C) Representative active and inactive conformers of <i>cis</i> - and <i>trans</i> -macromonomers.	66

Figure 4-4 Estimantion of Activation Energies for Macromonomer's Conformation in ROMP .	68
Figure 5-1 Hydroboration of alkynes and arynes with boranes and NHC-boranes	73
Figure 5-2 Hydroboration of acetylenedicarboxilate with Me-substitued NHC-borane	76
Figure 5-3 Favorable mechanim of the formation of alkenylborane and borirane.	76
Figure 5-4 Snapshots of BOMD trajectory simulations of the reaction of 1 and 2	79
Figure 5-5 Structures used in the normal model sampling to generate initial geometries for the BOMD trajectory simulations.....	80
Figure 5-6 Mechanism of formation of alkenylborane and borirane without explicit THF molecule	81
Figure 5-7 Mechanism of <i>cis</i> -selective hydride transfer.....	82
Figure 5-8 Optimized geometries of <i>trans</i> - and <i>cis</i> -selective hydride transfer transtion states....	82
Figure 5-9 Proton transfer-borylene cycloaddition pathway of the formation of borirane.....	83
Figure 5-10 Optimized geometry of the proton transfer transition states TS3 and TS3•THF	84
Figure 5-11 Interconversion between alkenylorane and borirane.....	85
Figure 5-12 Optimized geometry of transition states and intermediates in the 1,2-hydride transfer pathway	85
Figure 5-13 <i>Cis/trans</i> isomerization of alkenyl anion 11 is not likely to compete with boronium addition	87
Figure 5-14 Hydroboration of benzyne with diMe-substitued NHC-borane.....	88
Figure 5-15 Possible mechanisms of the hydroboration of benzyne with NHC-boranes	89
Figure 5-16 Calculated energy profile for hydride transfer mechanisms in benzyne hydroboration	91

Figure 5-17 Optimized geometries of transition states and intermediates involved in hydride transfer mechanism of the benzyne hydroboration.....	91
Figure 5-18 Intrinsic reaction coordinate (IRC) plot for the concerted transition states of benzyne hydroboration.....	92
Figure 5-19 Theoretical calculation of KIE for benzyne hydroboration with NHC-borane.....	93
Figure 5-20 Unfavored pathways that involved the dissociation of 13	94
Figure 5-21 Two representative trajectories from BOMD simulation for TS7-C and TS7-SW ..	97
Figure 5-22 The distribution of bond formation timing for trajectories propagated from TS7-C and TS7-SW.....	98
Figure 5-23 Hydroboration of various arynes with NHC-borane.....	99
Figure 5-24 Competing transition states for hydroboration of 3-OMe benzyne (17) and 3-Me benzyne (19).....	101
Figure 5-25 The correlation of the difference in activation barriers ($\Delta\Delta G^\ddagger$) with the difference in pre-distorted angles (ΔL) and charges (ΔQ) of ground state arynes.....	103
Figure 5-26 Calculated energy profiles for the hydroboration of benzyne, acetylenedicarboxylate, and 2-butyne with NHC-borane.....	104

ACKNOWLEDGEMENTS

First of all, I would like to sincerely thank my supervisor, Prof. Peng Liu, for his guidance and continuous support in my PhD study at Pitt. It is very fortune and grateful for me to work with him in the past five years. I learnt and benefited a lot from close interactions with him, in particular, hot to think things deep but interpret them at a high-level. My PhD experience under Prof. Peng Liu's mentorship will definitely have a great impact on my future independent career development.

I would like to thank all of my collaborators, especially Prof. Krzysztof Matyjaszewski, and Prof. Dennis Curran for insightful discussions in our multiple collaborative projects, and their kind support in my fellowship applications. I would also like to thank Prof. Michelle Coote, Prof. Tara Meyer, Prof. Joseph Ready, Prof. Ting Wang, Prof. Jianglong Zhu, Prof. Stephen Buchwald, and Prof. Guangbin Dong, and Dr. Marco Fantin and Dr. Xiangcheng Pan from Matyjaszewski group, and Dr. Timothy McFadden from Curran group.

I will appreciate the help and kind support from all the fellows in Prof. Peng Liu's group. Especially, I would to thank Dr. Gang Lu and Dr. Xiaotian Qi for all insightful discussions.

I would like to thank the computational modeling and simulation PhD program. Appreciate the help and support from the director Prof. Ken Jordan, and the coordinators Christie Hay and Wendy Janocha.

I will appreciate the financial support from Andrew Mellon Fellowship, Arts and Science Fellowship, PQI Award, and ACS Outstanding Poster Award.

Finally, I would especially like thank my parents, and my dear girlfriend, Dr. Jieni Xu, for their love and support.

1.0 INTRODUCTION

1.1 Background

Alkenes and alkynes are two commonly used types of starting materials for the production of various valuable chemicals and organic compounds for biomedical research. Two types of chemical transformations with alkenes and alkynes will be discussed in this thesis, including olefin polymerization and the hydroboration of alkynes with *N*-heterocyclic carbene (NHC) boranes.

Olefin polymerization has been long time used to produce polyolefins in over 300 different commercial products, which accounts for half of the global plastics production.^{1, 2} Since Ziegler and Natta shared the Nobel Prize in Chemistry in 1963 for their discovery of olefin polymerization catalysts,³ the discovery of novel and better transition-metal catalyzed systems has become the major driving forces in the field of olefin polymerization. For instance, atom transfer radical polymerization (ATRP), as a powerful controlled radical polymerization technique, has shown a great impact on the synthesis of macromolecules with well-controlled compositions and architectures. ATRP can be catalyzed by both transition-metal catalysts and photoredox catalysts, and it is compatible with a variety of initiators and monomers. Another widely employed olefin polymerization reaction is ruthenium-catalyzed ring-opening metathesis polymerization (ROMP), which often utilizes the release of ring strain energy as the driving force. Recently, entropy-driven ROMP (ED-ROMP) and selectivity-enhanced ED-ROMP (SEED-ROMP) have been successfully developed to polymerize strainless macrocyclic olefins for sequence-controlled polymers.

Although tremendous developments have been made in the field of olefin polymerization, in particular with ATRP and ROMP, there are still several challenges that impede the design and discovery of better catalysts for olefin polymerization:

1. Insufficient mechanistic understanding of olefin polymerization. Copper-catalyzed ATRP (Cu-ATRP) is the first developed ATRP system, involving the halogen atom transfer between the initiator and the catalyst to complete activation and deactivation. However, this atom transfer transition state has not been explored by computation so far. On the other hand, photoredox-mediated ATRP (*photo*ATRP) has been discovered in recent years. The mechanism for *photo*ATRP is still unveiled, which hinders the investigation of the structure-reactivity relationship for photoredox catalysts in ATRP.

2. The lack of predictive models for catalyst effect in olefin polymerization. Over decades of development, there are a diverse set of catalysts available for olefin polymerization, especially for Cu-ATRP. But there is no efficient and insightful predictive model for the reactivity of catalysts. The lack of the predictive model makes it difficult to better understand how the perturbation of catalyst structure would affect the reactivity.

3. The origin of the effect of initiators and monomers is unclear in olefin polymerization. Cu-ATRP is compatible with a variety of initiators, which covers a wide range of reactivities. But the origin of the initiator effect on reactivity is not clear. On the other hand, although the mechanism for ROMP is well-established, the enhanced selectivity of *cis*-macrocyclic olefins over *trans*-monomers in ED-ROMP is still unknown.

In addition to olefin polymerization, the hydroboration of alkynes and arynes with NHC-boranes is also investigated in this thesis. NHC-boranes have striking reactivity difference from simple boranes in the hydroboration of π bonds. For example, NHC-boranes are able to

hydroborate the electron-deficient alkynes and various arynes, but don't react with electron-rich alkynes. Most interestingly, the hydroboration of alkynes with NHC-boranes shows unexpected *trans*-product selectivity, and it generates unusual *trans*-boriranes products. Also, the hydroboration of substituted arynes with NHC-boranes shows high levels of regioselectivities.

1.2 Computational Approaches

In this thesis, I applied multiple computational approaches, including density functional theory (DFT) calculation, Marcus theory calculation, classical molecular dynamics (MD) simulation, Born-Oppenheimer molecular dynamics (BOMD) simulation, and energy decomposition analysis (EDA), to investigate the mechanisms, dynamics, the origin of reactivity and selectivity for aforementioned chemical transformations of alkenes and alkynes. In the meantime, the multivariate linear regression was applied to establish predictive models for the catalyst and initiator effects on reactivity in Cu-ATRP, which facilitates rational catalyst design for Cu-ATRP, and can be extended to other transition metal-catalyzed reactions.

1.2.1 Density functional theory (DFT) calculations

Density functional theory (DFT) is a commonly-used quantum mechanical modeling method in computational chemistry to investigate the electronic structures of many-body systems.^{4,5} Specifically, DFT has generally been the method of choice for the mechanistic investigation of organic and organometallic chemical reactions due to an adequate balance between computational speed and accuracy.^{6,7}

Over decades of development, a variety of DFT methods are available for geometry optimizations of ground states and transition states, as well as properties and energy calculations. Although there is no universal method suitable for all investigated systems, there is indeed a group of methods that dominates in the field of organic and organometallic reaction calculations in terms of both geometry optimizations and energy calculations.⁷

1. Geometry optimizations. The B3LYP⁸ functional is still in extensive usage in geometry optimizations⁷ with its proven overall good performance across a wide range of systems.⁹ However, since B3LYP doesn't account well for dispersion interactions,¹⁰ a couple of newer dispersion-correction methods, including Minnesota functionals¹¹ (M06, M06L, M06-2X) and range-separated functional (ω -B97XD¹²), become popular in recent years especially when the van der Waals force or London dispersion force is significant for intermolecular or intramolecular interactions in the system. It is noted that M06-2X¹¹ doesn't work well for organometallic systems since it doesn't include the transition metal chemistry experimental data in the parameterization of its functional. In addition, the double-zeta Pople basis set¹³ (e.g. 6-31G(d)) is the most commonly used basis set for main-group atoms in geometry optimization, and the LANL2DZ¹⁴ and Stuttgart-Dresden (SDD)¹⁵ are the most frequently employed effective core potential (ESP) for heavy atoms such as Cu, Ru, etc.

2. Energy calculations. Given the fact that the B3LYP functional might systematically underestimate reaction barrier heights by about a few kcal/mol,¹⁶ and it performs poorly for noncovalent interactions governed by van der Waals attractions,¹⁷ an increasing usage of dispersion-corrected functionals, such as M06, M06L, M06-2X, ω -B97XD, in the energy calculations are witnessed in recent references. In addition, the triple-zeta Pople basis set with diffuse functions (e.g. 6-311++G(d,p)) is commonly used for main-group atoms in energy

calculations, and the ESP of SDD is becoming more popular than LANL2DZ for heavy atoms since SDD offers more flexibility in the valence shell.

Table 1-1 shows the DFT methods used in different projects covered by this thesis. In Chapter 2, given the significant nonbonding interactions between the catalyst and the substrate in the Cu-ATRP transition state, the functional ω -B97XD, which takes medium-range and long-range interaction into account, was applied in both geometry optimizations and energy calculations. Also, the triple-zeta basis set (def2-TZVP¹⁸) was employed in energy calculations. In Chapter 3, the B3LYP/6-31G(d) method was used in geometry optimization. But more accurate functional M06-2X with large basis set 6-311++G (3df, 2p) was used in energy calculation to capture the difference between Br and Cl substrates. In Chapter 4, since the goal of the DFT study was to obtain the geometry of the Ru-catalyzed [2+2] cycloaddition transition state, and the relative energies for different constrained structures resembling the transition state, the method of B3LYP/LANL2DZ-6-31G(d) was applied in both geometry optimizations and energy calculations. In Chapter 4, M06-2X, which performs better for main-group chemistry, was employed to this metal-free system.

Table 1-1 DFT methods and solvation models used in different projects of this thesis

Project		Geomtery Optimization			Energy Calculation		
		Functional	Basis Set	Solvation Model	Functional	Basis Set	Solvation Model
Chapter 2	Cu-ATRP	w-B97XD	SDD for Cu; 6-31G(d) for other atoms	Gas phase	w-B97XD	def2-TZVP	CPCM (MeCN)
Chapter 3	<i>photoATRP</i>	B3LYP	6-31G(d)	SMD (DMF)	M06-2X	6-311++G(3df,2p)	SMD (DMF)
Chapter 4	Ru-ED-ROMP	B3LYP	LANL2DZ for Ru; 6-31G(d) for other atoms	Gas phase	B3LYP	LANL2DZ for Ru; 6-31G(d) for other atoms	Gas phase
Chapter 5	NHC-borane hydroboration	M06-2X	6-31G(d)	SMD (THF)	M06-2X	6-311++G(d,p)	SMD (THF)

1.2.2 Implicit solvation models

Although unable to describe the explicit short-range solvent-solute interactions, such as hydrogen-bonding, the implicit (continuum) solvation models¹⁹ are capable of describing the long-range solvent-solute interactions, and thereby computing the solvation effect on molecular structures, energies, and properties accurately and efficiently in most cases.

In implicit solvation models, the bulk of the solvent is represented as a continuum polarizable medium characterized by its dielectric constant (ϵ). The solute is placed in a molecule-shaped cavity in the continuum solvent. Thus, the solvation free energy could be calculated by eq 1-1.

$$\Delta G_{\text{solvation}} = \Delta G_{\text{cavity}} + \Delta G_{\text{dispersion-repulsion}} + \Delta G_{\text{electrostatic}} \text{ (eq. 1-1)}$$

where ΔG_{cavity} is the energy required to create the cavity, $\Delta G_{\text{dispersion-repulsion}}$ are the non-electrostatic interactions between the solvent and the solute molecules, including the dispersion interactions and repulsions, $\Delta G_{\text{electrostatic}}$ is the electrostatic interaction between the solvent and the solute molecules.

Several popular implicit solvation models include: Conductor-like Polarizable Continuum Model (CPCM²⁰), Solvation Model based on Density (SMD²¹), COnductor-like Screening MOdel (COSMO²²), and COSMO for Real Solvents (COSMO-RS²³). Among these, CPCM and SMD are two mostly used implicit solvation models in organic and organometallic reaction calculations. According to the benchmark studies, SMD provides on average better results than CPCM.²⁴ However, the performance of solvation models is highly system-dependent, which might require careful case-by-case benchmark investigation. Table 1-1 shows the implicit solvation models used in different projects covered in this thesis. For metal-free reactions discussed in Chapter 3 and

Chapter 5, both geometry optimization and energy calculations were performed in SMD solvation models. In Chapter 2 Cu-ATRP project, the geometry optimization was performed in gas phase since we validated that the transition state geometries optimized in gas phase and in solvation were similar, and the gas phase optimization was much more efficient. The CPCM solvation model was used in energy calculation instead of SMD model due to our benchmark results showing that the computed activation free energies with the CPCM model had better correlation with the experimental activation barriers than those with SMD model. In addition, since the goal in Chapter 4 was to obtain the geometry of Ru-catalyzed [2+2] cycloaddition transition state, both of the geometry optimization and energy calculations were performed in gas phase.

1.2.3 Marcus theory calculations

Marcus theory²⁵, which was originally developed by R. A. Marcus in 1956, was used to estimate the rates of single electron transfer (SET) reactions where an electron moves from the electron donor to the electron acceptor. Due to the fact that the electron transfer occurs very fast and usually doesn't follow clear reaction coordinate, Marcus theory takes place of the transition state theory for the estimation of SET activation barriers. In this thesis, three types of SET processes will be discussed: Outer-sphere SET (OSET) without bond forming and breaking, Dissociative SET (DET) where the electron transfer occurs simultaneously with bond dissociation, and Associative SET (AET) where the electron transfer occurs simultaneously with bond association. Detailed discussion of Marcus theory calculations is present in Chapter 2 and 3.

1.2.4 Molecular dynamics (MD) simulation

Molecular dynamics (MD) simulation²⁶ is widely used to study the physical movements of all atoms in a system over time, in which the positions and velocities of all atoms in the system evolve according to the Newton's equations of motion. Classical MD simulations, which apply force-field based molecular mechanics to compute the forces acting on atoms, have shown proved success in investigating the time evolution of conformations of proteins or other macromolecules.²⁷ Nowadays, the classical MD simulation is compatible with up to 100,000 atoms at time scale of about 1 μ s.

However, the classical MD simulation is unable to model chemical reactions due to the lack of accurate force fields that can describe bond forming/breaking in chemical reactions. Instead, Born-Oppenheimer MD (BOMD) simulation,^{28,29} as one type of *ab initio* MD simulations, can be used to investigate the time-resolved mechanisms of chemical reactions by propagating the reaction trajectories on an accurate potential energy surface (PES). In BOMD simulation, the optimized geometries, energies and forces at each point in the trajectories are computed with quantum mechanical methods such as DFT. As demonstrated in references, BOMD simulations have been typically used for two purposes: to study the bifurcation reaction where multiple products are formed via a single transition state,²⁸ and to study the dynamically-concerted/stepwise mechanism^{29b} by computing the time gap between multiple bonds formation.

In Chapter 4, I applied classical MD simulation to generate the conformations of macrocyclic olefins and investigate the steric environments around the double-bonds for each conformer. In Chapter 5, I applied BOMD simulations to study the bifurcation pathways for the alkyne hydroboration with NHC-boranes, and the dynamically concerted/stepwise mechanisms for aryne hydroboration with NHC-boranes.

1.2.5 Energy decomposition analysis (EDA)

Energy decomposition analysis (EDA)³⁰ is a powerful method to partition the quantum mechanics-calculated instantaneous interaction energy into its chemical origins such as electrostatics, exchange–repulsion, polarization, and charge transfer between the two fragments in a molecule or in a transition state.

On the basis of the original EDA methods (i.e. Kitaura-Morokuma scheme^{31,32} and Ziegler-Rauk scheme³³), a lot of modern variations of EDA methods have been developed, which primarily includes Natural EDA (NEDA),³⁴ Absolutely Localized Molecular Orbital EDA (ALMO-EDA),^{35,36} and Localized Molecular Orbital EDA (LMO-EDA).³⁷ Recently, EDA is becoming a promising approach to investigate the origin of reactivity and selectivity on organic and organometallic reactions.³⁸ In Chapter 2, ALMO-EDA was applied to analyze the origin of bent geometry for Cu-ATRP transition state.

1.2.6 Multivariate linear regression

Multivariate linear regression³⁹ is a classical statistical model to estimate the responses ($Y_{\text{predicted}}$) from multiple variables (X_i) using a linear association (eq. 1-2):

$$Y_{\text{predicted}} = \sum_i^N a_i \times X_i + a_0 \quad (\text{eq. 1-2})$$

where $Y_{\text{predicted}}$ is the predicted response values derived from the eq. 1-2, a_i is the coefficient for the i th variable X_i , X_i is the i th variable, and a_0 is the intercept of the linear regression.

Then, the coefficients a_i and the intercept a_0 can be solved by ordinary least squares (OLS) approach, in which the difference between the estimated response values ($Y_{\text{predicted}}$) and the experimentally observed response values (Y_{true}) will be minimized (eq. 1-3)

$$\min \|Y_{true} - Y_{predicted}\| = \min \sum_i^N (Y_i - \sum_i^N a_i \times X_i - a_0)^2 \quad (\text{eq. 1-3})$$

Sigman's group⁴⁰ and Doyle's group⁴¹ have successfully applied the multivariate linear regression approach to predict the experimental reactivity and selectivity using electronic and steric parameters of catalysts or substrates. Inspired by their elegant work, in Chapter 2, I developed a parameterization approach to predict the catalyst and initiator effect on the Cu-ATRP reactivities with the mechanistic insights from DFT calculations of the Cu-ATRP transition states.

1.3 Summary

Specifically, Chapter 2 discusses the computational studies on the mechanism, the effect of initiator and ligands in Cu-ATRP. I presented the first DFT study on the geometries and energies of the transition states in the activation/deactivation of Cu-ATRP. Detailed investigations of the transition states revealed key factors that control catalyst and initiator reactivities, which were utilized to build multivariate linear predictive models for the catalysts and initiators effects.

Chapter 3 focuses on the mechanistic studies on *photo*ATRP. I utilized DFT and Marcus theory calculations to predict the barriers of all competing pathways, including outer-sphere electron transfer (OSET) and inner-sphere electron transfer (ISET), in both activation and deactivation process in *photo*ATRP. The most favorable mechanisms were thus identified for the activation & deactivation in *photo*ATRP.

Chapter 4 talks about the computational investigation of the origin of selectivity-enhancement of *cis*-macrocyclic olefins over *trans*-monomers in ED-ROMP. I applied MD-DFT calculations to estimate the reactivity for each conformer of both *cis*- and *trans*- macrocyclic

olefins in ROMP, and investigate how the flexibility and conformation of the monomers affect the reactivity.

In Chapter 5, I applied DFT calculations and quasi-classical BOMD simulations to investigate the mechanisms, dynamics effect, and the origin of chemoselectivities in the hydroboration of alkynes and arynes with NHC-borane. The origin of the reactivity difference between alkynes, and arynes was also discussed in this chapter.

Chapter 2 is a revised version of a manuscript submitted to *Journal of the American Chemical Society*. The co-authors of the manuscript are C. Fang, M. Fantin, X. Pan, K. de Fiebre, M. L. Coote, K. Matyjaszewski, and P. Liu. (2019). This work is in collaboration with Prof. Krzysztof Matyjaszewski from Carnegie Mellon University, and Prof. Michelle Coote from Australian National University.

Chapter 3 is a revised version of X. Pan, C. Fang, M. Fantin, N. Malhotra, W. Y. So, L. A. Peteanu, A. A. Isse, A. Gennaro, P. Liu, and K. Matyjaszewski. *J. Am. Chem. Soc.* **2016**, 138, 7, 2411-2425. This work is in collaboration with Prof. Krzysztof Matyjaszewski, and Prof. Armando Gennaro from University of Padova.

Chapter 4 is a revised version of two published manuscripts in collaboration with Prof. Tara Meyer from University of Pittsburgh. J. A. Nowalk, C. Fang, A. L. Short, R. M. Weiss, J. H. Swisher, P. Liu, and T. Y. Meyer. *J. Am. Chem. Soc.* **2019** (Accepted); A. L. Short, C. Fang, J. A. Nowalk, R. M. Weiss, P. Liu, and T. Y. Meyer. *ACS Macro Lett.* **2018**, 7, 7, 858-862

Chapter 5 is a revised version of two manuscripts in collaboration with Prof. Dennis Curran at University of Pittsburgh. The first part about alkyne hydroboration is revised from T. R. McFadden, C. Fang, S. J. Geib, E. Merling, P. Liu, and D. P. Curran. *J. Am. Chem. Soc.* **2017**, 139, 5, 1726-1729. The second part about aryne hydroboration is unpublished.

2.0 MECHANISTICALLY GUIDED PREDICTIVE MODELS FOR LIGAND AND INITIATOR EFFECTS IN COPPER-CATALYZED ATOM TRANSFER RADICAL POLYMERIZATION (Cu-ATRP)

2.1 Introduction

Atom transfer radical polymerization (ATRP) is among the most powerful and robust controlled radical polymerization techniques that facilitate macromolecular engineering by synthesis of polymers with precise molecular weights, low dispersities, and well-controlled architectures.⁴² Although ATRP has been achieved with diverse transition metal⁴³ and photoredox catalysts,^{44, 45} copper-catalyzed ATRP (Cu-ATRP) is still the most extensively used and investigated ATRP^{42a, 46} with a wide range of compatible monomers, initiators, and solvents. Control of polymer chain growth via Cu-ATRP is largely attributed to the dynamic activation/deactivation equilibrium between a $[\text{Cu}^{\text{I}}\text{L}]^+ / [\text{Br-Cu}^{\text{II}}\text{L}]^+$ couple where L represents a multidentate nitrogen-donor ligand (Figure 2-1).^{47, 48} The $[\text{Cu}^{\text{I}}\text{L}]^+$ catalyst activates the dormant alkyl bromide chain end ($\text{P}_n\text{-Br}$) to reform the $[\text{Br-Cu}^{\text{II}}\text{L}]^+$ complex and a propagating alkyl radical ($\text{P}_n\bullet$). The alkyl radical continues to grow by adding a few monomers before it abstracts the Br from $[\text{Br-Cu}^{\text{II}}\text{L}]^+$ to form alkyl bromide. A successful ATRP catalyst system should have a large activation rate constant (k_{act}) and an even larger deactivation rate constant (k_{deact}) to provide good control over the polymerization while maintaining a reasonable polymerization rate.

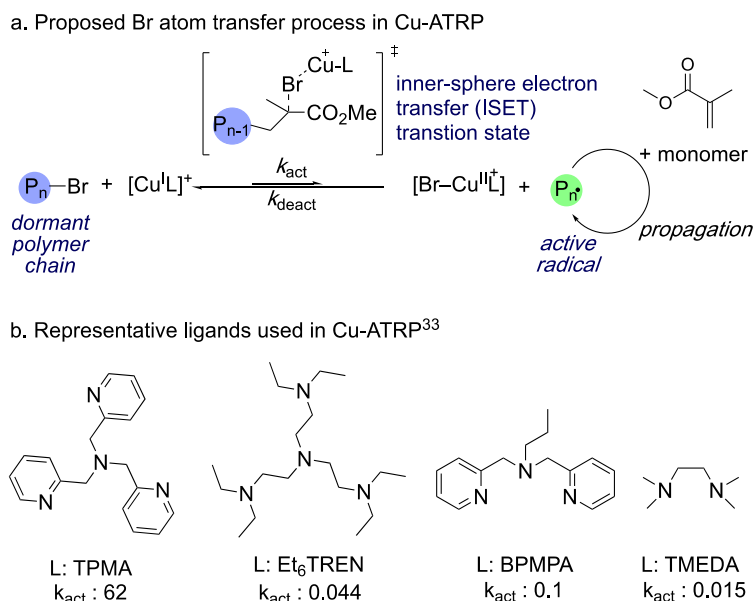


Figure 2-1 Ligand effects on the activation/deactivation of Cu-ATRP

Previous mechanistic studies from Coote, Gennaro, and Matyjaszewski indicated that Cu-ATRP occurs via a concerted inner-sphere electron transfer (ISET) process in which the Br atom is transferred from the alkyl bromide to the $[Cu^I L]^+$ catalyst (Figure 2-1a), because the predicted outer-sphere electron transfer (OSET) barriers are much higher than experimental data.⁴⁹ However, the geometry and energy of this Br atom transfer transition state have not been explored by computations so far. Although a few computational studies demonstrated that the reactivity of alkyl halide initiators is affected by their bond dissociation energies^{49,50} and LUMO energies,⁵¹ it remains challenging to understand and computationally predict the reactivities of Cu-ATRP catalysts with the structurally-diverse ligands (Figure 2-1b). The lack of theoretical insights into the origins of ligand effects hinders the rational catalyst design for Cu-ATRP. Herein, we describe a workflow to establish mechanistically guided predictive models for the reactivity of Cu-ATRP catalysts. Inspired by the elegant work from Sigman⁴⁰ and Doyle⁴¹'s groups that utilizes a multivariate regression approach to predict ligand effects in transition metal catalyzed reactions

using steric and electronic parameters, we surmised such parameterization approach may be facilitated by mechanistic insights from DFT calculations. In particular, in-depth analysis of factors that stabilize the rate-determining transition state may offer the theoretical basis for the rational selection of ligand parameters.⁵² Our workflow to establish the predictive mathematical equation is summarized in Figure 2-2. First, we applied DFT calculations to obtain the geometries and energies of Cu-ATRP activation transition states. Detailed investigations of the transition states revealed key factors that control catalyst and initiator reactivities. These theoretical insights were then utilized to rationally select a set of chemically meaningful descriptors to define effects of different factors on the reactivity. Finally, a simple mathematical equation for predicting ligand effect was established by correlating these descriptors with experimental reactivities using a multivariate regression approach. Similarly, a predictive equation was developed for the reactivity of different alkyl halide initiators. These predictive models can be used to guide rational catalyst design⁵³ and computational ligand discovery for Cu-ATRP reactions.

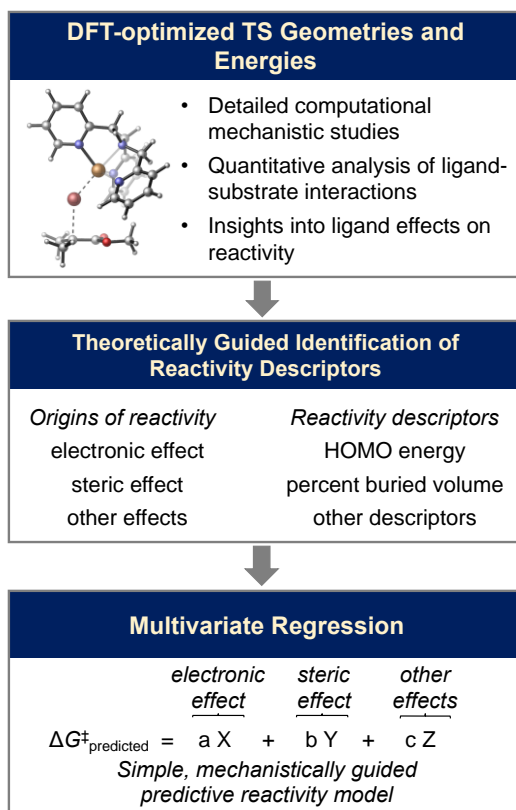


Figure 2-2 Workflow of establishing predictive models for reactivity of Cu-ATRP catalysts

2.2 Computational methods

2.2.1 DFT calculations

All geometry optimizations and single point energy calculations were performed with the Gaussian 09 software package.⁵⁴ Geometries were optimized in the gas phase using the ω -B97XD¹² functional and a mixed basis set of SDD¹⁵ for Cu and 6-31G(d)¹³ for other atoms. Single point energies were calculated using ω -B97XD and the def2-TZVP¹⁸ basis set in acetonitrile using the CPCM solvation model.²⁰ Reported Gibbs free energies and enthalpies in solution include thermal corrections computed at 298 K and are computed at the standard concentration (1 mol/L).

The activation free energies of the outer-sphere single electron transfer reactions were calculated using modified Marcus theory.^{25, 55} Distortion/interaction model and energy decomposition analysis (EDA) calculations were performed to dissect the computed gas-phase activation energy (ΔE^\ddagger). The activation energy was first decomposed into the distortion energy of the two reactive fragments, *i.e.* the $[\text{Cu}^{\text{I}}\text{L}]^+$ catalyst and the alkyl halide, to reach their transition state geometries ($\Delta E_{\text{dist}} = \Delta E_{\text{dist}(\text{CuL})} + \Delta E_{\text{dist}(\text{RX})}$) and the interaction energy (ΔE_{int}) between these two fragments (eq. 2-1).^{56,57}

$$\Delta E^\ddagger = \Delta E_{\text{dist}} + \Delta E_{\text{int}} \quad (\text{eq. 2-1})$$

Here, the distortion energies were calculated from the energy difference between the distorted fragment in the transition state geometry and the same fragment in the fully optimized ground state geometry. Then, ΔE_{int} is calculated from $\Delta E_{\text{int}} = \Delta E^\ddagger - \Delta E_{\text{dist}}$. Next, ΔE_{int} was further dissected into chemically meaningful terms using the second-generation EDA based on absolutely-localized molecular orbitals (ALMO-EDA2)^{35,36} in Q-Chem 5.0 (eq. 2-2).⁵⁸

$$\Delta E_{\text{int}} = \Delta E_{\text{pauli}} + \Delta E_{\text{elstat}} + \Delta E_{\text{disp}} + \Delta E_{\text{orb}} \quad (\text{eq. 2-2})$$

Here, ΔE_{pauli} is the Pauli repulsion, ΔE_{elstat} is the electrostatic interactions, ΔE_{disp} is the dispersion interaction, and ΔE_{orb} is the orbital interaction energy that consists of interfragment charge transfer energy and intrafragment polarization energy.

2.2.2 Marcus Theory Calculations

We used the modified Marcus theory to estimate the barriers for the stepwise outer-sphere single electron transfer (OSET-SW) and the concerted dissociative electron transfer (DET)

processes in the reduction of MMA-Br by $[\text{Cu}^{\text{I}}\text{-TPMA}]^+$. The DFT calculations were performed at the $\omega\text{-B97XD/def2-TZVP//}\omega\text{-B97XD/SDD-6-31G(d)}$ level of theory in acetonitrile at 25°C.

OSET-SW pathway in the activation



The following equation was used to calculate the activation free energy of activation ($\Delta G_{\text{OSET-SW}}^{\ddagger}$) in the OSET-SW pathway:

$$\Delta G_{\text{OSET-SW}}^{\ddagger} = \Delta G_0^{\ddagger} \left(1 + \frac{\Delta_r G^{\ominus}}{4\Delta G_0^{\ddagger}} \right)^2$$

Here, $\Delta_r G^{\ominus} = 36.1$ kcal/mol is the reaction energy of eq. 2-3 obtained from DFT calculations. The intrinsic barrier is determined using $\Delta G_0^{\ddagger} = \lambda_0/4$, where λ_0 is the solvent reorganization energy that can be calculated as follows:

$$\lambda_0 = A \times [(2r_{\text{D}})^{-1} + (2r_{\text{A}})^{-1} - (r_{\text{D}} + r_{\text{A}})^{-1}]$$

where r_{D} and r_{A} are the hard sphere radii of electron donor and acceptor, respectively. A is an empirical constant. Here we used $A = 99 \text{ kcal mol}^{-1} \text{ \AA}$ as suggested in the Coote and Matyjaszewski's study.⁴⁹ Thus,

$$\begin{aligned} \lambda_0 &= 99 \times [(2r_{[\text{CuI-TPMA}]^+})^{-1} + (2r_{\text{MMA-Br}})^{-1} - (r_{[\text{CuI-TPMA}]^+} + r_{\text{MMA-Br}})^{-1}] \\ &= 99 \times [1/(4.29 \times 2) + 1/(3.58 \times 2) - 1/(4.29 + 3.58)] \\ &= 12.8 \text{ kcal/mol} \end{aligned}$$

leading to

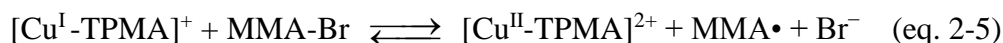
$$\Delta G_0^{\ddagger} = \lambda_0/4 = 3.2 \text{ kcal/mol}$$

Thus,

$$\Delta G_{OSET-SW}^{\ddagger} = 3.2 \times \left(1 + \frac{36.1}{4 \times 3.2}\right)^2 = 46.7 \text{ kcal/mol}$$

The dissociation of the radical anion [MMA-Br] \cdot^- is highly exothermic (Figure 2-3) and is expected to be very fast. Therefore, the rate-determining step in the OSET-SW pathway is the outer-sphere single electron transfer (eq. 2-3).

DET pathway in the activation



In the DET pathway (eq. 2-5), the electron transfer occurs with simultaneous alkyl halide bond dissociation to form the MMA \cdot radical and the Br $^-$ anion in a polar solvent (MeCN) cage. Thus, the “sticky” model⁴⁹ is used to estimate the free energy of activation of the DET pathway:

$$\Delta G_{DET}^{\ddagger} = \Delta G_0^{\ddagger} \left(1 + \frac{\Delta_r G^{\ominus} - D_p}{4\Delta G_0^{\ddagger}}\right)^2$$

$$\Delta G_0^{\ddagger} = \frac{(\sqrt{D_{\text{MMA-Br}}} - \sqrt{D_p})^2 + \lambda_0}{4}$$

where ΔG_0^{\ddagger} is the the intrinsic barrier; $\Delta_r G^{\ominus} = 26.0$ kcal/mol is the DFT-calculated reaction energy for eq. 2-5; D_p is the interaction energy between MMA \cdot and Br $^-$ in the solvent cage, and the experimental data of $D_p = 0.24$ kcal/mol is used in our calculation;⁸⁵ $D_{\text{MMA-Br}}$ is the MMA–Br bond dissociation enthalpy calculated using DFT ($D_{\text{MMA-Br}} = 56.7$ kcal/mol); λ_0 is the solvent reorganization energy that is the same as that in the OSET-SW pathway ($\lambda_0 = 12.8$ kcal/mol).

Thus,

$$\Delta G_0^\ddagger = \frac{(\sqrt{D_{MMA-Br}} - \sqrt{D_p})^2 + \lambda_0}{4} = \frac{(\sqrt{56.7} - \sqrt{0.24})^2 + 12.8}{4} = 15.59 \text{ kcal/mol}$$

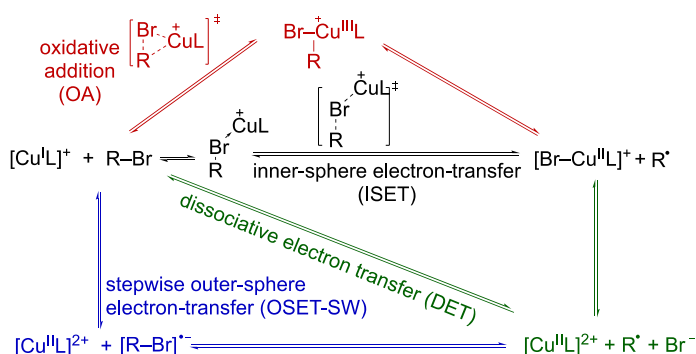
$$\Delta G_{DET}^\ddagger = \Delta G_0^\ddagger \left(1 + \frac{\Delta_r G^\ominus - D_p}{4\Delta G_0^\ddagger}\right)^2 = 15.59 \times \left(1 + \frac{26.0 - 0.24}{4 \times 15.59}\right)^2 = 31.1 \text{ kcal/mol}$$

2.3 Results and Discussion

2.3.1 Activation mechanisms in Cu-ATRP

In previous studies, several possible mechanisms have been proposed for the activation/deactivation process in Cu-ATRP (Figure 2-3a), including inter-sphere single electron transfer (ISET), stepwise outer-sphere single electron transfer (OSET-SW), and dissociative electron transfer (DET).⁴⁹

a. Possible mechanisms of Cu-ATRP activation



b. Computed energy profiles for Cu-ATRP activation of MMA-Br (**2**)

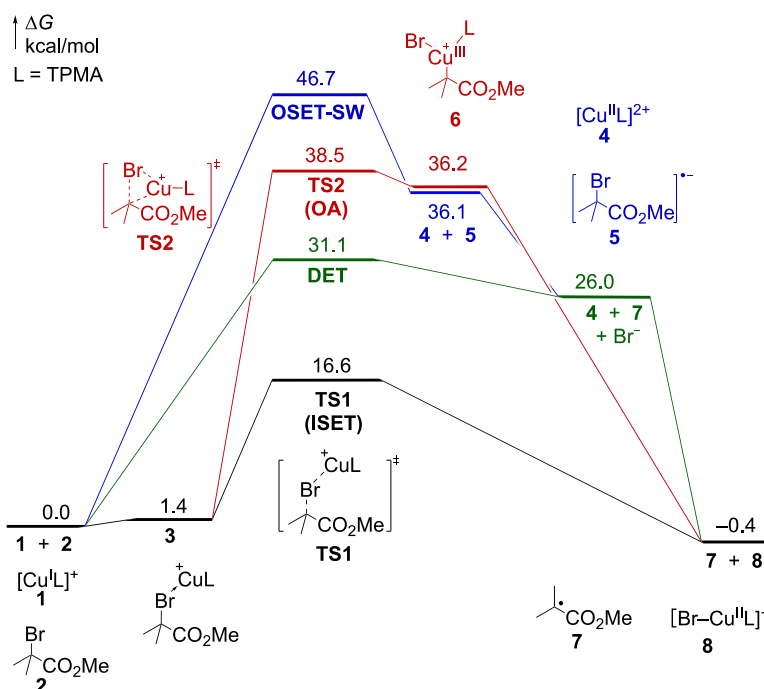


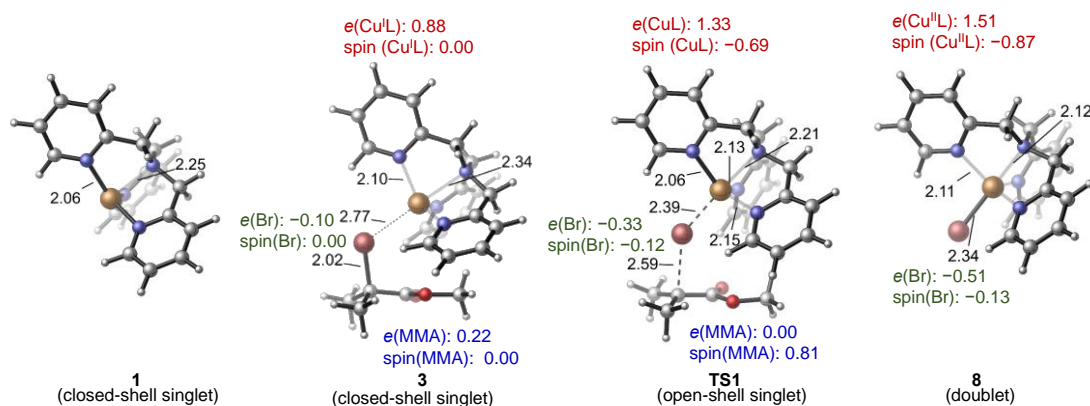
Figure 2-3 Computed energy profiles of Cu-ATRP activation pathways in MeCN at 25 °C with tris(2-pyridylmethyl)amine (TPMA) ligand

Here, we used DFT and Marcus theory to investigate these previously proposed pathways, as well as the oxidative addition (OA) of alkyl bromide to the Cu^I catalyst to form a Cu^{III} intermediate (Figure 2-3b). The barrier for the concerted DET to form the MMA radical **7** and a bromide was estimated using the “sticky model”, a modification of the Marcus theory.⁵⁵ The

calculations were performed using a model system that consists of $[\text{Cu}^{\text{I}}(\text{TPMA})]^+$ (TPMA: tris(2-pyridylmethyl)amine), one of the most popular ATRP catalysts, and a widely used initiator α -bromoisobutyrate (*i.e.* a mimic of a dormant chain end in ATRP of methyl methacrylate, MMA-Br, **2**). In agreement with previous computational studies,⁴⁹ the OSET-SW and DET processes both involve very high barriers that are inconsistent with experimental data. The oxidative addition of the sterically crowded tertiary alkyl bromide (**TS2**) also requires a very high barrier.⁵⁹ The most favorable activation mechanism is the concerted ISET (**TS1**), which requires a substantially lower barrier ($\Delta G^\ddagger = 16.6$ kcal/mol in MeCN) than other processes considered.

The optimized geometries, Mulliken atomic charges, and spin densities of the Cu^{I} and Cu^{II} complexes and transition state involved in the ISET pathway are shown in Figure 2-4. The analysis of charge and spin density along the reaction coordinate (Figure 2-4b) indicates a dramatic change of charge and spin density before **TS1**, while both quantities remain almost constant after the transition state. The computed Mulliken charge of the CuL fragment in **TS1** is +1.33, indicating a considerable amount (0.33 *e*) of charge transfer from the $[\text{Cu}^{\text{I}}\text{L}]^+$ catalyst to the alkyl bromide in the ISET transition state. Nonetheless, since the charge transfer in **TS1** is much less than unity and the Cu is less positively charged than that in the $[\text{Br-Cu}^{\text{II}}\text{L}]^+$ complex **8**, the Cu...Br interaction in **TS1** has a significant covalent character. The much-shortened Cu-Br bond distance (2.39 Å) and the elongated C-Br bond distance (2.59 Å) in **TS1**, along with the relatively large spin densities on the Cu and the MMA, indicate the ISET process involves a late transition state that structurally resembles the $[\text{Br-Cu}^{\text{II}}\text{L}]^+$ product. Furthermore, the computed Wiberg bond indices⁶⁰ of the Cu-Br bond in **TS1** and **8** are 0.386 and 0.574, respectively, which is consistent with a late transition state with a substantial bonding interaction between the Cu and Br in **TS1**.

a. Optimized geometries of $[\text{Cu}^{\text{I}}\text{L}]^+$ (**1**), dative complex (**3**), ISET transition state (**TS1**), and $[\text{Br}-\text{Cu}^{\text{II}}\text{L}]^+$ (**8**)



b. Energy, charge, and spin density along the reaction coordinate

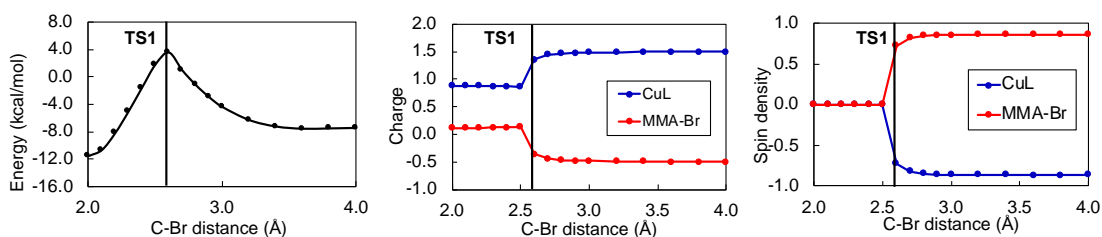


Figure 2-4 Optimized geometries, energies, Mulliken charges, and spin densities of computed structures in the ISET pathway

The optimized geometry of **TS1** has a substantially bent Cu–Br–C bond angle (141.9°). This is rather surprising considering most known halogen atom transfer processes involve a linear transition state structure.^{44,61,62} The bent geometry means a closer distance between the ancillary ligand and the substrate (*i.e.* the alkyl halide initiator or the dormant chain end). As such, the non-covalent interactions between the ligand and the substrate, a previously underappreciated effect, may play a significant role on the activation/deactivation reactivity. Because of its potential impacts on the catalyst reactivity, we have undertaken a detailed computational analysis to investigate the origin of the bent geometry.

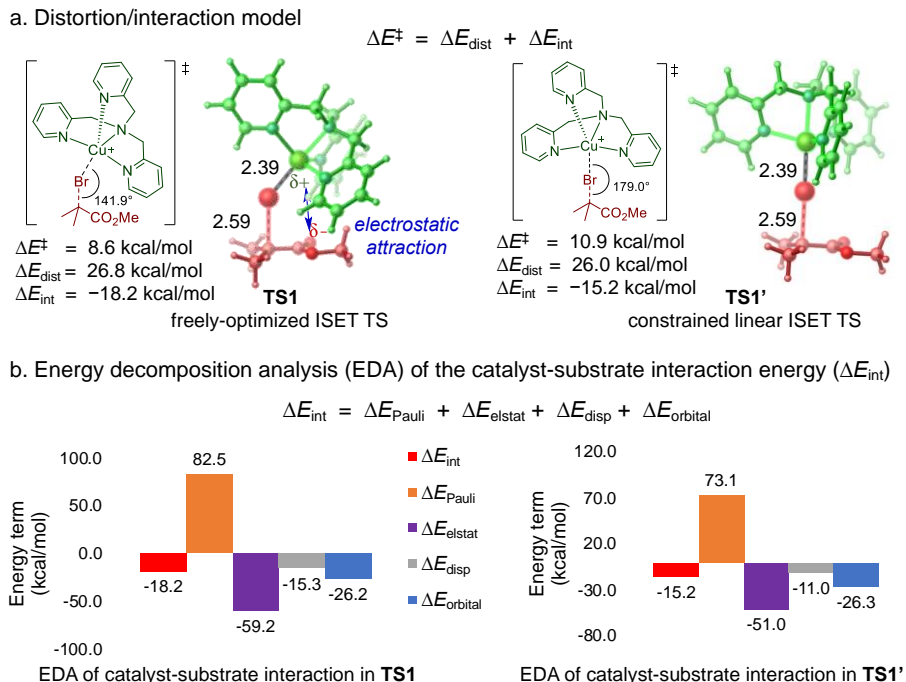


Figure 2-5 The origin of the bent geometry in TS1

We performed a constrained optimization of the ISET transition state by forcing a linear geometry, fixing the Cu–Br–C bond angle at 179° (Figure 2-5a). It was found that the freely optimized bent transition state was 2.3 kcal/mol lower in energy than the linear transition state. The distortion/interaction model analysis indicates the bent TS geometry has 3.0 kcal/mol more favorable interaction energy (ΔE_{int}) between the CuL catalyst and the MMA-Br. We then applied the energy decomposition analysis methods to dissect the interaction energy (Figure 2-5b). Although the bent transition state is disfavored by Pauli repulsion ($\Delta\Delta E_{\text{Pauli}} = +9.4 \text{ kcal/mol}$), it has stronger attractive electrostatic interaction ($\Delta\Delta E_{\text{elstat}} = -8.2 \text{ kcal/mol}$) and dispersion interaction ($\Delta\Delta E_{\text{disp}} = -4.3 \text{ kcal/mol}$) between the catalyst and the substrate than linear transition state. While the increased dispersion is expected to partially compensate the Pauli repulsion effect, the stronger electrostatic interaction is attributed to the attraction between the positively charged

Cu catalyst and the partial negatively charged ester group of the substrate. DFT calculations using other alkyl halides also provided bent ISET transition state structures (Figure 2-6). The bent TS structures are stabilized by either electrostatic attraction with the Cu catalyst when an electron-withdrawing group is present in the chain end or attractive London dispersion forces in reactions with benzylic halides.

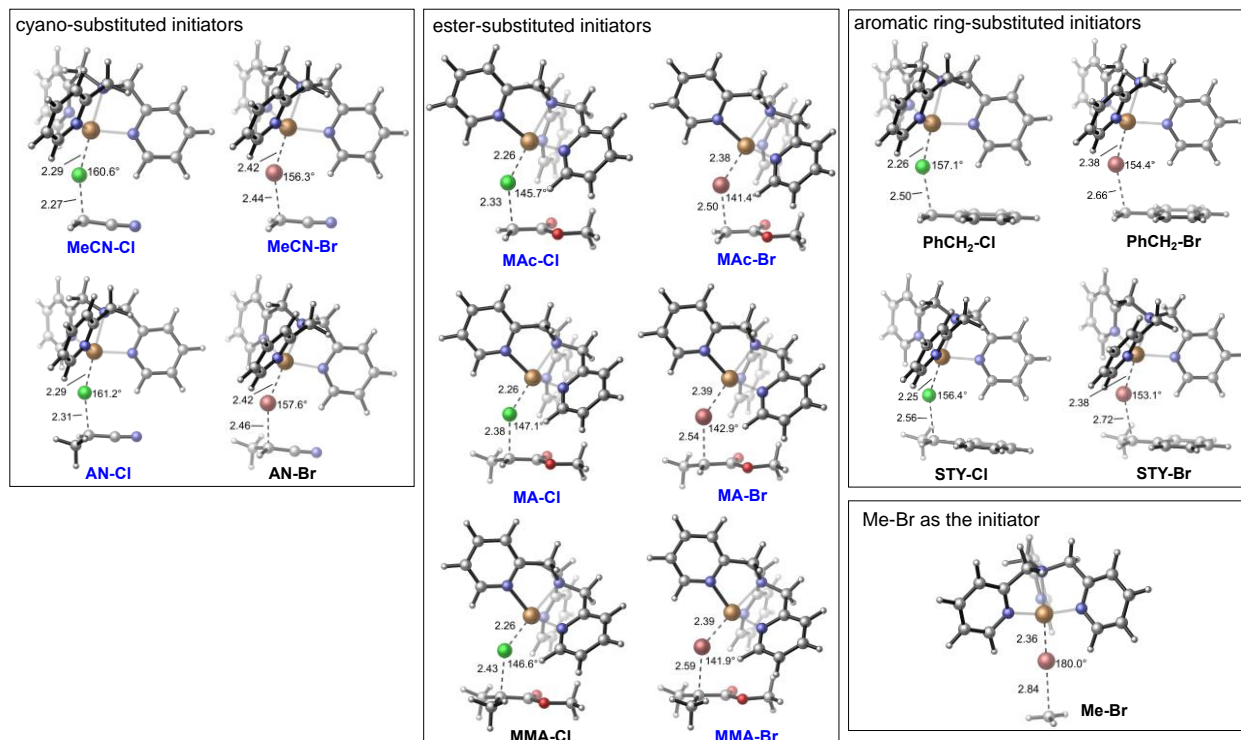


Figure 2-6 Optimized geometries of ISET TS of 15 initiators with $[\text{Cu}^{\text{I}}(\text{TPMA})]^+$ catalyst. The initiators highlighted in blue are reported in Section 2.3.2

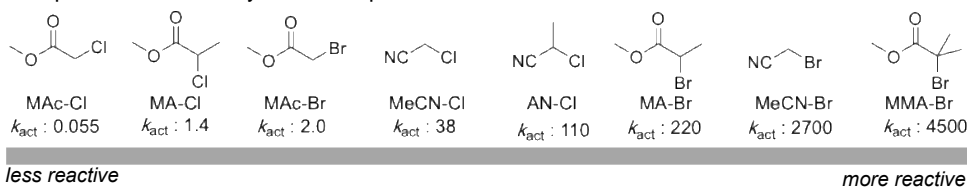
Collectively, the computational data indicate the ISET involves a late, open-shell singlet transition state that is consistent with a concerted bromine atom transfer^{44,61,62} process. The substantial C-Br bond stretch and Cu-Br interactions in the late TS implies that the BDE of the carbon-halogen bond and the halogen binding energy to Cu both play a significant role on the reaction rate.⁶³ In addition, the charge transfer from the Cu catalyst to the alkyl bromide in the

ISSET TS suggests a more electron-rich ligand would promote the reaction. The bent transition state geometry suggests the ligand-substrate non-bonding interactions are expected to affect the stability of the transition state. These mechanistic insights were used to develop the predictive models for reactivity between different alkyl halide initiators and the Cu ATRP catalysts (*vide infra*).

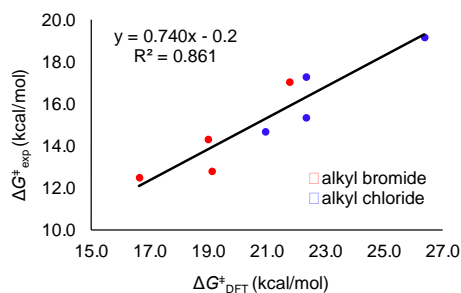
2.3.2 Predictive Model for Initiator Effects on Reactivity

Over the past decades, Cu-ATRP was successfully employed with a variety of initiators, which activation rate constants (k_{act}) have been determined by experimental kinetic studies with different catalysts (Figure 2-7a).^{64,65} Herein, we report the first computational prediction of activation barriers for a representative set of alkyl bromide and alkyl chloride initiators (R-X, Figure 2-7a) using transition state calculations. The DFT-computed barriers of the ISET transition states ($\Delta G_{\text{DFT}}^{\ddagger}$) with the $[\text{Cu}^{\text{I}}(\text{TPMA})]^+$ catalyst provided a good agreement with the experimentally determined reactivity trend ($\Delta G_{\text{exp}}^{\ddagger}$)⁶⁶ for both alkyl bromide and alkyl chloride initiators (Figure 2-7b), which validates the robustness and reliability of the computational methods and computed transition state models. To further explore the origin of reactivity of the different initiators, we performed distortion/interaction model analysis for the computed ISET transition states. The results indicate the activation energies correlates well with the distortion energies of the R-X initiators (Figure 2-8). Furthermore, ISET transition states with alkyl bromides are stabilized by stronger interaction energies between the Cu catalyst and the halide compared to those with alkyl chlorides (Figure 2-9). Therefore, the distortion/interaction model analysis reaffirmed the significant roles of both the R-X bond strength and Cu-X interactions on the stability of the transition state.

a. Experimental reactivity trend of representative initiators³⁴



b. Experimental barrier vs. Calculated barrier



c. Experimental barrier vs. Calculated R-X BDE

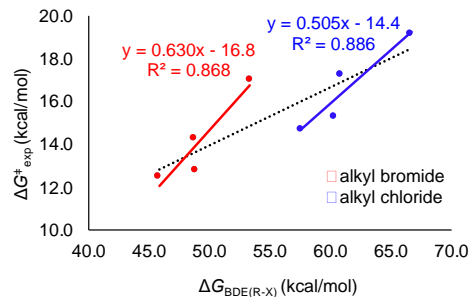
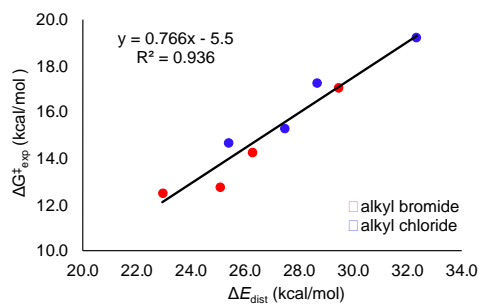


Figure 2-7 Initiator effect in Cu-ATRP with the Cu^I-TPMA catalyst

a. Correlation of total distortion energies (ΔE_{dist}) with experimental activation barriers



b. Correlation of initiator distortion energies ($\Delta E_{\text{dist(R-X)}}$) with experimental activation barriers

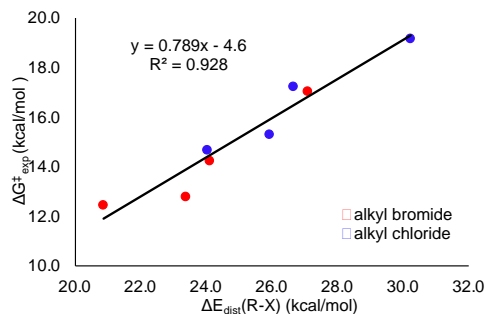


Figure 2-8 Correlation of distortion energies with experimental reactivities of alkyl halide initiators

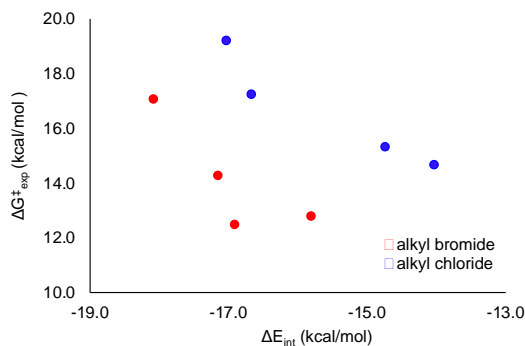


Figure 2-9 Correlation of interaction energies (ΔE_{int}) with experimental reactivities of alkyl halide initiators

Because the transition state analysis indicated the R–X bond strength and the Cu–X covalent interactions are both important factors for the transition state energy, we surmised the R–X BDE and the halogenophilicity⁴⁹ (*i.e.* the binding ability of X• to [Cu^IL]⁺) can be used as two appropriate descriptors for the initiator reactivity model. Although it has been widely recognized that the R–X BDE plays a significant role on the activation rate,^{49,50} the computed BDEs do not have a good overall correlation with experimental barriers for the entire set of alkyl bromide and chloride initiators (Figure 2-7c, dashed line). However, within the same type of halides (X = Br or Cl), R–X BDEs are good indicators of their reactivities (Figure 2-7c, solid red and blue lines). This indicates the halogenophilicity is another important factor impacting the reactivity. Indeed, when combining R–X BDE with Cu–X halogenophilicity ($E(\text{Cu}, \text{X}^\bullet)$), the two-parameter equation (eq. 2-6) provides an excellent correlation with the experimentally observed activation rate constants. (Figure 2-10). Previous studies have revealed a good correlation between the activation rate constant and the activation/deactivation equilibrium constant (K_{ATRP}).^{65, 67} Because K_{ATRP} is determined by both R–X BDE and Cu–X halogenophilicity, our two-parameter equation is consistent with the experimentally observed effects of K_{ATRP} on the activation rate.

$$\Delta G_{\text{predicted}}^\ddagger = 0.56 \times \text{BDE}(\text{R-X}) + 0.39 \times E(\text{Cu}, \text{X}^\bullet) + 4.8 \quad (\text{eq.2-6})$$

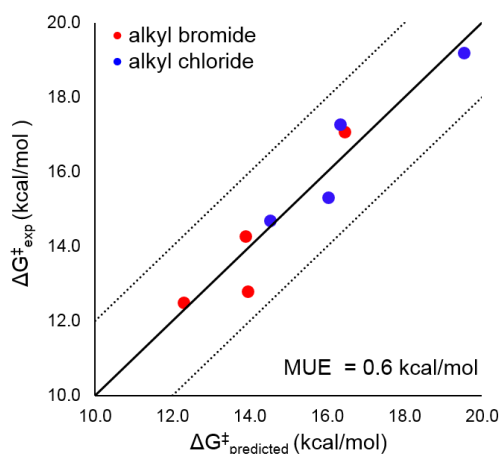


Figure 2-10 Predictive model for initiator reactivity in Cu-ATRP

2.3.3 Predictive Model for Ligand Effects on Reactivity

The reactivities of Cu-ATRP catalysts can be significantly impacted by altering the structures of their *N*-donor ligands.⁶⁸ In the past decades, a structurally diverse set of multidentate *N*-donor ligands have been used experimentally, including bi-, tri-, and tetradentate ligands with either sp^2 or sp^3 *N* atoms (Figure 2-11). The reactivity of the Cu-ATRP catalyst appears to be affected by a combination of a few different types of effects, including electronic, steric, denticity, hybridization, and other factors. As such, rational ligand design for efficient Cu-ATRP catalysts remains challenging. Here, we use the three-step approach described in the Introduction (Figure 2-2) to establish a simple mathematical equation for the prediction of the activation rate of Cu-ATRP catalysts. We selected 9 representative ligands with distinct electronic and steric properties (blue squares in Figure 2-11) as a training set to understand the factors controlling the ATRP activation rate constants, and to identify suitable descriptors for the predictive model. The rest of the ligands (red squares, circles, and triangles) are used as test sets to validate the reliability of the predictive model. All of ISET transition states were calculated with the same initiator MMA-Br.

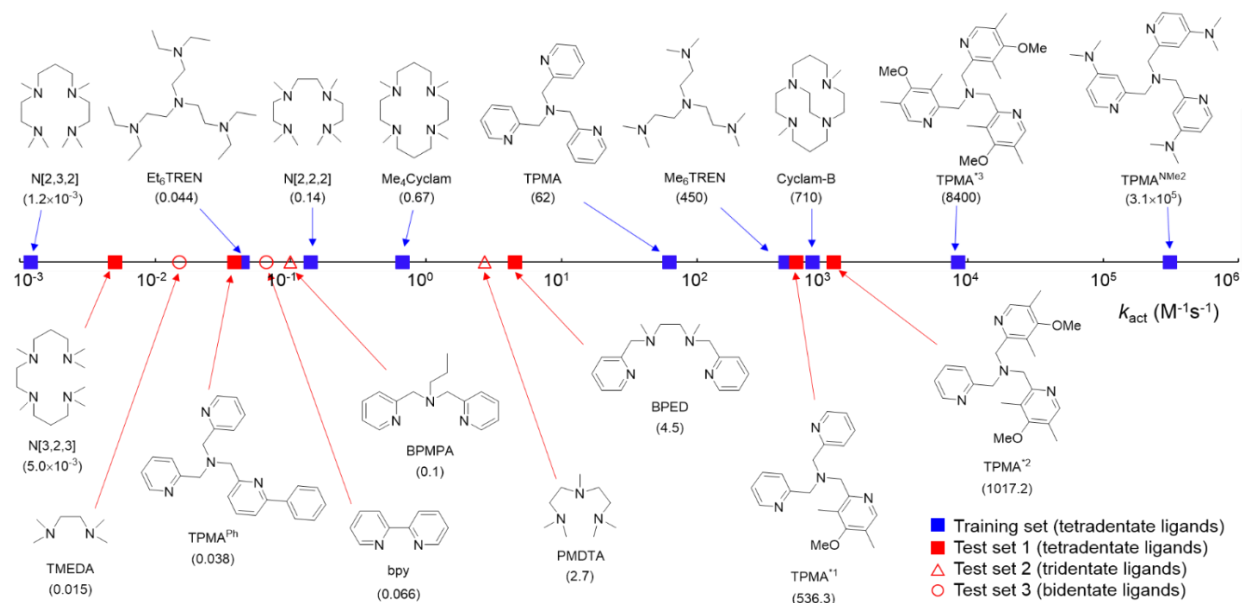


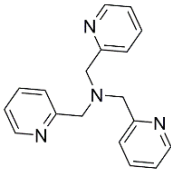
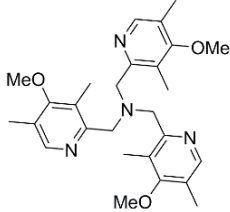
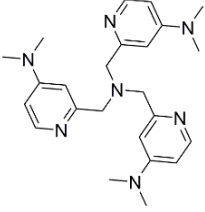
Figure 2-11 Representative ligands for Cu-ATRP catalyst. Experimentally k_{act} are provided in parentheses⁶⁸

2.3.3.1 Ligand electronic effect

Three TPMA derivatives (**L1-L3**) with similar steric properties were chosen to investigate the electronic effects of the ancillary ligands. Recently, Matyjaszewski group discovered that incorporation of electron-donating groups in the pyridine ring of TPMA profoundly increased the ATRP catalyst activity (Table 2-1).⁶⁹ Notably, the dimethyl amino ($-NMe_2$) substituted TPMA (**L3**, TPMA^{NMe2}) ligand forms the most reactive Cu-ATRP catalyst reported to date. We performed DFT calculations to locate the ISET transition states for these three Cu-ATRP catalysts in Figure 2-12. The DFT-predicted activation barriers (ΔG_{DFT}^\ddagger) were consistent with the experimental reactivity trend. The computed percent buried volume ($V_{bur}\%$)⁷⁰ and the catalyst distortion energy in the transition state ($\Delta E_{dist}(TS)$) are similar for all three catalysts, which confirmed the ligand steric properties and the distortion of the Cu catalysts are comparable among this group of ligands. As such, their reactivity difference is expected to be mainly controlled by inductive electronic effects of the ligand. A good correlation between the activation energies and the computed HOMO energy

of the Cu^I catalyst (E_{HOMO}) was observed (Figure 2-13). Thus, E_{HOMO} was chosen as an appropriate descriptor to describe the electronic effects of the ancillary ligand.

Table 2-1 Electronic effects of the TPMA family ligands.^a

<div style="display: flex; justify-content: space-around; align-items: flex-end;"> <div style="text-align: center;">  <p>L1: TPMA $k_{\text{act}} = 62$</p> </div> <div style="text-align: center;">  <p>L2: TPMA*³ $k_{\text{act}} = 8400$</p> </div> <div style="text-align: center;">  <p>L3: TPMA^{NMe2} $k_{\text{act}} = 3.1 \times 10^5$</p> </div> </div>						
ligand	$\Delta G^{\ddagger}_{\text{exp}}$	$\Delta G^{\ddagger}_{\text{DFT}}$	E_{HOMO}^b	$V_{\text{bur}}\%$ ^c	$\Delta E_{\text{dist}}(\text{TS})^d$	$\Delta E_{\text{dist}}(\text{BrCu}^{\text{II}}\text{L})^e$
TPMA	15.0	16.6	−7.66	39.2	2.1	4.0
TPMA* ³	12.0	14.6	−7.41	40.3	2.0	3.6
TPMA ^{NMe2}	10.0	13.0	−7.36	39.0	1.8	3.7

^a All Gibbs free energies and distortion energies are in kcal/mol; E_{HOMO} is in eV. ^b HOMO energy of the $[\text{Cu}^{\text{I}}\text{L}]^+$ computed at the ω -B97XD/def2-TZVP level of theory in acetonitrile using the CPCM solvation model. ^c Percent buried volume of the ligand computed from the DFT-optimized geometry of the $[\text{Cu}^{\text{I}}\text{L}]^+$.⁷⁰ ^d Distortion energy of the CuL catalyst in the ISET transition state with respect to the ground state $[\text{Cu}^{\text{I}}\text{L}]^+$. ^e Distortion energy of the CuL catalyst in the $[\text{BrCu}^{\text{II}}\text{L}]^+$ complex with respect to the ground state $[\text{Cu}^{\text{I}}\text{L}]^+$.

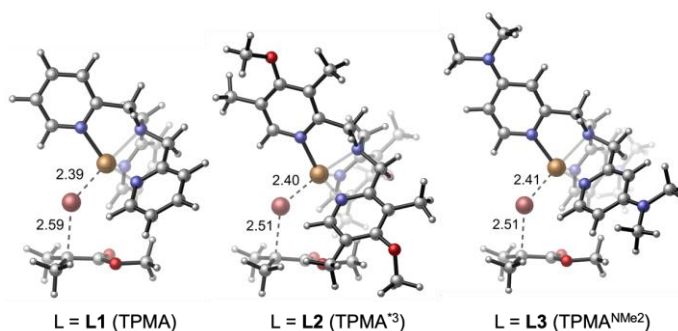


Figure 2-12 Optimized geometries of ISET transition states with TPMA family ligands

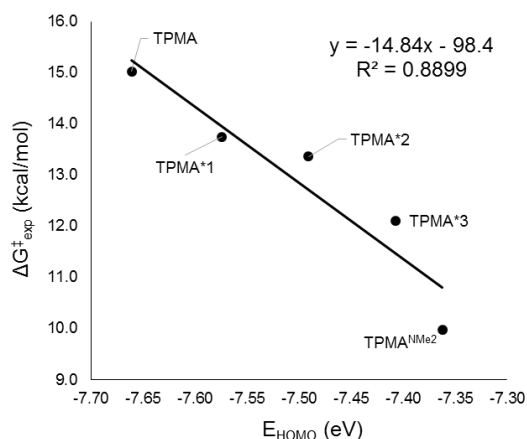


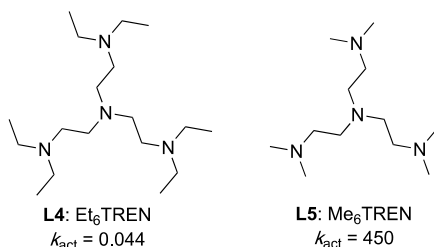
Figure 2-13 Correlation of experimental reactivities and the HOMO energies of five $[\text{Cu}^{\text{I}}\text{L}]^+$ catalysts with TPMA family ligands

2.3.3.2 Ligand Steric Effect

Me_6TREN (**L5**) is another highly effective and commonly employed ligand in Cu-ATRP.⁶⁸ When replacing all *N*-methyl substituents with ethyl groups (**L4**, Et_6TREN), the ATRP reactivity dramatically decreases (Table 2-2). Considering their similar electronic properties, this series of ligands was chosen to study the ligand steric effect on reactivity. The optimized ISET transition states with both ligands have a greater Cu–Br–C bond angle than that of **TS1**, indicating greater steric repulsions than with the TPMA ligand (Figure 2-14). The computationally predicted barrier with Et_6TREN is more than 4 kcal/mol higher than that with Me_6TREN (Table 2-2), in agreement with the experimental reactivity trend. The decreased reactivity with the Et_6TREN ligand is mostly due to the greater steric hindrance of the ligand as evidenced by the less bent geometry in the ISET transition state (Figure 2-14). As shown in Table 2-2, the widely used percent buried volume ($V_{\text{bur}}\%$)⁷⁰ is an appropriate descriptor to distinguish the ligand steric properties. Et_6TREN has a much larger $V_{\text{bur}}\%$ than Me_6TREN (56.5% versus 45.7%), while the less hindered TPMA has a smaller $V_{\text{bur}}\%$ (39.2%) than both ligands. As expected, the computed HOMO energies for **L4** and

L5 are similar, which confirmed the similar electronic properties of these ligands. Although the transition state with Et₆TREN has greater distortion energy ($\Delta E_{\text{dist(TS)}}$) than that with Me₆TREN, the relatively small distortion energy difference between the two transition states suggests the ligand distortion may not strongly correlate with the steric effects of ligands. Effects of ligand distortion on reactivity are discussed in more detail below.

Table 2-2 Steric effects of the TREN family ligands^a



ligand	$\Delta G_{\text{exp}}^{\ddagger}$	$\Delta G_{\text{DFT}}^{\ddagger}$	E_{HOMO}^b	$V_{\text{bur}}\%^c$	$\Delta E_{\text{dist(TS)}}^d$	$\Delta E_{\text{dist(BrCu}^{\text{II}}\text{L)}}^e$
Et ₆ TREN	19.3	18.5	-7.33	56.5	3.5	5.1
Me ₆ TREN	13.8	14.3	-7.34	45.7	2.2	4.0

^a All Gibbs free energies and distortion energies are in kcal/mol; E_{HOMO} is in eV. ^b HOMO energy of the $[\text{Cu}^{\text{I}}\text{L}]^+$ computed at the ω -B97XD/def2-TZVP level of theory in acetonitrile using the CPCM solvation model. ^c Percent buried volume of the ligand computed from the DFT-optimized geometry of the $[\text{Cu}^{\text{I}}\text{L}]^+$.⁷⁰ ^d Distortion energy of the CuL catalyst in the ISET transition state with respect to the ground state $[\text{Cu}^{\text{I}}\text{L}]^+$. ^e Distortion energy of the CuL catalyst in the $[\text{BrCu}^{\text{II}}\text{L}]^+$ complex with respect to the ground state $[\text{Cu}^{\text{I}}\text{L}]^+$.

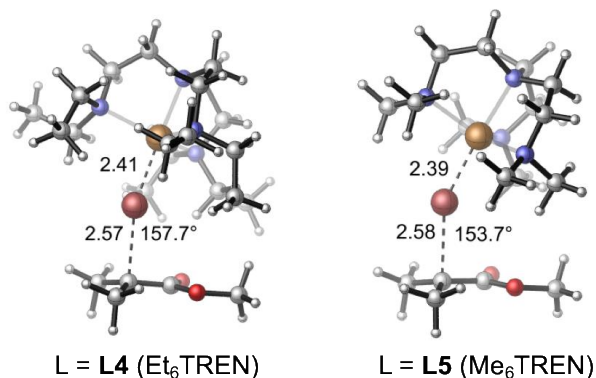


Figure 2-14 Optimized geometries of ISET transition states with TREN family ligands

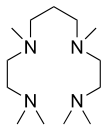
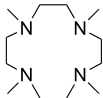
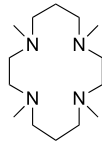
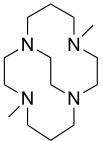
2.3.3.3 Ligand Backbone Flexibility Effect

Finally, we considered a series of tetradentate Cyclam family ligands (**L6-L9**) to investigate the effect of ligand backbone flexibility (Table 2-3). Albeit their similar electronic and steric properties, these ligands have significantly different reactivities in Cu-ATRP. Experimental kinetic data showed that the reactivity decreases with augmented backbone flexibility.⁶⁸ For example, the Cu complex with the most rigid ligand, Cyclam-B, is among the most active catalysts for Cu-ATRP, while the complex with structurally-similar acyclic ligand N[2,3,2] is six orders of magnitude less reactive. This reactivity trend was successfully reproduced by the computed transition state energies ($\Delta G_{\text{DFT}}^\ddagger$). The computed distortion energies ($\Delta E_{\text{dist(TS)}}$) indicated the low reactivities with the more flexible ligands (**L6** and **L7**) are mainly due to the high distortion energy of the CuL catalyst in the ISET transition state. In reactions with **L6**, **L7**, and **L8**, the CuL catalyst is distorted from a tetrahedral geometry in the Cu^I ground state to a square pyramidal geometry in the ISET transition state (Figure 2-15). In contrast, the ligand conformation remains similar in reaction with the more rigid ligand **L9**, leading to a much smaller distortion energy.

Because of its significant role on reactivity, a specific parameter should be included in the predictive model to describe the effect of ligand backbone flexibility. However, to the best of our knowledge, parameters specifically for ligand flexibility effects have not been developed in the literature. Here, we found the computed distortion energy of CuL in the ISET transition state ($\Delta E_{\text{dist(TS)}}$) and in the [Br-Cu^{II}L]⁺ product ($\Delta E_{\text{dist(BrCu}^{\text{II}}\text{L)}}$) can both adequately describe the ligand flexibility effect. Because the ISET transition states are late (*vide supra*) and product-like, an excellent linear correlation between $\Delta E_{\text{dist(TS)}}$ and $\Delta E_{\text{dist(BrCu}^{\text{II}}\text{L)}}$ for all 9 aforementioned ligands is observed (Figure 2-16). Because the computation of $\Delta E_{\text{dist(BrCu}^{\text{II}}\text{L)}}$ does not require optimization of

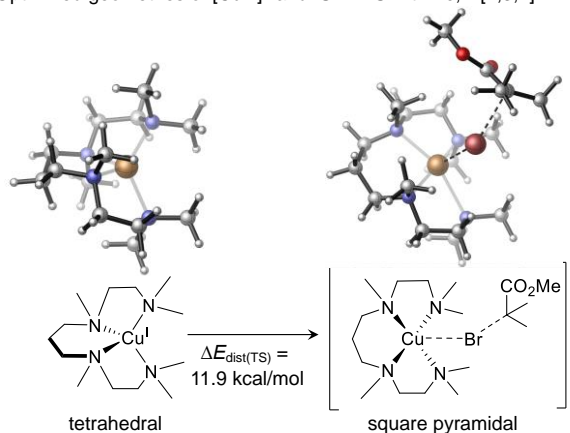
the ISET transition state geometry and thus is much more feasible, $\Delta E_{\text{dist}}(\text{BrCu}^{\text{II}}\text{L})$ was chosen as a parameter to describe the ligand flexibility effect.

Table 2-3 Flexibility effects of the Cyclam family ligands^a

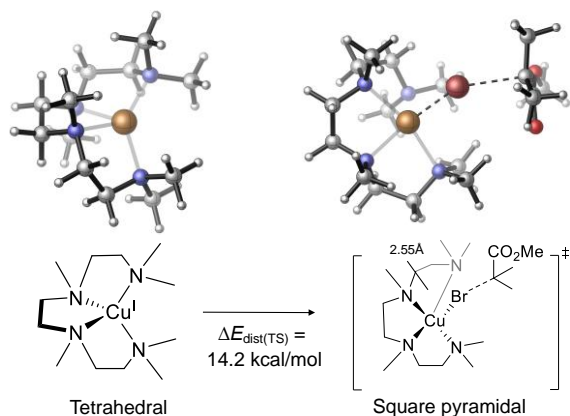
<div style="display: flex; justify-content: space-around; align-items: flex-end;"> <div style="text-align: center;">  <p>L6: N[2,3,2] $k_{\text{act}} = 1.2 \times 10^{-3}$</p> </div> <div style="text-align: center;">  <p>L7: N[2,2,2] $k_{\text{act}} = 0.14$</p> </div> <div style="text-align: center;">  <p>L8: Me₄Cyclam $k_{\text{act}} = 0.67$</p> </div> <div style="text-align: center;">  <p>L9: Cyclam-B $k_{\text{act}} = 710$</p> </div> </div>						
ligand	$\Delta G_{\text{exp}}^{\ddagger}$	$\Delta G_{\text{DFT}}^{\ddagger}$	E_{HOMO}^b	$V_{\text{bur}}\%$ ^c	$\Delta E_{\text{dist}}(\text{TS})^d$	$\Delta E_{\text{dist}}(\text{BrCu}^{\text{II}}\text{L})^e$
N[2,3,2]	21.5	27.5	−7.12	48.4	11.9	14.4
N[2,2,2]	18.6	26.4	−7.26	45.6	14.2	17.0
Me ₄ Cyclam	17.7	20.3	−6.92	49.6	7.0	9.0
Cyclam-B	13.6	16.8	−6.81	47.6	4.0	5.2

^a All Gibbs free energies and distortion energies are in kcal/mol; E_{HOMO} is in eV. ^b HOMO energy of the $[\text{Cu}^{\text{I}}\text{L}]^+$ computed at the ω -B97XD/def2-TZVP level of theory in acetonitrile using the CPCM solvation model. ^c Percent buried volume of the ligand computed from the DFT-optimized geometry of the $[\text{Cu}^{\text{I}}\text{L}]^+$.⁷⁰ ^d Distortion energy of the CuL catalyst in the ISET transition state with respect to the ground state $[\text{Cu}^{\text{I}}\text{L}]^+$. ^e Distortion energy of the CuL catalyst in the $[\text{BrCu}^{\text{II}}\text{L}]^+$ complex with respect to the ground state $[\text{Cu}^{\text{I}}\text{L}]^+$.

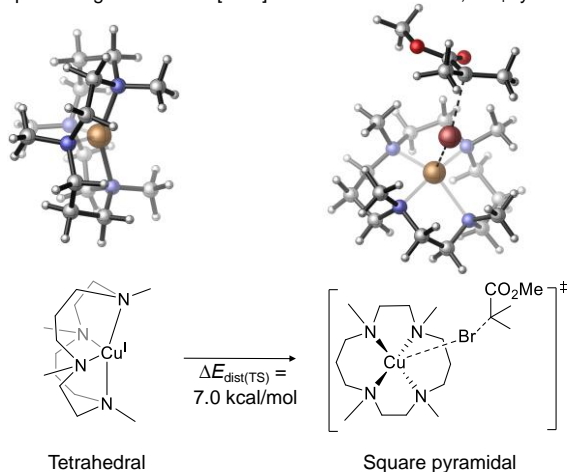
a. Optimized geometries of $[\text{Cu}^{\text{I}}\text{L}]^+$ and ISET TS with **L6**, N[2,3,2]



b. Optimized geometries of $[\text{Cu}^{\text{I}}\text{L}]^+$ and ISET TS with **L7**, N[2,2,2]



c. Optimized geometries of $[\text{Cu}^{\text{I}}\text{L}]^+$ and ISET TS with **L8**, Me₄Cyclam



d. Optimized geometries of $[\text{Cu}^{\text{I}}\text{L}]^+$ and ISET TS with **L9**, Cyclam-B

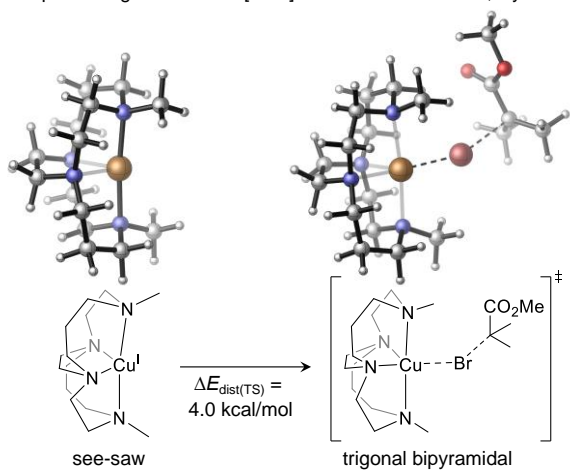


Figure 2-15 Optimized geometries of Cu^{I} catalysts and ISET transition states with Cyclam family ligands

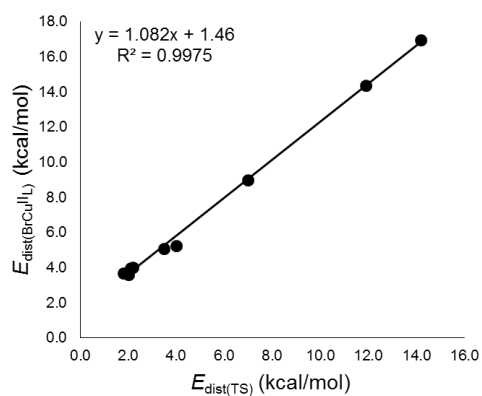


Figure 2-16 Correlation of $\Delta E_{\text{dist(TS)}}$ and $\Delta E_{\text{dist(BrCuIL)}}$ for 9 ligands in the training set

2.3.3.4 Predictive model for ligand effect on reactivity

Through the detailed analysis of computed transition state structures and energies, we not only uncovered the factors that affect reactivity, but also identified appropriate parameters to describe each type of ligand effects. Therefore, these theoretical insights allowed us to establish a simple mathematical equation using only three parameters to predict the reactivity of the structurally diverse Cu-ATRP catalysts, namely, the HOMO energy of the $[\text{Cu}^{\text{I}}\text{L}]^+$ catalyst (E_{HOMO}), the percent buried volume ($V_{\text{bur}}\%$), and the distortion energy of CuL in the $[\text{BrCu}^{\text{II}}\text{L}]^+$ complex (ΔE_{dist}). Using the nine ligands discussed above (**L1-L9**) as the training set, eq. 2-7 was developed using multivariate linear regression by correlating the experimental activation free energies with these three calculated parameters (Figure 2-17). The rest of the ligands in Figure 8 were then used as test sets to validate the predictive model.

$$\Delta G_{\text{predicted}}^{\ddagger} = -4.50 \times E_{\text{HOMO}} + 0.45 \times V_{\text{bur}}\% + 0.48 \times \Delta E_{\text{dist}} - 41.0 \quad (\text{eq.2-7})$$

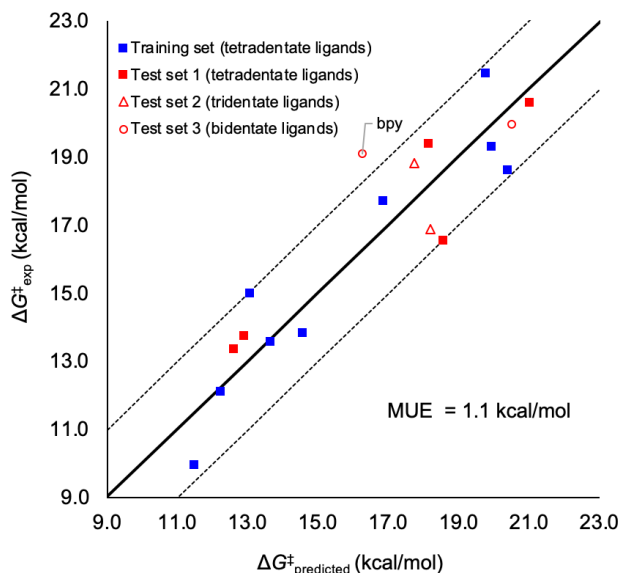


Figure 2-17 Predictive model for ligand effect on Cu-ATRP reactivity

Overall, a good correlation between the predicted activation free energies ($\Delta G_{\text{predicted}}^\ddagger$) and the experimentally derived activation free energies ($\Delta G_{\text{exp}}^\ddagger$). For all 18 ligands studied, the mean unsigned error (MUE) of the predicted activation free energy is 1.1 kcal/mol. Although the training set only contains tetradentate ligands, eq. 2-7 performed well for tetradentate as well as tridentate ligands in the test set. The barriers for all tetradentate and tridentate ligands from either the training set or the test set were correctly predicted within ± 2 kcal/mol error ranges (between the two dash lines). This is very promising to Cu-ARTP ligand discovery since tetra- and tridentate ligands form the most reactive Cu complexes for ATRP. The less accurate prediction for the bidentate bpy ligand⁷¹ might be due to the fact that it only contains 100% sp^2 N and thus is structurally different from the training set tetradentate ligands.

To further understand the impact of each factor on the reactivity, the computed parameters of all 18 ligands are shown using the green-yellow-red color scale in **Table 2-4**. Here, green indicates a positive effect to enhancing the reactivity, while red indicates a negative effect as compared with other investigated ligands. In terms of electronic effect, ligands with a greater number of chelating sp^3 N atoms are generally more effective due to their stronger donicity. For example, the all- sp^3 N cyclam-family ligands (Cyclam-B, Me₄Cylam, N[2,2,2], N[2,3,2], and N[3,2,3]) have HOMO values between -6.81 eV to -7.26 eV, while the sp^3/sp^2 hybrid ligands such as TPMA ligands have lower HOMO values ranging from -7.36 eV to -7.66 eV. Similarly, two TREN-type ligands (Me₆TREN and Et₆TREN) have higher HOMO than TPMA ligands. Although not among the most electronically activated ligands, TPMA ligands are advantageous due to their less steric repulsions and high rigidity with low $V_{\text{bur}}\%$ and ΔE_{dist} values. Therefore, five of the seven most reactive ligands ($\Delta G_{\text{exp}}^\ddagger \leq 15.0$ kcal/mol) are TPMA derivatives. In fact, we found steric effect ($V_{\text{bur}}\%$) and backbone flexibility effect (ΔE_{dist}) have greater contribution to the

reactivity than the electronic effect (E_{HOMO}) from the standardized multivariate linear equation (see eq. 2-8). Furthermore, the electronic properties of TPMA ligands can be easily tuned by substitution on the pyridine rings. As such, TPMA^{NMe₂} is the most reactive ligand discovered so far because it has low steric repulsion and distortion penalty, and favorable electronic effect via incorporation of strong electron-donating groups.

Table 2-4 Calculated electronic (E_{HOMO}), steric ($V_{\text{bur}}\%$), and backbone flexibility (ΔE_{dist}) parameters for all 18

ligands ^a					
ligand	$\Delta G_{\text{exp}}^{\ddagger}$	$\Delta G_{\text{predicted}}^{\ddagger}$	E_{HOMO}	$V_{\text{bur}}\%$	ΔE_{dist}
TPMA ^{NMe₂}	10.0	11.5	-7.36	39.0	3.7
TPMA ^{*3}	12.1	12.2	-7.41	40.3	3.6
TPMA ^{*2}	13.4	12.6	-7.49	40.0	3.8
Cyclam-B	13.6	13.6	-6.81	47.6	5.2
TPMA ^{*1}	13.7	12.9	-7.57	39.6	4.0
Me ₆ TREN	13.8	14.5	-7.34	45.7	4.0
TPMA	15.0	13.0	-7.66	39.2	4.0
BPED	16.6	18.5	-7.48	41.8	14.7
PMDTA	16.9	18.2	-7.46	40.9	14.9
Me ₄ Cyclam	17.7	16.8	-6.92	49.6	9.0
N[2,2,2]	18.6	20.3	-7.26	45.6	17.0
BPMPA	18.8	17.7	-7.82	37.5	13.9
bpy	19.1	16.3	-7.78	38.6	10.2
Et ₆ TREN	19.3	19.9	-7.33	56.5	5.1
TPMA ^{Ph}	19.4	18.1	-7.62	47.7	7.0
TMEDA	20.0	20.5	-7.39	47.4	14.4
N[3,2,3]	20.6	21.0	-7.21	51.1	13.6
N[2,3,2]	21.5	19.7	-7.12	48.4	14.4

^a All calculated parameters are color-coded. Green indicates quantities that are favorable for reactivity, and red indicates quantities that lead to lower reactivity. All energies are in kcal/mol. E_{HOMO} are in eV.

$$\Delta G_{\text{predicted}}^{\ddagger} = -1.17 \times E_{\text{HOMO}} + 2.56 \times V_{\text{bur}}\% + 2.42 \times \Delta E_{\text{dist}} + 15.7 \quad (\text{eq.2-8})$$

Here the raw computed parameters were standardized to the normalized values with zero mean and unit variance, i.e. $\text{Parameter}' = \frac{\text{Parameter}_{\text{raw}} - \mu}{\sigma}$, where μ and σ are the mean and the standard deviation of individual parameters for 9 ligands in the training set, respectively.

2.4 Conclusion

In this study, we demonstrated a computational approach to develop predictive mathematical equations for the reactivity of catalysts and initiators in Cu-ATRP, a widely used controlled radical polymerization reaction. We report the first DFT calculations of the inner-sphere electron transfer transition state, which involves a halogen atom transfer between a dormant alkyl halide chain end and the Cu(I) catalyst. An in-depth computational analysis revealed a few key factors controlling the stability of the ISET transition state, and thus the activation rate constant. The ISET transition state involves a bent geometry of the Cu \cdots Br \cdots R bond, which leads to an enhanced non-covalent interaction between the ancillary *N*-donor ligand and the alkyl halide chain end. As such, the stability of the ISET transition state is sensitive to the steric properties of the ligand. A substantial amount of charge transfer from the Cu(I) catalyst to the alkyl halide is observed in the transition state, which indicates the ISET process can be facilitated by stronger donor ligands. In addition, ISET transition states with flexible multidentate ligands, such as the acyclic ligand N[2,3,2], suffer from a high catalyst distortion energy due to the different ligand conformations in the [Cu^IL]⁺ resting state and the ISET transition state. With these mechanistic insights into the factors controlling reactivity, we identified three parameters, namely the percent buried volume, HOMO energy of the [Cu^IL]⁺ catalyst, and the catalyst distortion energy of the [Br-Cu^{II}L]⁺ complex, to describe the steric, electronic, and flexibility effects of ligand,

respectively. We developed a three-variable linear equation using these three DFT-computed parameters to predict the reactivity of a structurally diverse set of Cu-ATRP catalysts. The predicted activation barriers are within ± 2 kcal/mol of the experimental values for 17 out of 18 ligands used in the training and test sets.

The same computational approach was used to develop a predictive equation for initiator effects on reactivity. Since the DFT calculations indicated a late ISET transition state with a substantial R–X bond stretch and a strong X \cdots Cu interaction, the stability of the transition state is expected to be affected by both the R–X bond dissociation energy (BDE) and the halogenophilicity of the [Cu^IL]⁺ complex. These conclusions were reaffirmed by a distortion/interaction model analysis which indicated a good correlation between the R–X distortion energy to reach the ISET transition state and the in general stronger interaction energies between Br and Cu than between Cl and Cu in the ISET transition states. Using these mechanistic insights, a two-variable linear equation was developed using R–X BDE and Cu–X halogenophilicity as parameters to describe the effects of R–X bond stretch and Cu–X interactions, respectively.

Taken together, we demonstrated the use of mechanistic insights derived from transition state calculations to guide the development of predictive mathematical relationships for reactivities of Cu-ATRP. We expect our models to shed light on the rational ligand design and discovery for Cu-ATRP. Similar approaches may be employed to benefit the ligand design in other transition metal-catalyzed reactions.

3.0 COMPUTATIONAL STUDY ON THE MECHANISM OF PHOTO-INDUCED METAL-FREE ATOM TRANSFER RADICAL POLYMERIZATION (*photo*ATRP)

3.1 Introduction

Photoredox catalysts have been extensively investigated for water splitting,⁷² solar cells⁷³ and photodynamic therapy⁷⁴ in inorganic and materials chemistry. Photoredox catalysts were also used in organic synthesis⁷⁵ and polymerization,^{76,77} especially photoinduced electron transfer (PET)-RAFT.⁷⁸ Recently, photoinduced metal-free ATRP has been catalyzed by photoredox catalysts, such as *fac*-[Ir(ppy)₃] (**1**, ppy = 2-pyridylphenyl, in Figure 3-1) and 10-phenylphenothiazine (**2**, Ph-PTZ, in Figure 3-1). A simplified activation/deactivation mechanism for photoredox mediated ATRP (*photo*ATRP) is shown in Figure 3-2. Both ground state catalysts (Cat) can be excited to form very strong reductants (Cat*, $E_{1^+/1^*}^{\ominus} = -1.73$ V vs. SCE, $E_{2^{\bullet+}/2^*}^{\ominus} = -2.10$ V vs. SCE), which can reduce the alkyl halide (R-X) initiator to form the catalyst radical cation species (Cat^{•+}) and the propagating alkyl radical (R[•]) which initiates polymerization. The Cat^{•+} is a strong oxidant ($E_{1^+/1}^{\ominus} = 0.77$ V vs. SCE, $E_{2^{\bullet+}/2}^{\ominus} = 0.68$ V vs. SCE), able to deactivate the propagating alkyl radicals and regenerate the ground state catalyst. It should be noted that these two types of photoredox catalysts have much more negative potential values than the Cu-based ATRP catalyst (e.g. **3**, [Cu^I(TPMA*³)]⁺, in Figure 3-1, which is the most reactive Cu catalyst reported so far), indicating much greater reactivity in the activation of alkyl halides. Although it has been proved that the activation and deactivation in Cu-catalyzed ATRP occurs via inner-sphere electron transfer (ISET) only (see details in Section 2.3.1), the activation of photo-induced ATRP is believed to occur via dissociative electron transfer process due to the strong oxidation potential

of photoredox catalysts. But the mechanisms of deactivation in *photo*ATRP is unveiled yet. Both outer-sphere electron transfer (OSET) and ISET pathways would be possible.

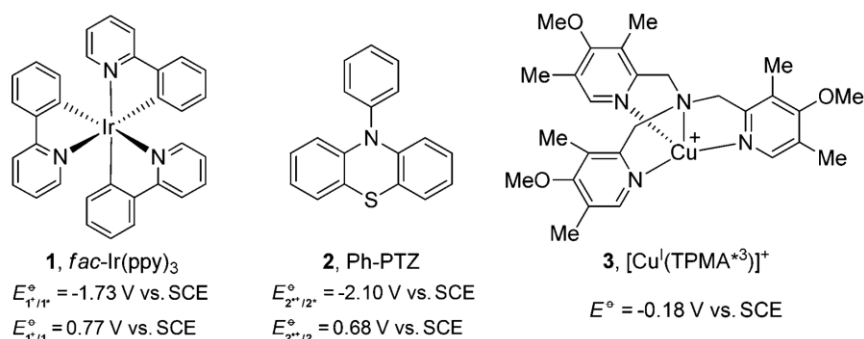


Figure 3-1 Structures of photoredox catalyst 1 and 2 and a Cu-catalyzed ATRP catalyst 3

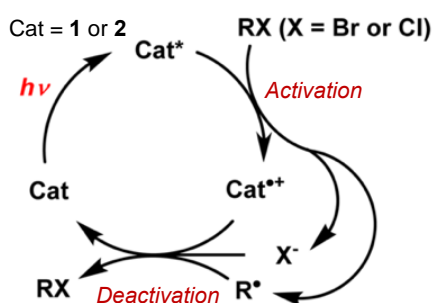
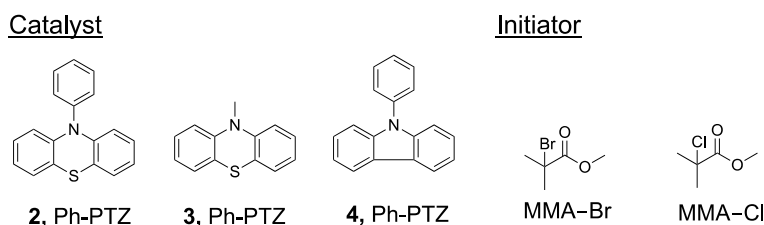


Figure 3-2 Simplified activation/deactivation mechanism for photoredox-mediated ATRP reactions

Matyjaszewski's group developed a series of phenothiazine derivatives and other related compounds as photoredox catalysts to conduct metal-free ATRP of methyl methacrylate (MMA). Figure 3-3 shows the structures, ATRP reactivities, and the dispersity of the polymerization for representative photoredox catalysts. Compare to the background reaction (Entry 1), all these catalysts are effective in the activation step, but not all of them participated efficiently in the deactivation step. In addition, the chloride-based initiator might not be suitable for photoinduced system that is inefficient to deactivate the propagating radicals, and lead to a large dispersity.



Entry	Catalyst	<i>R-X</i>	Activation	Deactivation	M_w/M_n
1	None	MMA-Br		–	2.25
2	2, Ph-PTZ	MMA-Br	+	+	1.50
3	2, Ph-PTZ	MMA-Cl	+	–	3.44
4	3, Me-PTZ	MMA-Br	+	+/-	1.79
5	4, Ph-CBZ	MMA-Br	+	–	1.89

Figure 3-3 The structures, ATRP reactivities, and the dispersity of polymerization for representative photoredox catalysts.

In order to obtain further insights into the mechanisms of the activation and the deactivation processes, and to explore factors that affect the efficiency of the photoredox catalysts in ATRP, Marcus Theory and DFT calculations were carried out to study the activation/deactivation reactions with selected catalysts **2** (Ph-PTZ), **3** (Me-PTZ), and **4** (Ph-CBZ).

3.2 Computational Methods

3.2.1 DFT calculations

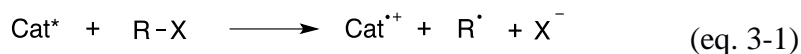
All DFT calculations were performed with the Gaussian 09 software package.⁵⁴ Geometries were optimized using the B3LYP⁸ functional and the 6-31G(d)¹³ basis set in solution. The SMD²¹ solvation model and DMF solvent were used in the calculations. Single point energies were calculated using M06-2X¹¹ and 6-311++G(3df,2p) and the SMD solvation model in DMF.

Reported Gibbs free energies and enthalpies in solution include thermal corrections computed at 298 K and are computed at the standard concentration (1 mol/L). The CCSD(T) benchmark calculations were performed with MOLPRO Version 2012.1.⁷⁹

3.2.2 Marcus Theory Calculations

1. Activation of photoinduced ATRP

The strongly negative values for $E_{\text{Cat}^{\bullet+}/\text{Cat}^*}^{\ominus}$ (see Figure 3-1) suggested the viability of an OSET for the activation of photoinduced ATRP (eq. 3-1). This reaction involves a concerted dissociative electron transfer (DET) to R-X, as consolidated in the literature for the reductive cleavage of alkyl halides.^{80,81} Therefore, assessment of activation barriers cannot be made by a straight forward application of the well-known Marcus theory for electron-transfer processes. A modified model of Marcus theory, developed by Savéant⁵⁵, is available and is currently used to analyze the dynamics of DET processes.



Given the ion-dipole interaction between the two fragments of DET, R^{\bullet} and X^- , in the solvent cage, a “sticky” model⁸¹ was used to estimate the DET barriers (eq. 3-2).

$$\Delta G_{\text{DET}}^{\ddagger} = \Delta G_0^{\ddagger} \left(1 + \frac{\Delta_r G^{\ominus} - D_p}{4\Delta G_0^{\ddagger}} \right)^2 \quad (\text{eq. 3-2})$$

$$\Delta G_0^{\ddagger} = \frac{(\sqrt{D_{\text{R-X}}} - \sqrt{D_p})^2 + \lambda_0}{4} \quad (\text{eq. 3-3})$$

$$\lambda_0 = A \times [(2r_{\text{Cat}})^{-1} + (2r_{\text{RX}})^{-1} - (r_{\text{Cat}} + r_{\text{RX}})^{-1}] \quad (\text{eq. 3-4})$$

where ΔG_0^{\ddagger} is the intrinsic barrier of the reaction that can be derived from eq. 3-3; λ_0 is the solvent reorganization energy that can be calculated with eq. 3-4 where $A=95 \text{ kcal mol}^{-1} \text{ \AA}$ was used, r_{Cat} is the radii of the catalyst and r_{RX} is the effective radii of R-X, which was calculated from the

equation $r = (2r_{RX} - r_X)r_X/r_{RX}$ ^{82,83}; $\Delta_r G^\ominus$ is the reaction energy for the DET process (eq. 3-1), which can be either calculated from DFT or obtained from standard potentials of the donor and acceptor redox couples in the ground state using Weller equation⁸⁴ (eq. 3-5); D_p is the interaction energy between R^\bullet and X^- in the solvent cage, and the experimental data of D_p for MMA-Br and MMA-Cl were used in our calculation⁸⁵; D_{R-X} is the R-X bond dissociation enthalpy calculated using DFT.

$$\Delta_r G^\ominus = F(E_{Cat^{\bullet+}/Cat}^\ominus - E_{RX/R^\bullet+X^-}^\ominus - E_{hv}) - \frac{N_A e^2}{4\pi\epsilon_0\epsilon r} \quad (\text{eq. 3-5})$$

where N_A is the Avogadro constant, e is the elementary charge, ϵ_0 is the permittivity of vacuum and ϵ the relative permittivity of the solvent at 25 °C. The last term is the Columbic energy experienced by the radical ion pair at distance r . The distance was approximated to the sum of the radii of the two hitting molecules $r = r_{Cat^*} + r_{RX}$). All radii were obtained from the computed volume of the molecules, based on an isoelectron density surface of 0.001 electrons/Bohr³ using the DFT-optimized structures. The relevant thermodynamic, kinetic and geometric parameters used in the calculations are listed in Table 3-1.

Table 3-1 Thermodynamic, kinetic and geometric parameters for the homogenous electron transfer to R-X.

Cat	R-X	r_{Cat}	r_{RX}	r	λ_o	D_{RX}	$E_{Cat^{\bullet+}/Cat^*}^\ominus$	$E_{RX/R^\bullet+X^-}^\ominus$	D_p
		Å	Å	Å	kcal/mol	kcal/mol	V vs. SCE	V vs. SCE	kcal/mol
2* , Ph-PTZ*	MMA-Br	4.49	3.42	2.80	14.53	58.7	-1.97	-0.52	0.24
2* , Ph-PTZ*	MMA-Cl	4.49	3.47	2.68	15.07	75.7	-1.97	-0.76	0.69
3* , Me-PTZ*	MMA-Br	3.94	3.42	2.80	14.94	58.7	-1.96	-0.52	0.24
4* , Ph-CBZ	MMA-Br	4.37	3.42	2.80	14.60	58.7	-1.91	-0.52	0.24

For example, when the catalyst is 2*, the numerical calculations are shown as follows:

$$\begin{aligned}\Delta_r G^\ominus &= 96485 \text{ C mol}^{-1} (0.815 + 0.52 - 2.787) \text{ V} \\ &\quad - \frac{6.022 \times 10^{23} \text{ mol}^{-1} (1.602 \times 10^{-19} \text{ C})^2}{4 \times 3.1416 \times 8.854 \times 10^{-12} \text{ J}^{-1} \text{ C}^2 \text{ m}^{-1} \times 37.78 \times (4.49 + 3.42) \times 10^{-10} \text{ m}} \\ &= -144.7 \text{ kJ mol}^{-1} = -34.59 \text{ kcal mol}^{-1}\end{aligned}$$

Alternatively, the reaction energy can be calculated by DFT: $\Delta_r G^\ominus = -30.4 \text{ kcal/mol}$

$$\Delta G_0^\ddagger = \frac{(\sqrt{D_{\text{RX}}} - \sqrt{D_{\text{p}}}) + \lambda_o}{4} = \frac{(\sqrt{58.7} - \sqrt{0.24}) + 14.53}{4} \text{ kcal mol}^{-1} = 16.49 \text{ kcal mol}^{-1}$$

$$\lambda_o = 95 \left(\frac{1}{2r_{\text{Cat}}} + \frac{1}{2r} - \frac{1}{r_{\text{Cat}} + r} \right) \text{ kcal mol}^{-1} = 14.53 \text{ kcal mol}^{-1}$$

Thus,

$$\Delta G_{\text{DET}}^\ddagger = \Delta G_0^\ddagger \left(1 + \frac{\Delta_r G^\ominus - D_{\text{p}}}{4\Delta G_0^\ddagger} \right)^2 = 16.49 \times \left(1 + \frac{-34.59 - 0.24}{4 \times 16.49} \right)^2 = 3.7 \text{ kcal/mol}$$

Alternatively, $\Delta G_{\text{DET}}^\ddagger = 4.7 \text{ kcal/mol}$ if using DFT calculated $\Delta_r G^\ominus = -30.4 \text{ kcal/mol}$

2. Deactivation of photoinduced ATRP

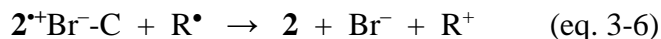
Five possible mechanisms were considered for the deactivation process: (a) inner-sphere electron transfer (ISET) mechanism; (b) dissociative electron transfer (DET); (c) outer-sphere electron transfer between Cat^+X^- and R^\bullet (OSET-I), followed by addition of X^- to R^+ ; (d) outer-sphere electron transfer between Cat^+ and R^\bullet (OSET-II), followed by recombination of R^+ and X^- ; (e) the termolecular associative electron transfer (AET-ter). The barriers for last four mechanisms are estimated using Marcus Theory. Geometric and thermodynamic parameters for the three catalysts **2**, **3** and **4** and for the initiators MMA-Br and MMA-Cl are provided in Table

3-2. Detailed calculations are here reported for the **2** + MMA-Br catalytic system, while results for all investigated systems are presented in Table 3-2.

Table 3-2 Parameters used for the determination of energy barriers for the deactivation pathways.

Catalyst Complex	D_{RX} (kcal mol ⁻¹)	Radius (Å)			$\Delta_r G^\circ$ (kcal mol ⁻¹)		
		MMA•	Cat• ⁺ -X ⁻	Cat• ⁺	OSET-I	OSET-II	DET
2•⁺Br⁻	20.9	3.0	4.6	4.1	13.6	8.7	8.4
2•⁺Cl⁻	36.0	3.0	4.5	4.1	11.0	8.7	7.5
3•⁺Br⁻	20.1	3.0	4.0	4.0	11.3	7.5	8.2
4•⁺Br⁻	6.8	3.0	4.1	4.4	-3.5	-7.4	-6.6

DET deactivation



Sticky interaction does not occur here, because there is no interaction between Br⁻ and a radical. The activation Gibbs free energy is therefore given by:

$$\Delta G_{\text{DET}}^\ddagger = \Delta G_0^\ddagger \left(1 + \frac{\Delta_r G^\circ}{4\Delta G_0^\ddagger} \right)^2$$

$\Delta_r G^\circ = 8.4 \text{ kcal mol}^{-1}$ from DFT optimizations, whereas ΔG_0^\ddagger for a dissociative electron transfer can be calculated from the bond dissociation energy and solvent reorganization energy:

$$\Delta G_0^\ddagger = \frac{D_{\mathbf{2^{\bullet+}Br^-} \cdot \mathbf{C}} + \lambda_o}{4}$$

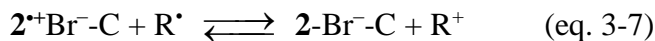
Using the computed $D_{\mathbf{2^{\bullet+}Br^-} \cdot \mathbf{C}}$ value of $6.3 \text{ kcal mol}^{-1}$ and λ_o calculated as

$$\lambda_o = 95[(2r_{\text{Cat}})^{-1} + (2r_{\text{R}^\bullet})^{-1} - (r_{\text{Cat}} + r_{\text{R}^\bullet})^{-1}] = 95 \left(\frac{1}{2 \cdot 4.56} + \frac{1}{2 \cdot 2.95} - \frac{1}{4.56 + 2.95} \right) = 13.87 \text{ kcal mol}^{-1}$$

leads to

$$\Delta G_{\text{DET}}^\ddagger = \left(5.04 \text{ kcal mol}^{-1} \right) \left(1 + \frac{13.6}{4 \times 5.04} \right)^2 = 14.13 \text{ kcal mol}^{-1}$$

OSET-I deactivation



As in the case of OSET-II, no bond is being broken or formed during electron transfer. Thus, Marcus theory of outer-sphere electron transfer can be applied to the OSET-I deactivation pathway:

$$\Delta G_{\text{OSET-I}}^{\ddagger} = \Delta G_0^{\ddagger} \left(1 + \frac{\Delta_r G^{\circ}}{4\Delta G_0^{\ddagger}} \right)^2$$

$\Delta_r G^{\circ} = 13.6 \text{ kcal mol}^{-1}$ from DFT optimizations, and $\Delta G_0^{\ddagger} = \frac{\lambda_0}{4} = 3.47 \text{ kcal/mol}$ with λ_0 given by

$$\lambda_0 = 95[(2r_{\text{Cat}})^{-1} + (2r_{\text{R}^{\bullet}})^{-1} - (r_{\text{Cat}} + r_{\text{R}^{\bullet}})^{-1}] = 95 \left(\frac{1}{2 \cdot 4.56} + \frac{1}{2 \cdot 2.95} - \frac{1}{4.56 + 2.95} \right) = 13.87 \text{ kcal mol}^{-1}$$

with these values $\Delta G_{\text{OSET-I}}^{\ddagger}$ is calculated as

$$\Delta G_{\text{OSET-I}}^{\ddagger} = (3.47 \text{ kcal mol}^{-1}) \left(1 + \frac{13.66}{4 \times 3.47} \right)^2 = 13.6 \text{ kcal mol}^{-1}$$

OSET-II deactivation



Similar to OSET-I mechanism, the barrier of OSET-II mechanism can be calculated as:

$$\Delta G_{\text{OSET-II}}^{\ddagger} = \Delta G_0^{\ddagger} \left(1 + \frac{\Delta_r G^{\circ}}{4\Delta G_0^{\ddagger}} \right)^2$$

where $\Delta_r G^{\circ} = 8.6 \text{ kcal mol}^{-1}$ from DFT optimizations, and $\Delta G_0^{\ddagger} = \frac{\lambda_0}{4} = 3.56 \text{ kcal/mol}$ with λ_0 given by

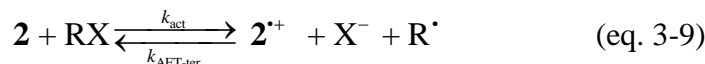
$$\lambda_0 = 95[(2r_{2^{*+}})^{-1} + (2r_{\text{R}^{\bullet}})^{-1} - (r_{2^{*+}} + r_{\text{R}^{\bullet}})^{-1}] = 95 \left(\frac{1}{2 \cdot 4.08} + \frac{1}{2 \cdot 2.95} - \frac{1}{4.08 + 2.95} \right) = 14.23 \text{ kcal mol}^{-1}$$

lead to

$$\Delta G_{\text{OSET-II}}^{\ddagger} = (3.56 \text{ kcal mol}^{-1}) \left(1 + \frac{8.6}{4 \times 3.56} \right)^2 = 9.16 \text{ kcal mol}^{-1}$$

AET-ter deactivation

The exact reverse process of metal-free ATRP activation (eq. 3-1), which is a dissociative electron transfer (DET), is an associative electron transfer involving a termolecular encounter (AET-ter):



The activation free energy of the termolecular deactivation ($\Delta G_{\text{AET-ter}}^{\ddagger}$) is

$$\Delta G_{\text{AET-ter}}^{\ddagger} = \Delta G_0^{\ddagger} \left(1 - \frac{\Delta G^{\circ} + D_{\text{p}}}{4\Delta G_0^{\ddagger}} \right)^2$$

where $\Delta G_0^{\ddagger} = 16.5 \text{ kcal mol}^{-1}$ and the DFT-calculated reaction free energy is $\Delta_{\text{r}}G^{\circ} = 33.6 \text{ kcal mol}^{-1}$. In addition, $D_{\text{p}} = 0.24 \text{ kcal mol}^{-1}$. Therefore, calculation of the activation free energy gives $\Delta G_{\text{AET-ter}}^{\ddagger} = 3.9 \text{ kcal mol}^{-1}$.

3.3 Results and Discussion

3.3.1 Activation Mechanism

The activation processes involving the reactions of excited **2***, **3***, and **4*** with MMA-Br and **2*** with MMA-Cl (eq. 3-1, Cat = **2***, **3***, or **4***, RX = MMA-Br or MMA-Cl) were examined through DFT calculations. Here, MMA-Br and MMA-Cl were used as a model of the PMMA growing chain end. Geometry optimizations of the radical anions of MMA-Br and MMA-Cl led to dissociation to the free MMA radical and Br⁻ or Cl⁻. The instability of the RX radical anion confirms that ET from Cat* to RX (eq. 3-1) is a concerted dissociative ET process. The standard

free energies obtained from DFT calculations for the dissociative ET to form R^\bullet and X^- were used to estimate the activation free energies according to the sticky model of DET (eq. 3-2). Table 3-3 reports the computed reaction free energies and activation free energies. The agreement between the computed activation energies and those derived from experimental data, is not very good in some cases. This could be due to the uncertainty in the computed free energy of solvation of ions. For instance, experimental solvation free energy of bromide anion in DMF⁸⁶, $\Delta G^{\text{sol}}_{\text{exp}}(\text{Br}^-)$, is -59.9 kcal mol⁻¹, while the value computed by the SMD solvation model, $\Delta G^{\text{sol}}_{\text{DFT}}(\text{Br}^-)$, is -54.1 kcal mol⁻¹. On the contrast, the $\Delta G^{\text{sol}}_{\text{exp}}(\text{Cl}^-) = -63.1$ kcal mol⁻¹,⁸⁶ while the $\Delta G^{\text{sol}}_{\text{DFT}}(\text{Cl}^-) = -66.3$ kcal mol⁻¹. All reactions are highly exergonic and have low barrier for the dissociative electron transfer. This confirms that DET activation is highly likely with all three catalysts.

Table 3-3 Computed reaction energies, and activation free energies in the activation process, with the existed catalysts, 2*, 3*, and 4*.

Cat	R-X	$\Delta_r G^{\text{a}}$	$\Delta G^{\ddagger \text{b}}$	$\Delta_r G^{\text{a} \text{c}}$	$\Delta G^{\ddagger \text{c}}$
2* , Ph-PTZ	MBiB	-30.4	4.7	-34.6	3.7
2* , Ph-PTZ	MCiB	-30.9	6.8	-29.1	7.2
3* , Me-PTZ	MBiB	-32.0	4.4	-34.4	3.8
4* , Ph-CBZ	MBiB	-25.1	6.3	-33.3	4.0

^a Reaction free energies (in kcal mol⁻¹) are computed at the M06-2X/6-311++G(3df,2p)//B3LYP/6-31G(d) level of theory. The SMD solvation model with DMF solvent was used in geometry optimizations and single point energy calculations. ^b Activation barriers of DET pathway calculated from eq. 3-2 using DFT-calculated reaction energies. ^c Calculated from eq. 3-2 using experimental reaction energies.

3.3.2 Structures and stabilities of intermediates $\text{Cat}^{\bullet+}$ and $\text{Cat}^{\bullet+}\text{X}^-$

A key factor that determines whether the deactivation occurs through an inner-sphere or an outer-sphere ET mechanism is the structural stability of the resulting radical cation and halide

anion complex $\text{Cat}^{\bullet+}\text{X}^-$ formed after the activation. The optimized geometries and energies of the radical cation $2^{\bullet+}$ and two lowest energy isomers of the $2^{\bullet+}\text{Br}^-$ complex are shown in Figure 3-4. The DFT calculations indicate that both isomers of $2^{\bullet+}\text{Br}^-$ have similar Gibbs free energies in solution as the dissociated radical cation $2^{\bullet+}$ and Br^- . Isomer $2^{\bullet+}\text{Br}^-$ -C (C stands for covalent) has stronger covalent interactions between the S atom in the catalyst and the bromide anion, while the interactions between the catalyst radical cation and the bromide in isomer $2^{\bullet+}\text{Br}^-$ -I (I stands for ionic) are mostly ionic. This difference is supported by the shorter S-Br distance (3.03 vs 4.04 Å, respectively) and a greater S-Br Wiberg bond index (0.12 vs 0.01, respectively) in $2^{\bullet+}\text{Br}^-$ -C than in $2^{\bullet+}\text{Br}^-$ -I. In addition, the Br atom in the covalent complex $2^{\bullet+}\text{Br}^-$ -C is less negatively charged and has greater spin density than the Br in the ionic complex (Figure 3-4). Due to the ionic character of $2^{\bullet+}\text{Br}^-$ -I, the geometry of the phenothiazine rings in the ionic complex $2^{\bullet+}\text{Br}^-$ -I is almost completely planar, the same as the dissociated radical cation.⁸⁷ In contrast, the phenothiazine is bent in $2^{\bullet+}\text{Br}^-$ -C, which resembles the geometry of **2** in the ground state. Nonetheless, the relative Gibbs free energies, the S-Br distances and bond orders all indicate that the interactions between the catalyst radical cation and the bromide anion in $2^{\bullet+}\text{Br}^-$ in solution are relatively weak, and $2^{\bullet+}$, $2^{\bullet+}\text{Br}^-$ -C, and $2^{\bullet+}\text{Br}^-$ -I may all exist in equilibrium.

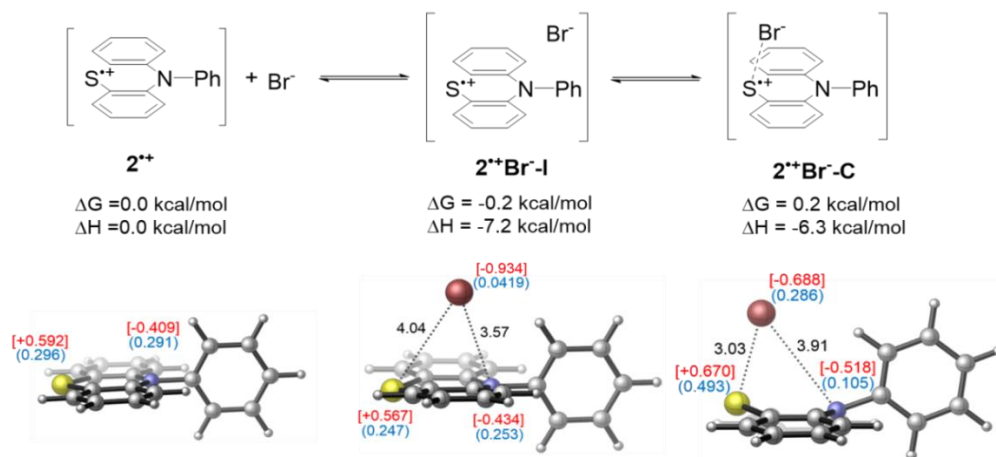


Figure 3-4^a Optimized geometries of the radical cation $2^{\bullet+}$ and the zwitterionic radical complex $2^{\bullet+}\text{Br}^-$.

^aThe bond lengths are provided in Å. NPA atomic charges of Br, S, and N atoms are shown in red in square brackets. Spin densities are shown in blue in parentheses.

Similarly, calculations on other $\text{Cat}^{\bullet+}\text{X}^-$ complexes indicate that their dissociation to the separated radical cation and halide anion are all facile. The most stable isomers of $2^{\bullet+}\text{Cl}^-$, $3^{\bullet+}\text{Br}^-$, and $4^{\bullet+}\text{Br}^-$ complexes are all within ± 1 kcal/mol of the separated ionic species in terms of Gibbs free energies. The optimized geometries, computed spin densities, charges, and Wiberg bond indices of these ion pair complexes are shown in Figure 3-5.

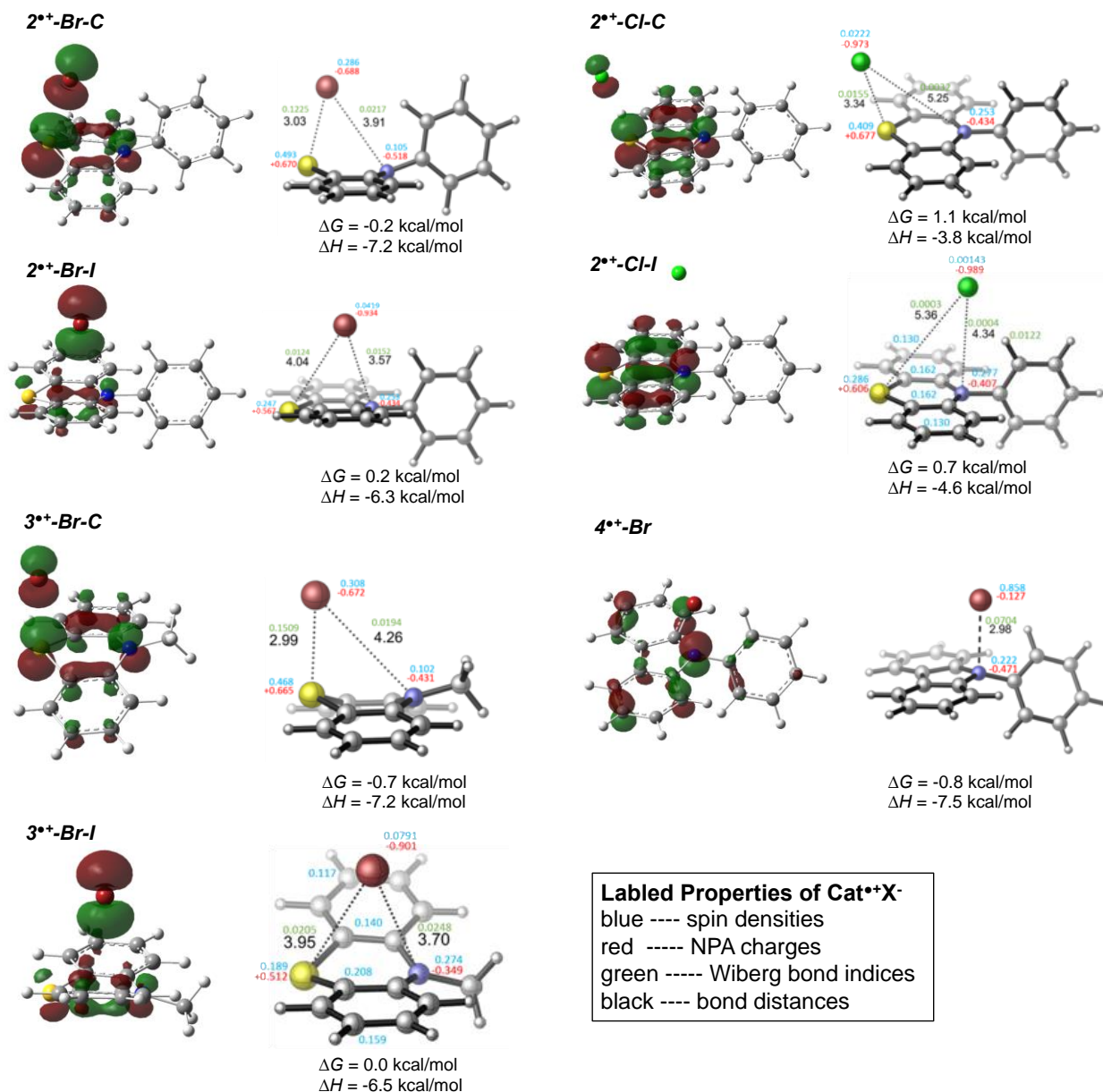


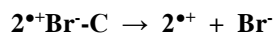
Figure 3-5 HOMO, spin densities, NPA charges, and Wiberg bond indices of Cat^{•+}X⁻

3.3.3 Benchmark calculations of dissociation energy of 2^{•+}Br⁻

To evaluate the accuracy of the computational method, we investigated the relative stabilities of 2^{•+}Br⁻-C and 2^{•+} at different levels of theory (Table 3-4). DMF was used as the solvent in the SMD and CPCM solvation model calculations. The method used in this study, M06-

2X/6-311++G(3df,2p), gives good agreement with the high-level DF-LCCSD(T)-F12/cc-pVTZ calculations in the gas phase (entries 6 vs. 8). Although the dissociation of the ion pair is highly unfavorable in the gas phase, the dissociation becomes slightly exergonic in solution. Calculations using the CPCM solvation model (entry 5) predicted the dissociation to be exergonic by 4.7 kcal mol⁻¹, while prediction of the SMD model is that dissociation is only slightly exergonic by 0.2 kcal/mol (entry 3). Using the experimental solvation free energy of bromide anion in DMF,⁸⁶ along with the solvation free energies computed with SMD for **2^{•+}Br⁻C** and **2^{•+}**, the calculations (entry 4) indicate that the dissociation of the ion pair is exergonic by 6.0 kcal/mol. These calculations suggest that the exact value of the ion pair dissociation energy in solution is challenging for computations, due to the relatively large errors in the solvation free energy calculations with the explicit solvation models. Based on the previous benchmark study by Cramer and Truhlar,⁸⁸ the average errors for SMD model for cations and anions in non-aqueous solutions are about 6 and 3 kcal mol⁻¹, respectively. The average errors for CPCM are greater than 10 kcal mol⁻¹ for cations, and about 4 kcal mol⁻¹ for anions. Considering these reported average errors, the SMD solvation model was used in the present study. It should be noted that the conclusions in this study will not be affected by the choice of the solvation model in the DFT calculations. Most importantly, the termolecular pathway in deactivation is always the most favorable regardless of the solvation model used.

Table 3-4 The relative stabilities of $2^{\bullet+}\text{Br}^-$ -C and $2^{\bullet+}$ at different levels of theory.



Entry	Method ^a	Dissociation energy (kcal mol ⁻¹)	
		ΔG	ΔH
1	B3LYP/6-311G(3df,2p) (SMD)	-0.8	5.7
2	M06-2X/6-311G(3df,2p) (SMD)	2.3	8.8
3	M06-2X/6-311++G(3df,2p) (SMD)	-0.2	6.3
4	M06-2X/6-311++G(3df,2p) (SMD) ^b	-6.0	0.5
5	M06-2X/6-311++G(3df,2p) (CPCM)	-4.7	1.9
6	M06-2X/6-311++G(3df,2p) (gas)	83.3	89.8
7	DF-LUCCSD(T)/cc-pVDZ (gas)	87.5	94.0
8	DF-LUCCSD(T)/cc-pVTZ (gas)	82.3	88.9

^aMethod used in singlet point energy calculations. Geometries were optimized with B3LYP/6-31G(d) with the SMD solvation model in DMF for all calculations. Thermal corrections to G and H at 298 K were calculated using the same level of theory as in geometry optimization. ^b Experimental solvation free energy of bromide anion in DMF ($\Delta G_{\text{sol(Br}^-)} = -59.9$ kcal mol⁻¹) was used in place of the value computed by the SMD solvation model ($\Delta G_{\text{sol(Br}^-)} = -54.1$ kcal mol⁻¹).

3.3.4 Deactivation Mechanism

Since the DFT calculations have shown that both the catalyst radical cation $2^{\bullet+}$ and the ion pair complex $2^{\bullet+}\text{Br}^-$ exist in solution, five possible deactivation mechanisms of the MMA^\bullet with $2^{\bullet+}$ or with $2^{\bullet+}\text{Br}^-$ -C⁸⁹ were evaluated (Figure 3-6): (a) inner-sphere electron transfer (ISET) mechanism through a concerted Br atom transfer from $2^{\bullet+}\text{Br}^-$ -C to MMA^\bullet *via* transition state **TS1**; (b) dissociative electron transfer (DET) from MMA^\bullet to $2^{\bullet+}\text{Br}^-$ -C to form the carbocation, **2** and Br^- , followed by recombination of MMA^+ and Br^- to generate MMA-Br ; (c) outer-sphere electron transfer (OSET-I) from MMA^\bullet to $2^{\bullet+}\text{Br}^-$ -C to form an anionic **2** Br^- complex and MMA^+ , followed by dissociation to the catalyst **2** and Br^- , and counterions recombination; (d) outer-

sphere electron transfer from MMA^\bullet to the dissociated radical cation $\mathbf{2}^{\bullet+}$ (OSET-II); and (e) associative electron transfer from $\mathbf{2}^{\bullet+}$ to MMA^\bullet and Br^- to form the ground-state catalyst **2** and MMA-Br , involving a termolecular encounter (AET-ter). ISET and AET-ter pathways produce RX without the formation of any intermediate, while all other ET pathways (DET, OSET-I, and OSET-II) generate the R^+ cation, which then rapidly recombines with the halide anion to form RX . The transition state for the concerted Br atom transfer (ISET) was optimized with DFT calculations. The barriers for the outer-sphere electron transfer pathways (OSET-I, OSET-II) were calculated using the Marcus theory (Details are seen in Section 3.2)

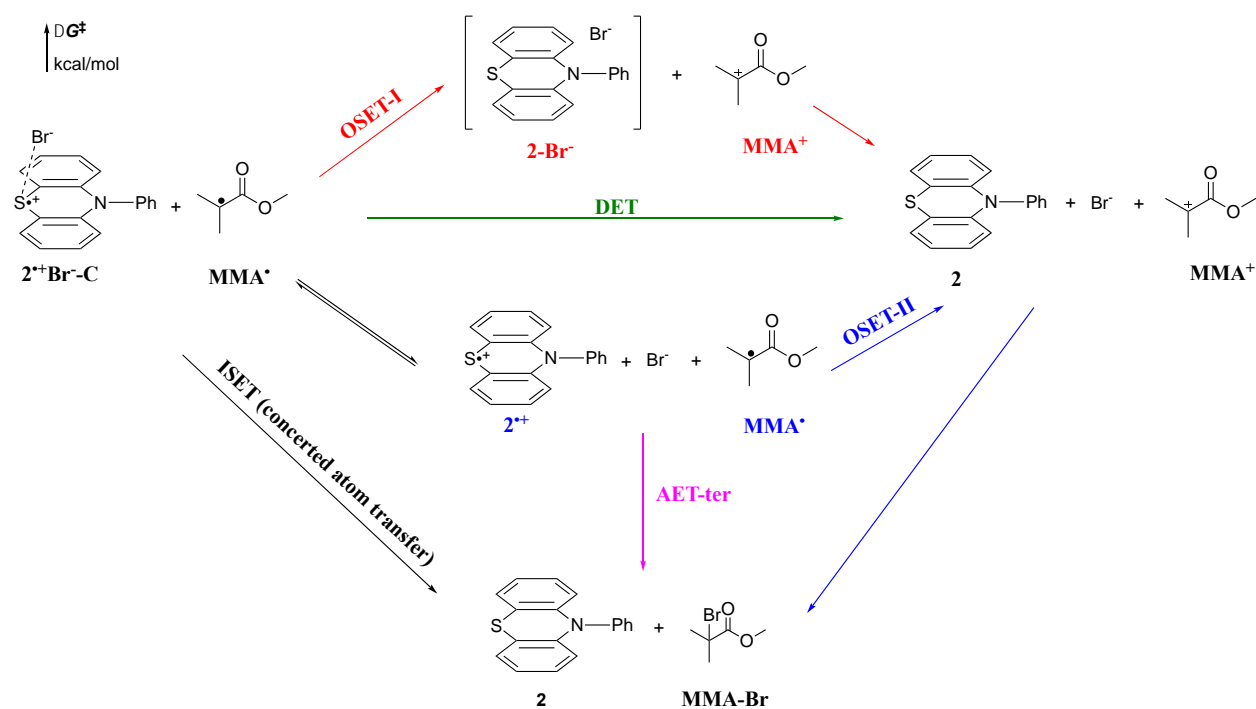


Figure 3-6 Possible deactivation mechanisms in photoinduced metal-free ATRP

The computed reaction energy profiles of the five pathways are summarized in Figure 3-7. The ISET pathway requires 10.5 kcal/mol of activation free energy with respect to the ion pair complex $\mathbf{2}^{\bullet+}\text{Br}^{-}\cdot\text{C}$. The optimized geometry of the ISET transition state (**TS1**) is shown in Figure 3-7. Among the other four outer-sphere electron transfer pathways, AET-ter pathway of radical

cation $2^{\bullet+}$, MMA^\bullet and Br^- forming **2** and MMA-Br has the lowest activation energy, 3.9 kcal/mol. The electron transfer from MMA^\bullet to the dissociated radical cation $2^{\bullet+}$ (OSET-II) requires 9.2 kcal/mol of activation free energy, which is close to the activation energy of ISET pathway (10.5 kcal/mol). The other two reaction pathways, OSET-I and DET, have higher barriers of 13.6 and 13.4 kcal/mol, respectively.

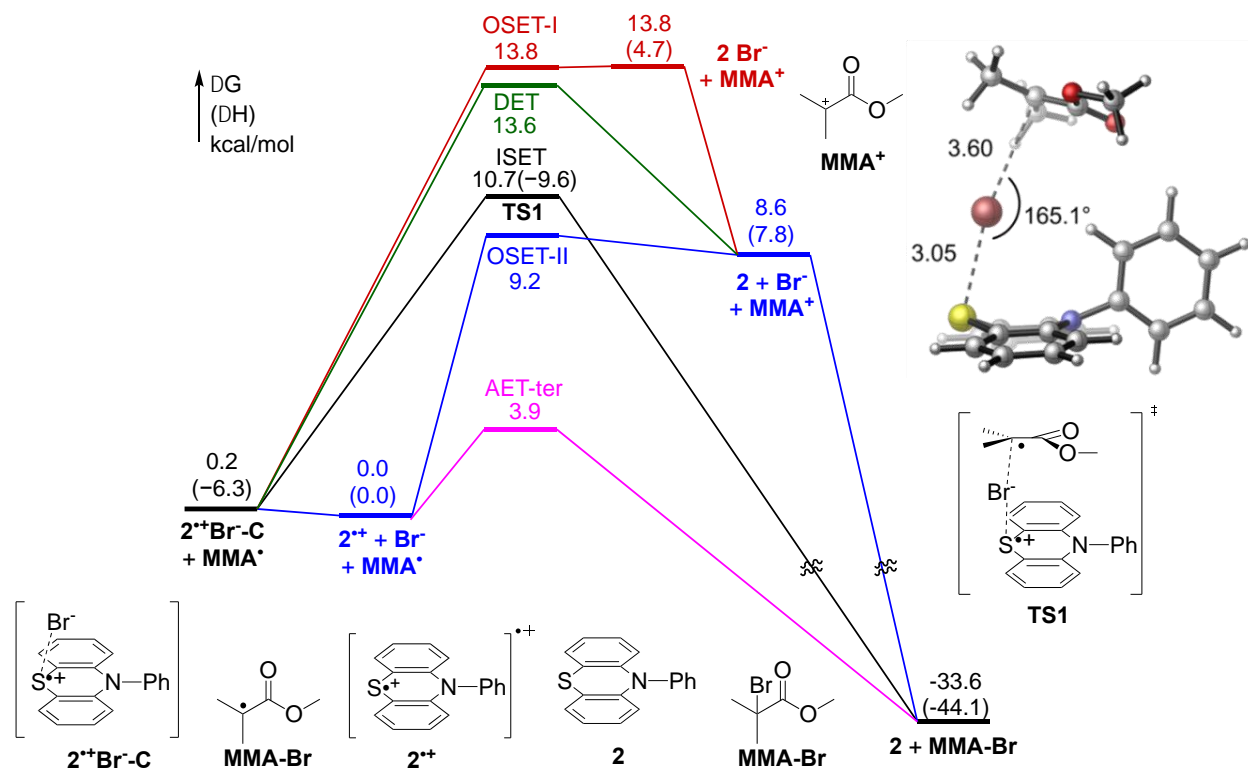


Figure 3-7 Computed reaction energy profiles for the reaction of $2^{\bullet+}\text{Br}^- \text{-C}$ with MMA^\bullet

These calculations suggest AET-ter to be the most favored pathway. Additionally, some experimental observations are not consistent with the OSET-I, OSET-II, and DET mechanisms. First, the reaction of **2** with ECIPA (alkyl chloride) was not as controlled as the reaction between **2** and EBPA (alkyl bromide). The effects of the halide (better control with RBr than RCl) rule out the possibility of OSET-II, which should not be affected by the nature of X^- . Also, the lack of

oligomer formation during the polymerization provides further evidence against the formation of MMA^+ , thus ruling out not only OSET-II pathway but also DET and OSET-I pathways.

3.3.5 Computed Barriers for Deactivation Processes with Different Catalysts.

The computed activation energies of deactivation reactions with different catalysts are summarized in Table 3-5.

Table 3-5 Computed activation energies for possible deactivation pathways in metal-free ATRP with photoredox catalysts 2, 3, and 4.

Entry	catalyst	initiator	activation energy for deactivation pathways ΔG^\ddagger (ΔH^\ddagger) kcal/mol				
			ISSET ^a	AET-ter ^b	DET ^a	OSET-I ^a	OSET-II ^b
1	2, Ph-PTZ	MMA-Br	10.5 (−3.3)	3.9	13.4	13.6	9.2
2	2, Ph-PTZ	MMA-Cl	12.5 (−2.4)	6.1	16.5	11.2	9.2
3	3, Me-PTZ	MMA-Br	9.0 (−2.6)	3.7	13.2	11.5	8.3
4	4, Ph-CBZ	MMA-Br	8.3 (−3.5)	1.0	2.5	2.0	0.8

^a Activation energies with respect to the ion pair complex $\text{Cat}^{\bullet+}\text{X}^-$; ^b Activation energies with respect to separated ions $\text{Cat}^{\bullet+}$ and X^- , which energies are within 1 kcal/mol of the ion pair complex.

In reactions with MMA-Br, the computed ΔG^\ddagger values are only minimally affected when switching the catalyst from Ph-PTZ **2** to Me-PTZ **3** (entries 1 and 3). However, catalyst **3** did not perform as well as catalyst **2** (cf. entry 4, Figure 3-3), probably due to the slow decomposition of $\mathbf{3}^{\bullet+}$.⁹⁰ In the reaction with catalyst Ph-CBZ **4** (entry 4), all five possible pathways have much lower ΔG^\ddagger than the corresponding pathways with **2** and **3**, due to the greater oxidizing power of $\mathbf{4}^{\bullet+}$ compared to $\mathbf{2}^{\bullet+}$ and $\mathbf{3}^{\bullet+}$. However, **4** is a very inefficient deactivator in the polymerization of MMA (cf. entry 5, Figure 3-3). The poor performance of **4** is due to the instability of the radical

cation $4^{\bullet+}$ shown by cyclic voltammetry (CV) experiments. In fact, CV of **4** has shown an irreversible response even at high scan rates indicating that $4^{\bullet+}$ has a very short lifetime. Computational results indicate that the homolytic cleavage of $4^{\bullet+}\text{Br}^-$ to form ground state **4** and a Br radical is exergonic by -1.5 kcal/mol (Figure 3-8). In contrast, the homolytic dissociation of other $\text{Cat}^{\bullet+}\text{X}^-$ complexes to form free halogen radical is much more unfavorable, and requires 14.0 kcal/mol, 13.8 kcal/mol, and 30.8 kcal/mol for $2^{\bullet+}\text{Br}^-$, $3^{\bullet+}\text{Br}^-$, and $2^{\bullet+}\text{Cl}^-$, respectively.

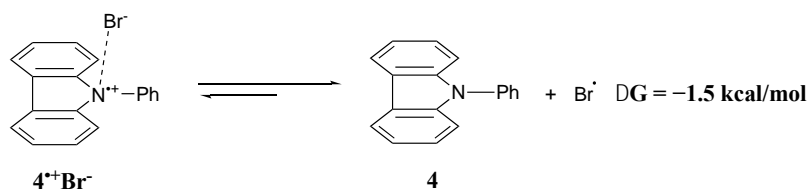


Figure 3-8 Homolytic cleavage of the $11^{\bullet+}\text{Br}^-$ complex indicates the instability of $4^{\bullet+}$.

The effects of halides on the barriers of ISET and all other four deactivation pathways were then explored. When MMA-Cl is used in place of MMA-Br as the initiator in the reaction with catalyst **2** (entry 2, Table 3-5), the barriers of the ISET, AET-ter and DET pathways increase, whereas that of OSET-I decreases. As expected, the halide has no effect on the barrier of the OSET-II pathway. While the most preferred pathway with MMA-Cl is still AET-ter, the activation free energy is 2.2 kcal/mol higher than the reaction with MMA-Br.

In summary, the computed activation energies indicate that the AET-ter pathway is preferred in the deactivation process. A combination of more effective catalysts and initiator, such as **2** and **3** with MMA-Br (entries 1 and 3 in Table 3-5) leads to low barriers for the AET-ter pathway. The performance of catalyst **4** is impeded by the instability of both radical cation $4^{\bullet+}$ and complex $4^{\bullet+}\text{Br}^-$ that can readily dissociate to form a free bromine radical. The poor control of polymerization of MMA with alkyl chloride as ATRP initiator provides a further support for the

AET-ter deactivation mechanism. With **2** as catalyst, ΔG^\ddagger of AET-ter increases by 2.2 kcal/mol when Cl^- is used in place of Br^- . This will result in a considerable lowering of the deactivation rate, which might not be able to outrun radical-radical termination reactions.

3.4 Conclusion

Photoinduced metal-free ATRP provides a fascinating avenue to synthesize well-defined polymers in the absence of residual transition metals. In this study, we conducted the first computational study on the mechanism of activation and deactivation of photoinduced ATRP via DFT and Marcus theory calculations. The structures and stabilities of the radical cation intermediates are analyzed with DFT studies. Our computational studies suggest that the activation process undergoes a dissociative electron transfer (DET) mechanism while an associative electron transfer involving a termolecular encounter (AET-ter) is favored in the deactivation process. This detailed study provides a deeper understanding of the chemical processes of metal-free ATRP that can aid the design of better catalytic systems.

4.0 COMPUTATIONAL STUDY ON *CIS*-SELECTIVE ENTROPY-DRIVEN RING-OPENING METATHESIS POLYMERIZATION OF MACROCYCLIC OLEFINS TOWARDS SEQUENCED POLYMERS

4.1 Introduction

Synthetic copolymer structure is rarely defined at the monomer level despite evidence from biological systems that monomer sequence controls properties.^{91,92,93} Challenges inherent in the synthesis of sequenced copolymers and a lack of general understanding of structure-function relationships has inhibited progress in this area. Instead, efforts have been largely directed at creating novel monomers and controlling architectures on longer length scales. While these efforts have been extremely fruitful, the control of sequence would expand exponentially the library of polymers available to address needs in fields like energy, medicine, environmental science and nanotechnology.^{94,95}

The idea of applying ring-opening metathesis polymerization (ROMP) to generate sequenced polymers has been previously explored by Hillmyer and Hawker groups.^{96,97} However, limitations of existing methodologies include the lack of molecular weight control, the narrow range of acceptable monomers, and/or the inclusion of property-dominating linker groups. Recently, Meyer's group successfully synthesized sequenced polyesters via entropy-driven ROMP (ED-ROMP)⁹⁸ of strainless macromonomers with metathesis-active olefin linker (**P**) and imbedded monomer sequences of lactic (**L**), glycolic (**G**) as well as an ethylene glycol (**Eg**) unit (Figure 4-1). This method produced materials with perfect sequence retention, but a moderate degree of molecular weight control with dispersities of ~ 1.3 , and low conversion of 35%. To

further enhance the molecular weight control, an enhanced version of ED-ROMP, which is termed as selectivity-enhanced ED-ROMP (SEED-ROMP)⁹⁹, was developed by Meyer's group by replacing *trans*-olefins with *cis*-olefins in the metathesis-active segment to prepare macromonomers (Figure 4-2). Under the SEED-ROMP conditions, first-order kinetics and narrow dispersities of ~1.1 were observed with high conversion of up to 90%.

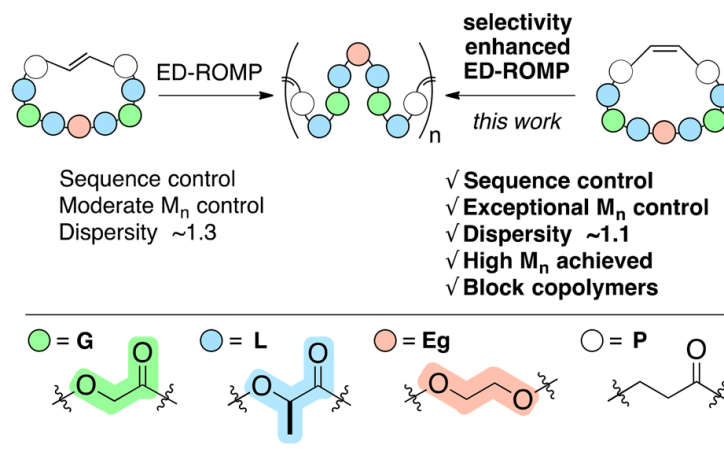


Figure 4-1 Advantages of SEED-ROMP Preparation of Sequenced Polyesters Relative to ED-ROMP

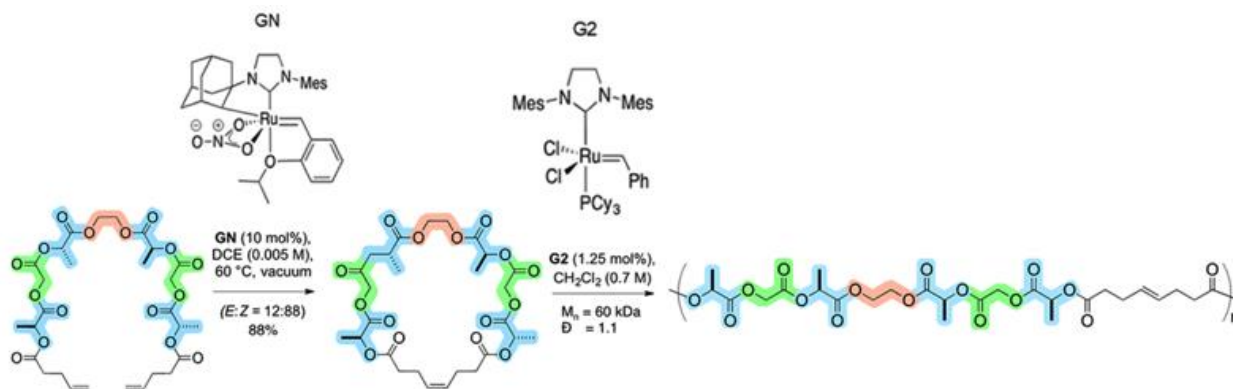


Figure 4-2 *Cis*-Selective Ring-Closing Metathesis and SEED-ROMP to Generate a Sequenced Copolymer

The underlying source of selectivity enhancement that occurs during SEED-ROMP is presumably related to the improved rate of reaction with the *cis*-macromonomer relative to the *trans*-macromonomer.¹⁰⁰ As the enhanced reactivity of the *cis*- relative to the *trans*-

macromonomers is the basis for SEED-ROMP and key to the near-living nature of the polymerization, we performed computational studies to investigate the origins of the difference. A few factors are known to affect the kinetic reactivity of ROMP, including ring strain,¹⁰¹ sterics, and electronic effects.¹⁰² However, both the *cis*- and *trans*- macromonomers are expected to have very small ring strain energies, and, thus, the higher reactivity of the *cis*-isomer should not be promoted by ring-strain. In addition, the electronic and steric properties of *cis*- and *trans*-double bonds in the macromonomers are similar. Based on the known kinetic reactivity of acyclic *cis*- and *trans*-olefins in cross-metathesis and ethenolysis,^{103, 104, 105} the local steric and electronic environments of the *cis*- and *trans*- macromonomers are not expected to play a key role in differentiating their reactivities in ROMP. We surmised the conformational flexibility of the macrocyclic monomers might affect the ability of the C=C double bond to approach the Ru catalyst, which then could, in turn, affect the reactivity of *cis*- and *trans*-macromonomers. Due to the flexible nature of the macrocyclic monomers, a large number of conformers exist in the resting state and many of these conformers are expected to provide access to the [2+2] cycloaddition transition state. Thus, a complete understanding of the relative reactivity of *cis*- versus *trans*-macromonomers requires the evaluation of all ground state conformers and their relative reactivity in the [2+2] cycloaddition transition state.

As the large number of transition state conformers is highly challenging for conventional transition state calculations, we utilized a combined molecular dynamics/density functional theory (MD-DFT) approach to investigate the conformational flexibility of the monomers using MD trajectory simulations combined with evaluation of reactivities of each monomer conformer using DFT.

4.2 Computational Methods

4.2.1 DFT calculations

All DFT calculations were performed using the Gaussian 09 software package.⁵⁴ The B3LYP⁸ density functional and a mixed basis set of LANL2DZ¹⁴ for Ru and 6-31G(d)¹³ basis set for other atoms were used in geometry optimizations and energy calculations. All DFT calculations were done in gas phase.

4.2.2 Molecular Dynamics simulations

Molecular dynamics (MD) simulation were performed using AMBER 10 software¹⁰⁶ and the general AMBER force field (GAFF).¹⁰⁷ The partial charges for the **cyclic-Eg(LGLG)₂** were generated within the *antechamber* module of AMBER 14 by fitting the electrostatic potential generated at the HF/6-31G(d) level by the RESP model.¹⁰⁸ The charges were calculated based on the Merz-Singh-Kollman scheme¹⁰⁹ using Gaussian 09. The starting structures for the MD simulation were the DFT-calculated lowest-energy conformers from a pool of low-energy conformers generated via conformational search within MacroModel¹¹⁰ in Schrodinger software package.¹¹¹ The MD simulations were performed in explicit solvent of CH₂Cl₂ by immersing the starting structure in a pre-equilibrated truncated octahedral box of CH₂Cl₂ molecules with an internal offset distance of 10 Å, using the *leap* module,¹¹² which resulted in the addition of around 150 solvent molecules. A two-stage geometry optimization was performed prior to the explicit solvation simulation. First, a short minimization of the CH₂Cl₂ molecules positions, with positional restraints on solute by a harmonic potential with a force constant of 10 kcal mol⁻¹ Å⁻², was

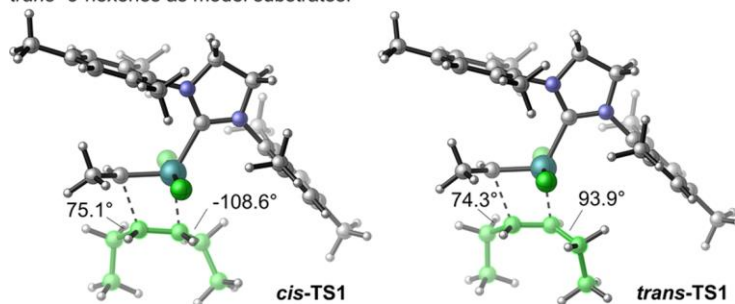
performed. The second stage was an unrestrained minimization of all the atoms in the simulation cell. Then, the systems were gently heated (10-300K) under constant-volume, periodic-boundary conditions and the particle-mesh Ewald approach¹¹³ was used to introduce long-range electrostatic effects. 8 Å cutoff was applied to Lennard-Jones and electrostatic interactions, and harmonic restraints of 10 kcal mol⁻¹ were applied to the solute. Bonds involving hydrogen were constrained with the Shake algorithm,¹¹⁴ and the Andersen equilibration scheme was used to control and equalize the temperature.¹¹⁵ The time step was kept at 2 fs during all stages of the simulation, allowing potential inhomogeneities to self-adjust. Each system was then equilibrated without restraints for 100 ps at a constant pressure of 1 atm. Finally, a 20 ns unrestrained MD trajectory at constant volume and temperature (300 K) was collected and analyzed using the *ptraj* module.

4.3 Results and Discussion

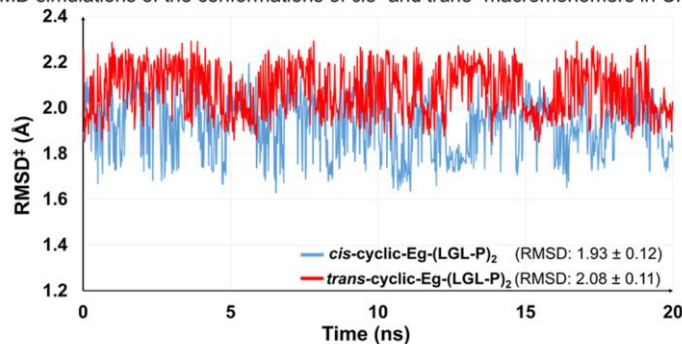
4.3.1 Deviation of Macromonomer's Conformation from Reactive Olefin Geometry

First, we optimized the transition state geometries with DFT methods using *cis*- and *trans*-3-hexene as model substrates that undergo [2+2] cycloaddition 14-electron Ru alkylidene complex derived from the **G2** catalyst (Figure 4-3A). We performed 20 ns MD simulations of ***cis*- and *trans*-cyclic-Eg-(LGL-P)₂** in a dichloroethane solvent box. Snapshots of the MD simulations revealed both active conformers in which the two olefin substituents are placed on the same face of the double bond and inactive conformers with the two olefin substituents on opposite faces (Figure 4-3C).

A. B3LYP/LANL2DZ-6-31G(d) optimized metathesis transition states using *cis*- and *trans*- 3-hexenes as model substrates.



B. MD simulations of the conformations of *cis*- and *trans*- macromonomers in CH₂Cl₂.



† Deviation of highlighted carbon atoms from the reactive olefin geometry in *cis*- and *trans*-TS1.

C. Representative active and inactive conformations of *cis*- and *trans*- macromonomers.

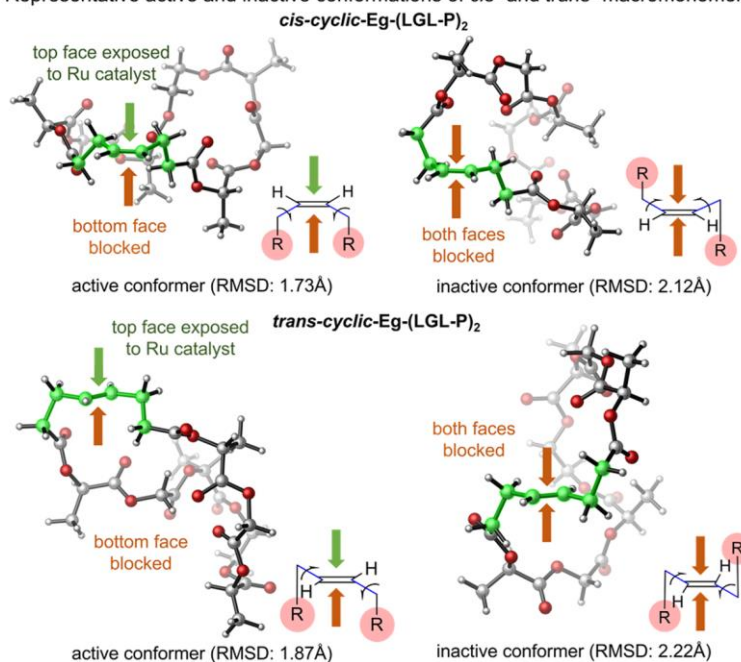


Figure 4-3 Computational study on the conformations and reactivity of *cis*- and *trans*-macromonomers. (A) Optimized transition states of model substrates. (B) Molecular dynamic simulations of *cis*- and *trans*-macromonomers. (C) Representative active and inactive conformers of *cis*- and *trans*-macromonomers.

To evaluate the structural deviations of MD snapshots from reactive olefin geometry in [2+2] cycloaddition, we calculated atomic root-mean-square deviation (RMSD) between the MD snapshots and the geometry of 3-hexene in the transition state (Figure 4-3A) in terms of six carbon atoms (i.e two olefin carbons, and two alpha, and two beta carbons which are highlighted in green in Figure 4-3). As shown in Figure 4-3C, the representative active conformers of *cis*- and *trans*-monomer have smaller RMSD (1.73 Å and 1.87 Å, respectively) than the inactive conformer in both cases (2.12 Å and 2.22 Å, respectively). Thus, the atomic RMSD of the highlighted carbon atoms can be used as the indicator of the macrocyclic olefin reactivity with Ru catalyst in [2+2] cycloaddition. Finally, the atomic RMSD from the all MD snapshots was plotted over time (Figure 4-3B). The *cis*- macromonomer has generally smaller deviation from the reactive conformation which indicates the *cis*-double bond is more exposed to the Ru catalyst.

4.3.2 Estimation of Activation Energies of [2+2] Cycloaddition with Different Conformers of *cis*- and *trans*-Macromonomers

In Section 4.3.1, we revealed that the geometries of the *cis*-macromonomer have smaller deviations from the reactive olefin conformations in the metathesis transition state, indicating greater populations of metathesis-active monomers, than the *trans*-macromonomer. To provide a more quantitative understanding of how monomer conformation affects the metathesis reactivity, we created a model that estimates the activation energy required for each macromonomer conformer to undergo [2+2] cycloaddition with the 14-electron Ru alkylidene complex derived from the **G2** catalyst (Figure 4-4).

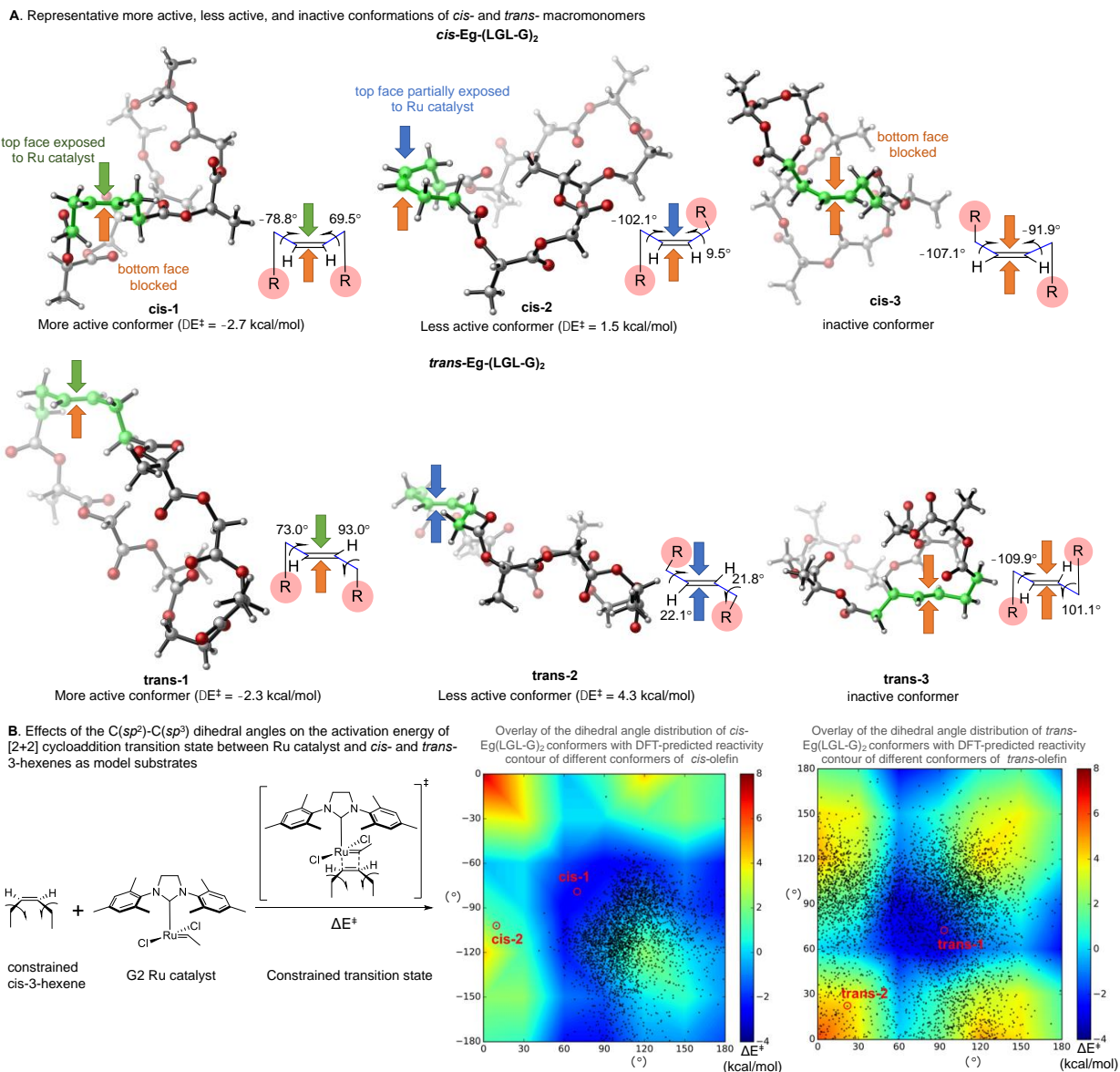


Figure 4-4 Estimation of Activation Energies for Macromonomer's Conformation in ROMP

First, the snapshots of the MD simulations revealed great levels of conformational flexibility in the two dihedral angles (θ and ϕ) for the C-C sigma bonds attached to the alkene. These conformers are expected to exhibit dramatically different reactivity in the [2+2] cycloaddition. Similar to Figure 4-3A, conformers with the two olefin substituents (highlighted in green in Figure 4-4A) placed on the same face of the double bond have exposed C=C double bonds

(e.g. **cis-1**), which are expected to be more reactive with the catalyst. If one of the substituents is placed in the same plane of the double bond, an increased steric repulsion with the Ru catalyst is expected, and, thus, the reactivity should be lower (e.g. **cis-2**). For conformers with two substituents on opposite faces, the C=C double bond is blocked for both, which translates into the lowest reactivity with **G2** (e.g. **cis-3**). Similarly, the dihedral angles (θ and ϕ) are also expected to affect the reactivity of the conformers of the *trans*-macromonomers.

To quantify the effects of the two highlighted dihedral angles on the reactivity of the conformers, we established an activation energy contour by correlating the DFT-calculated activation energies of constrained [2+2] cycloaddition transition states (ΔE^\ddagger) with two varying but fixed dihedral angles (θ and ϕ) for the model system of constrained *cis*- and *trans*-alkenes. The activation energy contours were calculated using a model system of constrained *cis*- and *trans*-3-hexenes and a 14-electron Ru alkylidene complex derived from the **G2** catalyst (Figure 4-4B). All constrained transition states were validated with the imaginary frequency vibration corresponding with the [2+2] cycloaddition process, and their activation energies were color-encoded where the blue indicated the more reactive region while the yellow to red indicated the less reactive region (Figure 4-4B, right).

We next mapped the *cis*- and *trans*-macromonomer conformers from the MD snapshots onto the generated activation energy contour. The activation energy for each conformer was thereby estimated with respect to two corresponding dihedral angles via linear interpolation from the contour. As shown in Figure 4-4B, the conformers of *cis*-macromonomers were primarily localized on the most reactive regions (blue, $\Delta E^\ddagger < 0$ kcal/mol) such as **cis-1** with the estimated activation energy of -2.7 kcal/mol. Only a relatively small fraction of *cis*-conformers were in the less reactive region, colored cyan-to-yellow. For example, **cis-2** with one dihedral angle close to

0, which makes the top face of the double bond more sterically hindered, has a higher activation energy of 1.5 kcal/mol.

In contrast, *trans*-macromonomers were more flexible. The conformers are more dispersed throughout the contour map and have a greater distribution in less reactive regions than the *cis*-MCOs. For instance, **trans-1**, one of the most reactive conformers ($\Delta E^\ddagger = -2.3$ kcal/mol), has the double bond fully exposed to Ru catalyst from the top face. **Trans-2** is less reactive ($\Delta E^\ddagger = 4.3$ kcal/mol), however, with two olefin substitutes placed on the plane of the double bond. This arrangement increases the steric repulsion between the substitutes and the Ru catalyst in their transition state.

4.4 Conclusion

The development of sequence-controlled polymer syntheses is an ongoing effort, in which homogeneity across samples in molecular weight and dispersity is critical. Selectivity-Enhanced Entropy-Driven ROMP (SEED-ROMP), which exploits a more reactive *cis*-olefin metathesis handle, enhanced the living character of the polymerization, improving molecular weight control, decreasing dispersity, and facilitating the preparation of sequenced polymers.

We combined molecular dynamics and density functional theory calculations (MD-DFT) to investigate the origin of enhanced reactivity for *cis*-macrocyclic olefin monomers over the *trans*-monomers. Two computational models were built in our studies. First, we monitored the deviation of MD snapshots for macrocyclic monomers from the reactive olefin geometry in the [2+2] cycloaddition transition states. It was found that the conformers of *cis*-monomers have generally smaller deviations than *trans*-monomers, indicating the larger population of reactive conformers.

Second, by mapping MD snapshots on the activation energy contour of [2+2] cycloaddition, we estimated the activation energies of [2+2] cycloaddition for each conformer of *cis*-monomer and *trans*-monomer, respectively. Our calculations suggested that the higher reactivity of *cis*-macromonomers can be attributed to their more localized conformer ensembles with the majority being reactive conformations for [2+2] cycloaddition in ROMP. It is interesting to note that this finding is subtly different from the intuitive rationale that *cis*-olefins react faster because they are “more accessible” and can more easily approach the metal center. This reasoning is based on a model of the olefin in which the substituents present a singular steric profile rather than a population of profiles and does not take into account the fact that not all coordination modes lead to energetically favorable transition states.

5.0 COMPUTATIONAL STUDY ON THE MECHANISMS, DYNAMICS, AND THE ORIGIN OF REACTIVITY AND SELECTIVITY OF HYDROBORATION OF ALKYNES AND ARYNES WITH N-HETEROCYCLIC CARBENE BORANES (NHC-BORANES)

5.1 Introduction

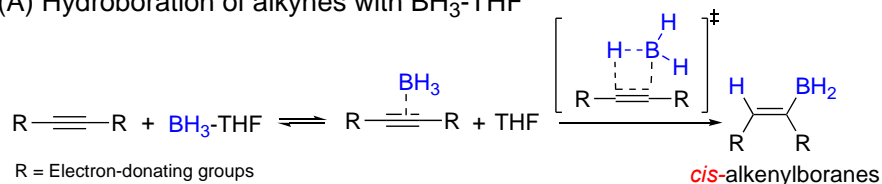
N-heterocyclic carbene boranes (NHC-boranes) are a class of ligated boranes with diverse applications as reactants, reagents, and catalysts in many unique transformations in organic synthesis and radical polymerization chemistry. NHC-boranes are readily accessible and stable to air, water, base, and even mild acid. More interestingly, their reactivities are often fundamentally different from trivalent boranes and many other Lewis base complexes of boranes.¹¹⁶

One of the most striking differences between free boranes and NHC-boranes is their behaviors in hydroboration reactions of π bonds (Figure 5-1). Figure 5-1A demonstrates the traditional hydroboration of alkynes with simple boranes such as $\text{BH}_3\text{-THF}$. In this reaction, rapid exchange of the Lewis base THF with a π bond leads to an alkyne- BH_3 complex, which then undergoes a concerted C-H/C-B bond formation via a four-membered cyclic transition state to form *cis*-alkenylboranes exclusively.¹¹⁷ Unlike $\text{BH}_3\text{-THF}$, NHC-boranes do not hydroborate electron-rich alkenes and alkynes, even at high temperatures (Figure 5-1B).¹¹⁸ On the other hand, NHC-boranes can successfully hydroborate electron-deficient alkynes to yield unexpected *trans*-alkenylboranes, and even more unusual *trans*-borirane products (Figure 5-1C).¹¹⁹ Furthermore, NHC-boranes spontaneously react with a diverse range of arynes generated in situ to yield the hydroboration products (Figure 5-1D),¹²⁰ while free boranes are incompatible with the reagents and conditions to generate benzyne due to their greater reactivity.¹²¹ Additionally, the

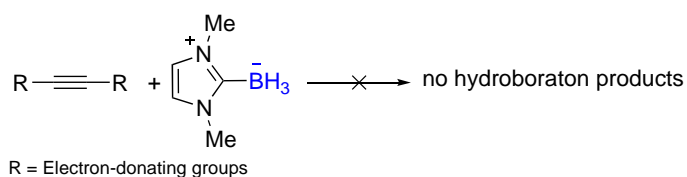
hydroboration of substituted alkynes with NHC-boranes are regioselective. In particular, for alkynes bearing an electron-withdrawing group at C-3 position, unusual *ortho* regioisomers are formed.

(Figure 5-1E)

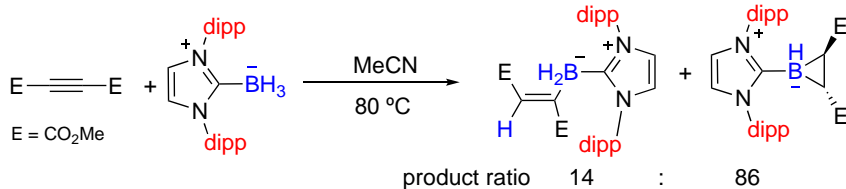
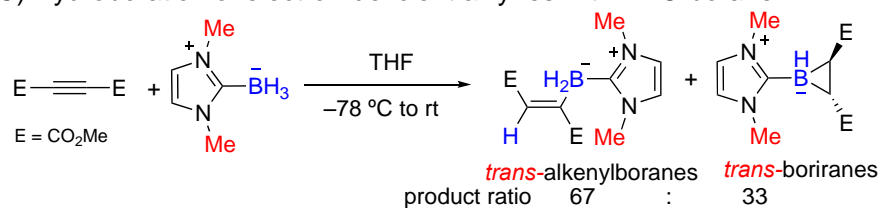
(A) Hydroboration of alkynes with BH_3 -THF



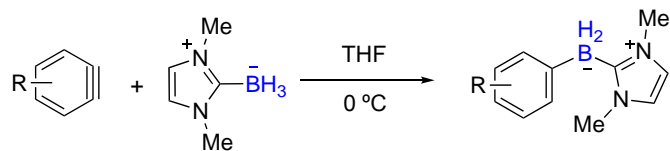
(B) Hydroboration of electron-rich alkynes with NHC-borane



(C) Hydroboration of electron-deficient alkynes with NHC-borane



(D) Hydroboration of alkynes with NHC-borane



(E) Regioselectivities in hydroboration of 3-methoxy-benzynes with NHC-borane

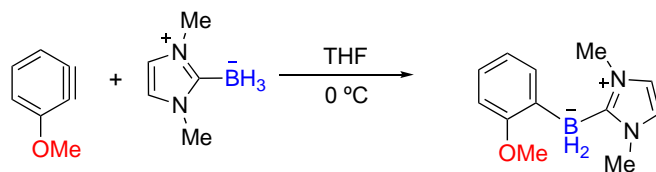


Figure 5-1 Hydroboration of alkynes and alkynes with boranes and NHC-boranes

In this Chapter, we performed a detailed mechanistic study on the hydroboration of alkynes and arynes with NHC-boranes to investigate the reactivity, and the origin of chemo- and regioselectivity. Our computational study will elucidate the following questions: 1) what are the mechanisms of the hydroboration of electron-deficient alkynes with NHC-boranes? How to form the unusual *trans*-boriranes? is the hydroboration with NHC-borane a concerted process like the BH₃ hydroboration? 2) what is the origin of product *trans*-selectivity in the alkyne hydroboration? 3) what is the origin of product regioselectivity in the substituted aryne hydroboration? 4) what are the factors that controls the reactivity difference between alkynes and arynes in hydroboration with NHC-boranes?

5.2 Computational Methods

All DFT calculations were performed using the Gaussian 09 software package.⁵⁴ The M06-2X¹¹ density functional and the 6-31G(d)¹³ basis set were used in geometry optimizations. The weakly bound zwitterionic intermediate **3** cannot be located using M06-2X. Thus, its geometry was optimized with the B3LYP⁸ density functional and 6-31G(d) basis set instead. Single-point energies were calculated with M06-2X and the 6-311++G(d,p) basis set. The SMD²¹ solvation model and the THF solvent were used in the geometry optimizations and single-point energy calculations.

Quasi-classical Born-Oppenheimer molecular dynamics (BOMD) trajectory simulations^{28,29} were performed using Gaussian 09. The initial geometries and velocities of the BOMD trajectories were generated from the normal mode sampling of the investigated transition state at 298 K. A total of 100 trajectories were generated and were propagated using the classical

equations of motion with energies and forces computed using M06-2X/6-31G(d) in THF with the SMD solvation model. An initial kinetic energy of 0.6 kcal/mol was added along the transition vector. Starting from the transition state, the trajectory propagation was performed in both directions to form the reactant and the product. A time step of about 0.8 fs was used in the trajectory propagation. The Hessian was updated every 12 steps. In alkyne hydroboration, the trajectories stop either when the NHC borenium and the alkenyl anion are away at least 3.2 Å (i.e. two separate species), or the B-C1 bond is longer than 2.2 Å & B-C2 bond is shorter than 1.6 Å (i.e. the formation of alkenylboranes), or the B-C1 bond is shorter than 1.7 Å & H-C2 bond is shorter than 1.2 Å (i.e. the formation of borirane). In benzyne hydroboration, the trajectories stop either the benzyne and NHC-boranes is away at least 2.9 Å (i.e. two separate species), or the transferred H-C1 bond is shorter than 1.09 Å & the B-C2 bond is shorter than 1.625 Å (i.e. the formation of hydroboration product).

5.3 Results and Discussions

5.3.1 Bifurcation Trajectory of Acetylenedicarboxylate Hydroboration with NHC-Borane

In our calculations, the hydroboration of acetylenedicarboxylate (**2**) with diMe-substituted NHC-borane (**1**) was investigated (Figure 5-2). Experimentally, the *trans*-alkenylboranes (**5**) and *trans*-borirane (**6**) are both primary reaction products with a ratio of 67:33.

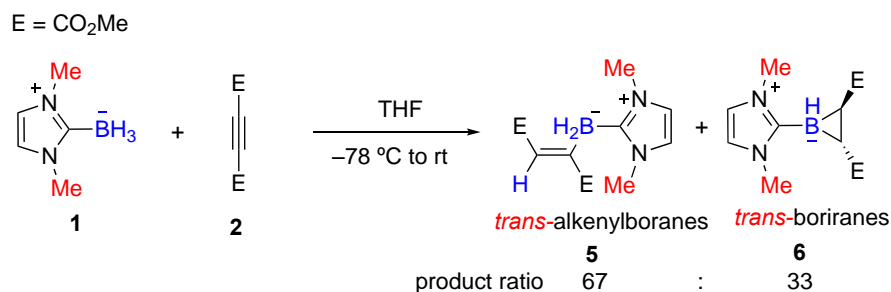


Figure 5-2 Hydroboration of acetylenedicarboxylate with Me-substituted NHC-borane

Thus, we performed DFT calculations to investigate pathways for their formation. The DFT calculations were performed at the M06-2X/6-311++G(d,p)//M06-2X/6-31G(d) level of theory and the SMD solvation model in THF. The most favorable pathways in the reaction of NHC borane **5** and **6** are shown in Figure 5-3. All energies are in kcal/mol with respect to **1** and **2**.

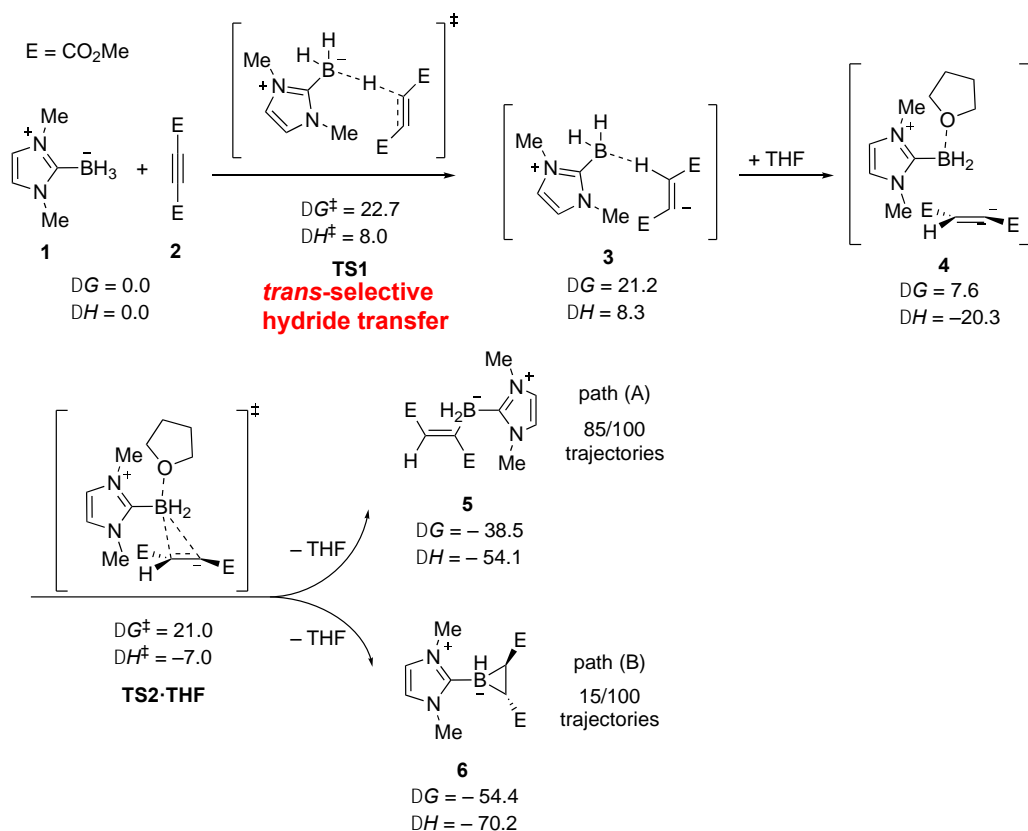


Figure 5-3 Favorable mechanism of the formation of alkenylborane and borirane.

Since NHC-boranes are good hydride donors,¹²² we hypothesized that they might hydroborate electron poor alkynes like acetylenedicarboxylates via a hydride transfer pathway. Based on our DFT calculations, the initial hydride transfer from NHC-borane **1** to **2** is highly *trans*-selective (**TS1**) to form a weakly bound zwitterionic complex of the NHC borenium and the alkenyl anion **3**. The corresponding *cis*-selective hydride transfer (**TS1'**) requires 5.0 kcal/mol higher activation free energy (See details in Section 5.3.2).

Upon coordination with a THF solvent molecule, the borenium is converted to a more stable four-coordinated boronium cation, which forms an ion pair with the alkenyl anion **4**. Subsequent addition of the THF-coordinated borenium to the alkenyl anion occurs via **TS2•THF**, in which the boronium approaches the π orbital that is perpendicular to the plane of the alkenyl anion. Although this geometry resembles the classical four-membered alkene hydroboration transition state,¹²³ the B-H bond in **TS2•THF** is short (1.19 Å, see Figure 5-5), suggesting this TS may not directly lead to B-H bond cleavage.

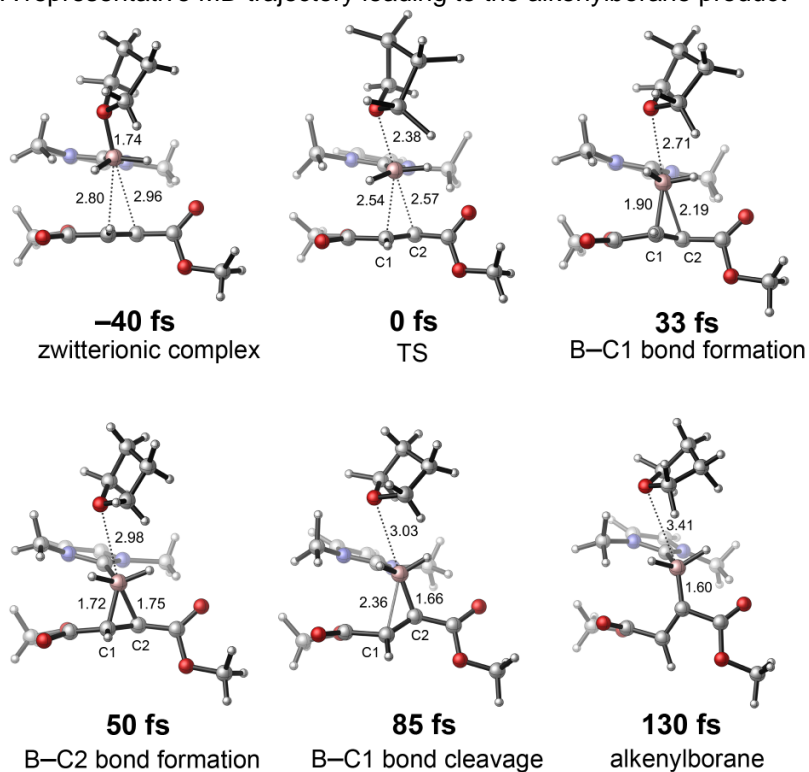
To identify the product formed from the borenium addition transition state **TS2•THF**, we performed quasi-classical Born-Oppenheimer molecular dynamics (BOMD) trajectory simulations. The initial geometries and velocities for the BOMD trajectories were generated from the normal mode sampling of **TS2•THF** at 298 K. 100 trajectories were propagated using the classical equations of motion with energies and forces computed using M06-2X/6-31G(d) in THF with the SMD solvation model. Each trajectory consisted a forward and reverse segment along the vibration of the transition state.

Out of the 100 trajectories calculated, the alkenylborane product **5** is formed in 85, and the borirane product **6** is formed in 15. These results are roughly consistent with experiment (67:33 in Figure 5-2) and indicate that a single transition state **TS2•THF** leads to both the alkenylborane

and the borirane products via a bifurcating reaction pathway in which no stable intermediates or transition states exist between the TS and the two final products.¹²⁴

Snapshots of two representative BOMD trajectories that lead to the alkenylborane and the borirane products are shown in Figure 5-4A and 5-4B, respectively. Both trajectories start by shortening of the B-C1 bond, followed by the decrease of the B-C2 bond distance. Then the two trajectories diverge. In the trajectory leading to the alkenylborane product (Figure 5-4A), the B-C1 bond is cleaved after 85 fs. In contrast, a 1,2-hydrogen migration occurred in the trajectory shown in Figure 5-4B, which leads to the formation of the C-H bond in the borirane product.

(A) A representative MD trajectory leading to the alkenylborane product



(B) A representative MD trajectory leading to the borirane product

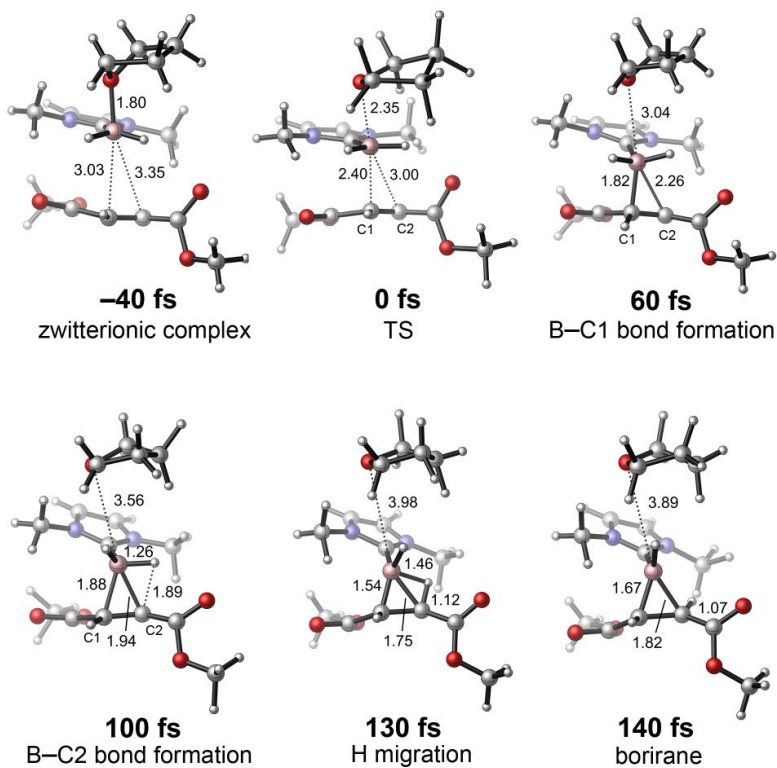


Figure 5-4 Snapshots of BOMD trajectory simulations of the reaction of 1 and 2

In addition, we surmised that the NHC borenium generated from the hydride transfer may directly react with the alkenyl anion without coordination with the explicit THF molecule. The reaction of NHC borenium with alkenyl anion is highly exergonic and likely occurs without a barrier (no stable transition state can be located in geometry optimization; a scan of the reaction coordinate indicates no barrier for the formation of either borirane or alkenylborane from NHC borenium and alkenyl anion). To investigate if the reaction of NHC borenium and alkenyl anion also bifurcates to borirane and alkenylborane, we performed BOMD simulation of the addition of NHC borenium to the alkenyl anion in the absence of THF molecule. Since no stable transition state of this process can be located in geometry optimization, the initial geometry of the BOMD simulation, **TS2-*pseudo***, was obtained by removing the THF molecule from the optimized geometry of **TS2•THF** followed by a restricted optimization with fixed B-C1 and B-C2 bond lengths using M06-2X/6-31G(d) in THF with the SMD solvation model (Figure 5-5).

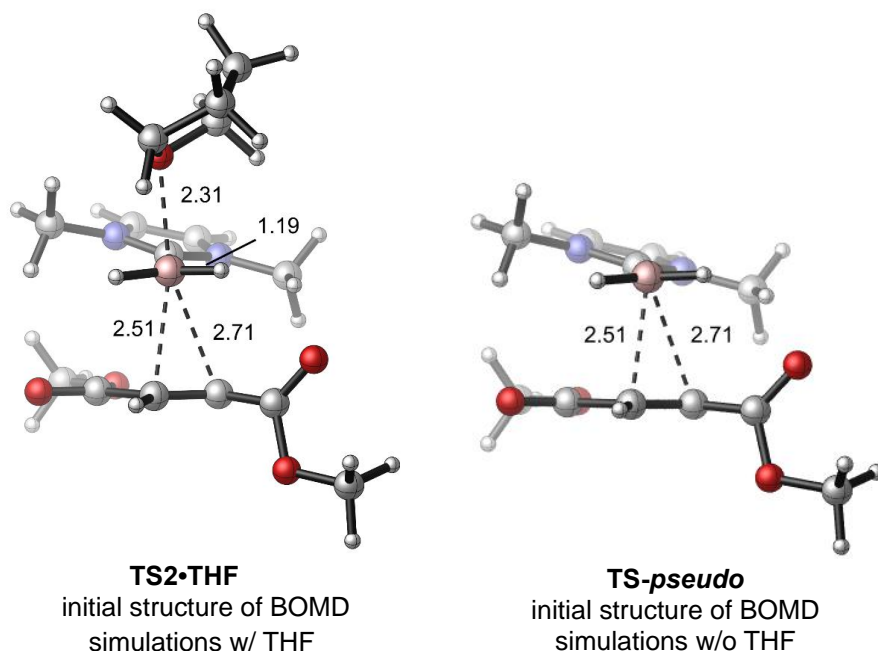


Figure 5-5 Structures used in the normal model sampling to generate initial geometries for the BOMD trajectory simulations.

Similarly, the initial geometries and velocities of 100 BOMD trajectories were generated from the normal mode sampling of **TS2-*pseudo*** at 298 K. The trajectories were then propagated using the same approach as described above. As shown in Figure 5-6, out of the 100 trajectories simulated, the alkenylborane product **5** was formed in 83 trajectories, and the borirane product **6** was formed in 17 trajectories. The computed product ratio was quite similar to that obtained from the BOMD simulations from **TS2•THF**. These results indicate the NHC borenium react with the alkenyl anion to form the borirane and alkenylborane products in a bifurcating pathway regardless whether an explicit THF molecule coordinates to the NHC borenium.

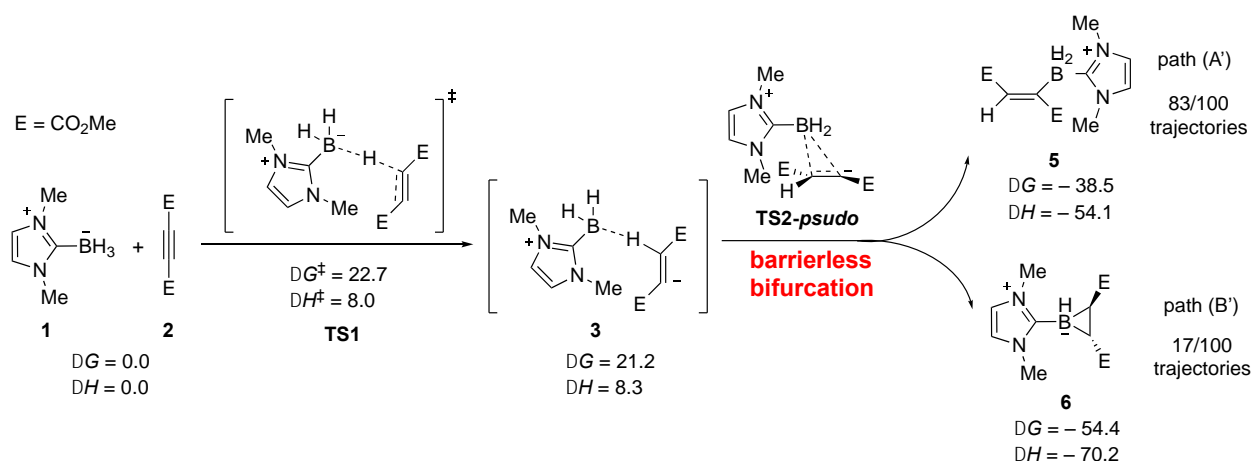


Figure 5-6 Mechanism of formation of alkenylborane and borirane without explicit THF molecule

5.3.2 Formation of *cis*-alkenylborane and borirane and the origin of *trans*-selectivity

As shown in Figure 5-3 and Figure 5-6, the rate-determining step of alkyne hydroboration is the hydride transfer step. We hypothesized that the hydride transfer step also determines the chemo-selectivity. Thus, the *cis*-selective hydride transfer pathway was also calculated for comparison (Figure 5-7). It was found that the *cis*-selective hydride transfer (**TS1'**) requires a 5.0 kcal/mol higher activation free energy than the *trans*-selective hydride transfer (**TS1**). This agrees

with the experimentally observed *trans*-selectivity for both borirane and alkenylborane products. The lower energy of **TS1** can be attributed to the stabilizing electrostatic interaction between the positively charged NHC moiety on the NHC borane and the adjacent carboxyl group on the alkyne (Figure 5-8).

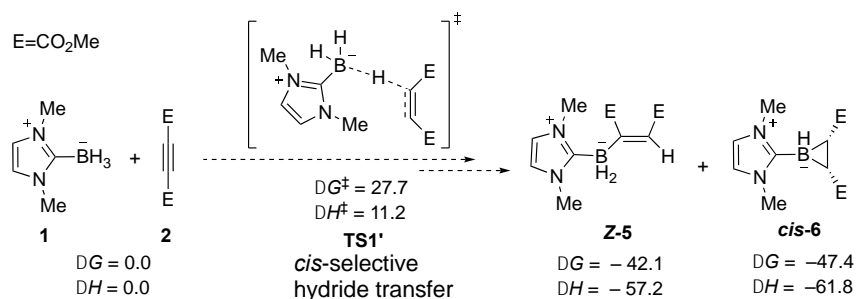


Figure 5-7 Mechanism of *cis*-selective hydride transfer

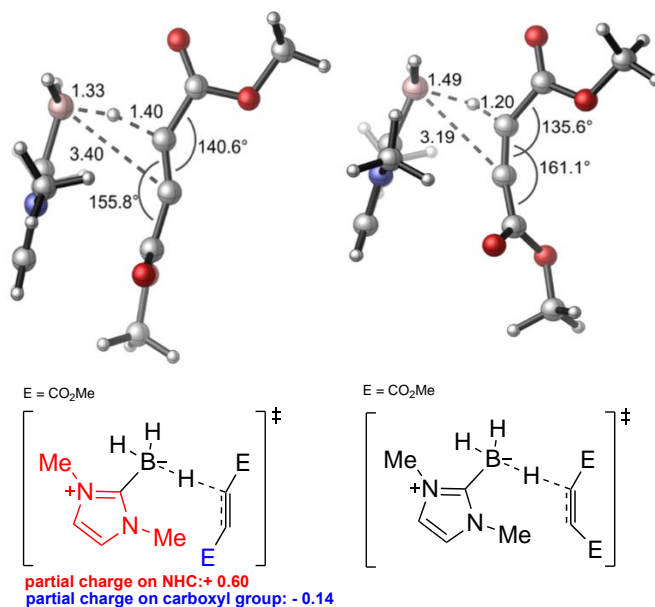


Figure 5-8 Optimized geometries of *trans*- and *cis*-selective hydride transfer transition states

5.3.3 Other mechanisms in acetylenedicarboxylate hydroboration

In addition to the most favorable bifurcation pathway shown in Figure 5-3, other possible mechanisms of the formation of borirane and alkenylborane were also computed with DFT.

1. Proton transfer/borylene cycloaddition pathway

In the alternative pathway shown in Figure 5-9, after the initial *trans*-selective hydride transfer to form the zwitterionic complex **3**, the proton transfer from the NHC borenium to the alkenyl anion yields borylene **7** and alkene **8**. The subsequent borylene cycloaddition to the alkene affords the borirane product. DFT calculations indicate the proton transfer transition state (**TS3**, Figure 5-10) requires a high barrier of 51.7 kcal/mol with respect to the reactants **1** and **2**. Similarly, the proton transfer from the THF-coordinated NHC boronium to the alkenyl anion in ion-pair **4** was also calculated (**TS3•THF**). This process requires an activation free energy of 34.8 kcal/mol with respect to **1** and **2**. Because of the high barriers of proton transfer (**TS3** and **TS3•THF**), these pathways were ruled out.

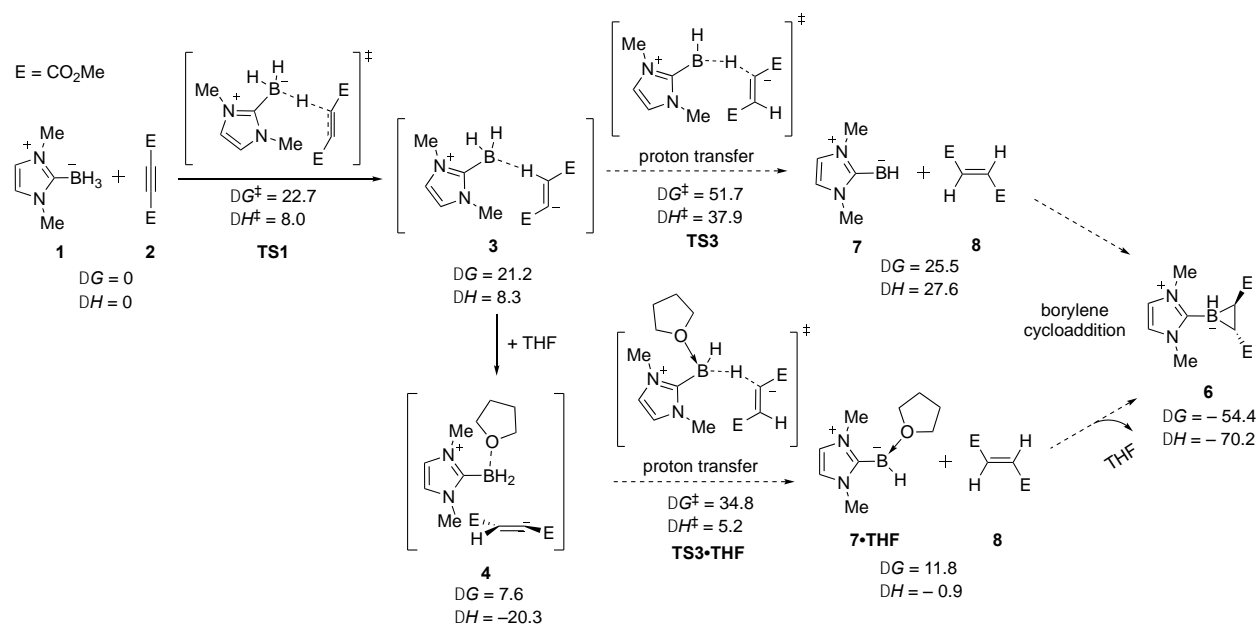


Figure 5-9 Proton transfer-borylene cycloaddition pathway of the formation of borirane

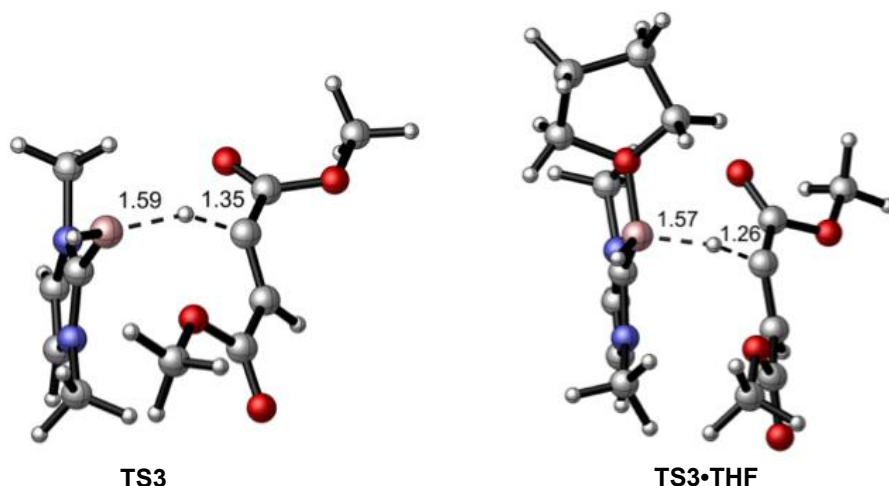


Figure 5-10 Optimized geometry of the proton transfer transition states **TS3** and **TS3•THF**

2. Interconversion between alkenylborane and borirane

To explore the possibility of interconversion between the alkenylborane **5** and borirane **6**, the 1,2-hydride transfer pathway was investigated (Figure 5-11). The 1,2-hydride transfer in **5** (via **TS4**) leads to a zwitterionic intermediate **9**, which then undergoes C–B bond forming cyclization (**TS5**) to form the borirane product **6**. The optimized geometries of **TS4**, **9**, and **TS5** are shown in Figure 5-12. Intermediate **9** is stabilized by the intermolecular coordination of boron and carbonyl group in the ester. Since both **TS4** and **TS5** require high barriers (31.9 and 41.7 kcal/mol with respect to **5** and **9**, respectively), interconversion between **5** and **6** is not expected to occur under the experimental conditions. Additionally, the interconversion between *Z*-alkenylborane *Z*-**5** and *cis*-borirane *cis*-**6** via 1,2-hydride transfer was also calculated (via transition states *cis*-**TS4**, *cis*-**TS5**, and intermediate *cis*-**9**) (Figure 5-11 and Figure 5-12). Due to the high barriers for *cis*-**TS4** and *cis*-**TS5**, this interconversion pathway for the *Z*-alkenylborane was ruled out as well. These results agree with the experiment that **5** and *Z*-**5** do not interconvert with **6** and *cis*-**6**.

E=CO₂Me

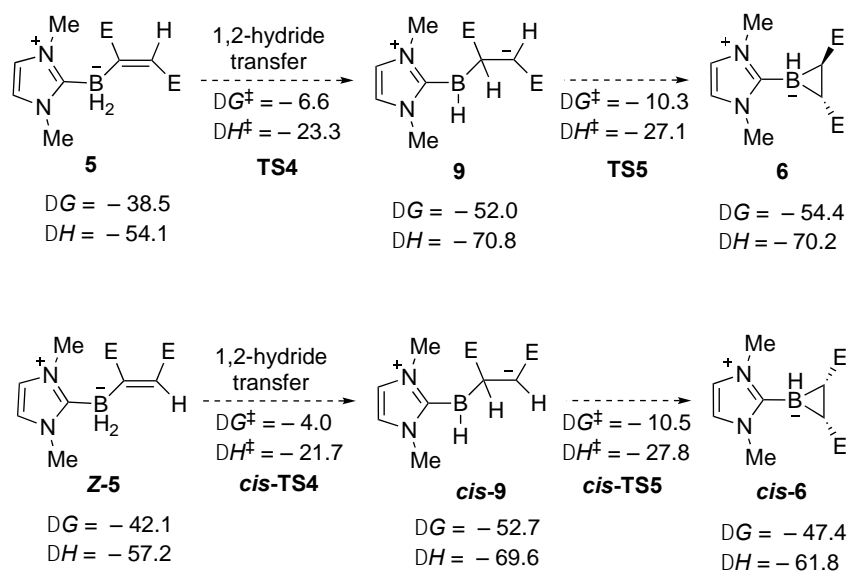


Figure 5-11 Interconversion between alkenylorane and borirane

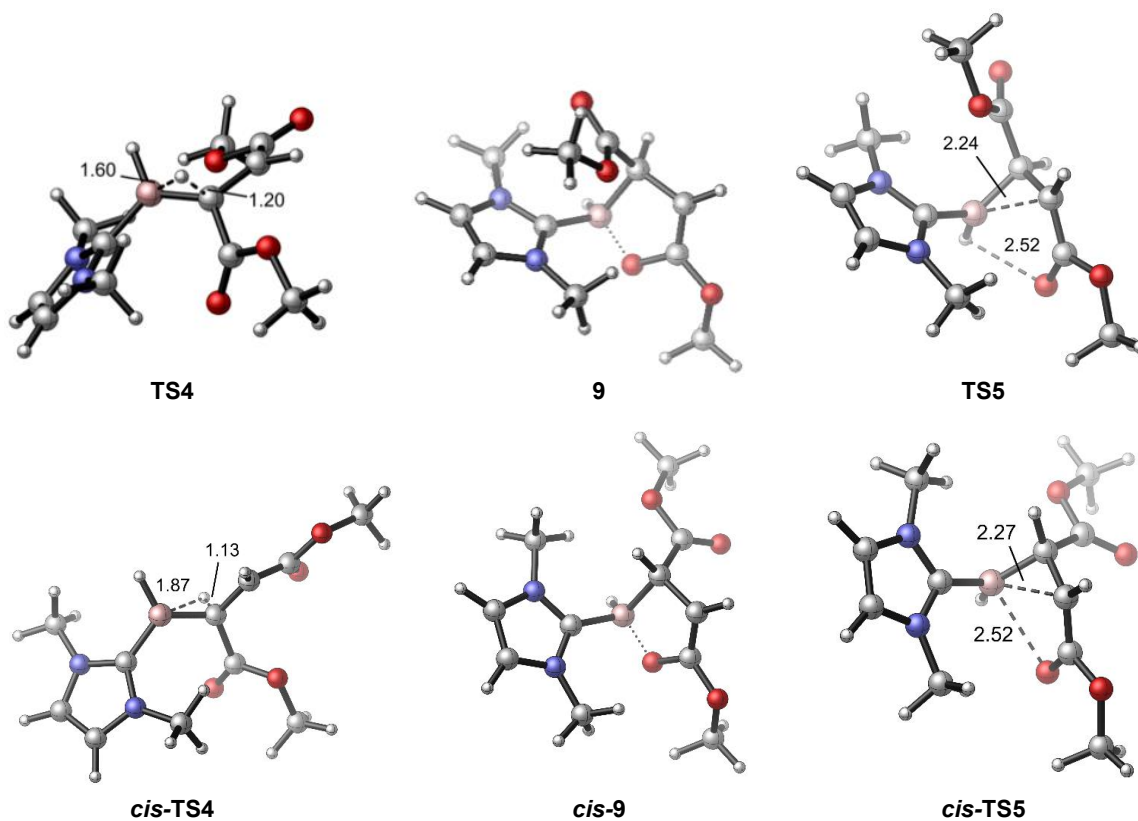


Figure 5-12 Optimized geometry of transition states and intermediates in the 1,2-hydride transfer pathway

3. *Cis/trans* isomerization of isolated alkenyl anion

Due to the very high barriers in the 1,2-hydride transfer pathways from both *cis*- and *trans*-alkenylborane (Figure 5-11), the *cis/trans* isomerization via intermediates **9** and *cis*-**9** can be ruled out. Dissociation of the THF-coordinated zwitterionic complex **4** may liberate a free *trans*-alkenyl anion **11** (eq. 5-1, Figure 5-11). Although the *trans*-to-*cis* isomerization of alkenyl anion **11** requires only a relatively low barrier of only 9.0 kcal/mol (**TS6**) and the resulting *cis*-alkenyl anion (*cis*-**11**) has very similar stability as the *trans*-alkenyl anion (eq. 5-2), such isomerization of the alkenyl anion is not likely to be able to compete with the addition of NHC-borenium or the THF-coordinated NHC-boronium (eqs. 5-3 and 5-4) to form *trans*-alkenylborane and *trans*-borirane. Calculations indicated the reaction of **11** with NHC-borenium is barrierless, while the bimolecular reaction with THF-coordinated NHC-boronium requires a barrier of 14.4 kcal/mol. It should be noted that the later barrier is likely to be overestimated due to errors in the computations of activation entropy for this bimolecular reaction.¹²⁵

E = CO₂Me

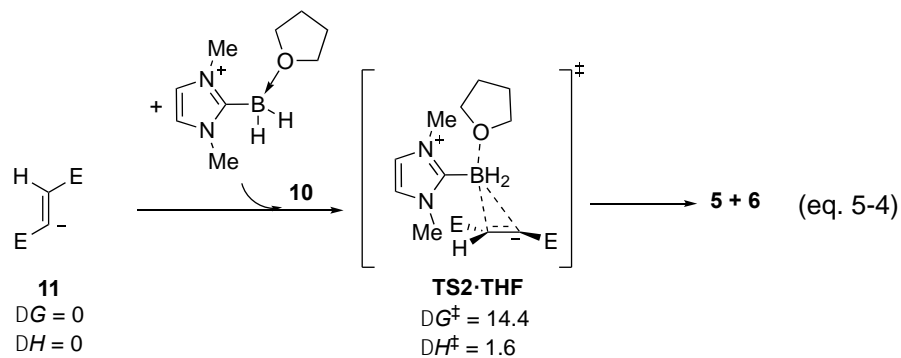
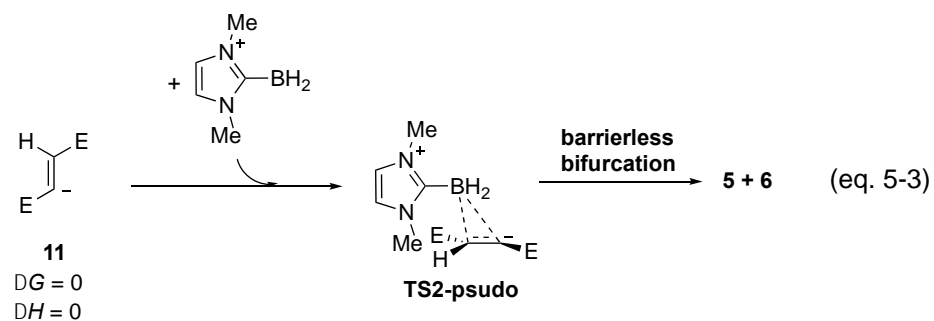
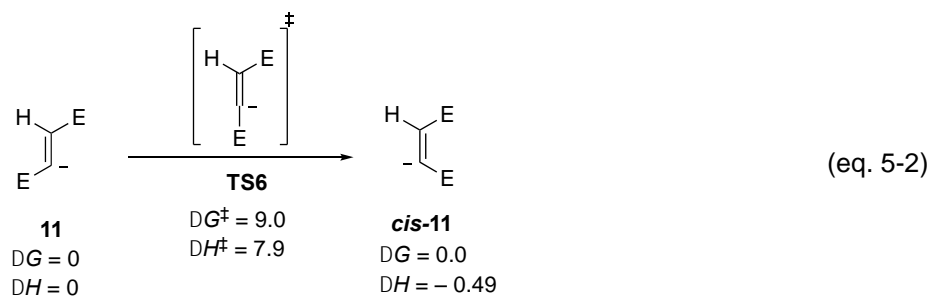
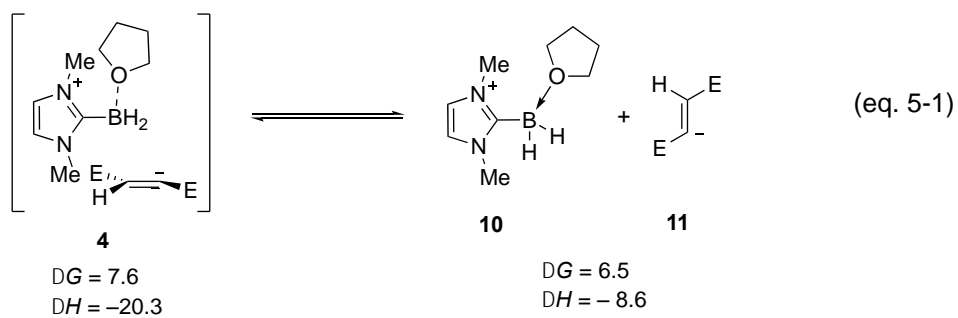


Figure 5-13 *Cis/trans* isomerization of alkenyl anion 11 is not likely to compete with boronium addition

5.3.4 Mechanisms of the hydroboration of benzyne with NHC-boranes

We first investigated the mechanism of the reaction of benzyne (**12**) with diMe-substituted NHC-borane (**1**) (Figure 5-14). Three possible mechanisms are proposed in Figure 5-15. Path A assumes that the hydroboration of benzyne with NHC-borane occurs through the formation of a synchronous concerted four-membered ring transition state like the reaction with BH_3 . But it might not be true because this synchronous concerted four-membered ring transition state leads to “*anti*-Markovnikov” products¹¹⁷ that contradicts the observed fact that *ortho* regioisomers predominate. In fact, the formation of the unusual *ortho* regioisomers for arynes bearing an electron-withdrawing group is consistent with a hydroboration mechanism in which the NHC-boranes react as a hydride donor (path B). In addition, since NHC-boranes could serve as radical hydrogen atom donors and afford NHC-boryl radicals, the hydrogen atom transfer pathway (path C) might also be possible.^{126,127}

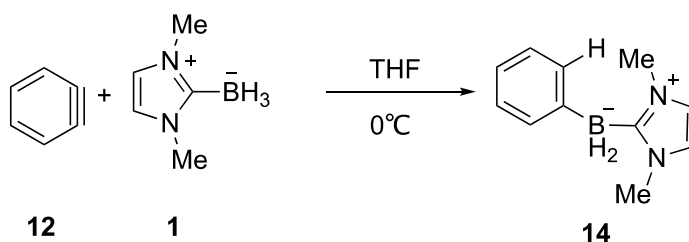


Figure 5-14 Hydroboration of benzyne with diMe-substituted NHC-borane

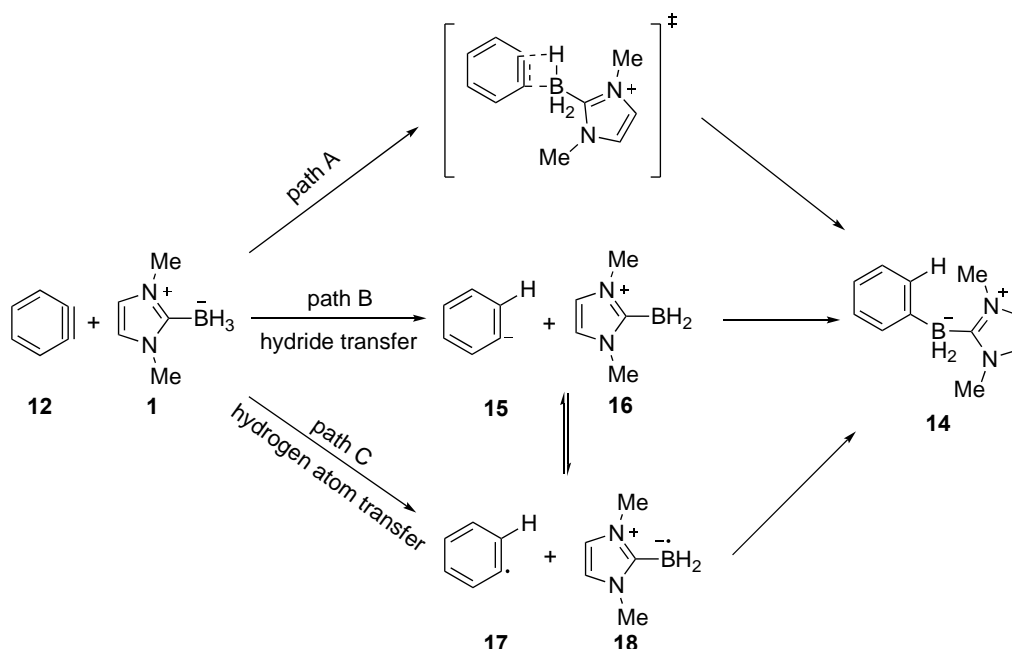


Figure 5-15 Possible mechanisms of the hydroboration of benzyne with NHC-boranes

1. Preferred hydride transfer mechanism in benzyne hydroboration

We have located the concerted hydroboration transition state **TS7-C** that directly forms the hydroboration product **14** and the stepwise hydride transfer transition state **TS7-SW** that leads to an ion pair intermediate **13**, which then undergoes rapid C-B bond formation through transition state **TS8** to form the hydroboration product (Figure 5-16). The nature of the transition states has been confirmed by intrinsic reaction coordinate (IRC) calculations. The optimized geometries of the transition states and intermediates are shown in Figure 5-17.

As shown in Figure 5-17, the concerted hydride transfer transition state (**TS7-C**) is highly asynchronous with a short forming C-H bond (1.89 Å), and a long forming C-B bond (3.58 Å). Although **TS7-C** is very early, as evidenced by the relatively short breaking B-H distance (1.25 Å), there is significant amount of electron transfer (-0.934 electrons) from the NHC borane to the benzyne in **TS7-C**. This causes noticeable distortion of the benzene geometry. The C-C-C bond

angles of the two benzyne carbons are 134.4° and 117.5° , respectively. Similarly, the stepwise hydride transfer transition state **TS7-SW** is also early with short breaking B-H distances (1.26 Å). **TS7-C** is only 0.8 kcal/mol more stable than **TS7-SW**. Also, the conversion of intermediate **3** to the final product only requires the barrier of 1.2 kcal/mol (**TS8**). Those indicates both pathways may be competing under experimental conditions. It should be noted that the discrimination between concerted and stepwise transition states (**TS7-C** vs **TS7-SW**) was determined by IRC analysis, in which there was no intermediates that could be located from **TS7-C** to the product **14**. However, from the IRC analysis of **TS7-C** (Figure 5-18), it is clear that the formation of the new C-H and C-B bonds is highly asynchronous. The hydride transfer occurs much earlier than the formation of the C-B bond. Figure 5-18 also shows the geometries of representative transient ion-pair intermediates along the IRC pathway after hydride transfer. Those transient intermediates are very close to **3**, which is obtained from IRC analysis of **TS7-SW**. In the meantime, although **TS7-SW** leads to the intermediate **3** from IRC calculation, the very small barrier between **3** to the final product would be likely overcome by the dynamic effect. Thus, to better capture the concerted or step-wise nature of the hydride transfer transition states, it is critical to measure the lifetime of those ion-pair intermediates, i.e. the time gap between C-H bond formation and C-B bond formation starting from the hydride transfer transition states. Thus, the molecular dynamics simulation is performed to distinguish the time-resolved nature of the hydride transfer mechanism. Details are shown in Section 5.3.5.

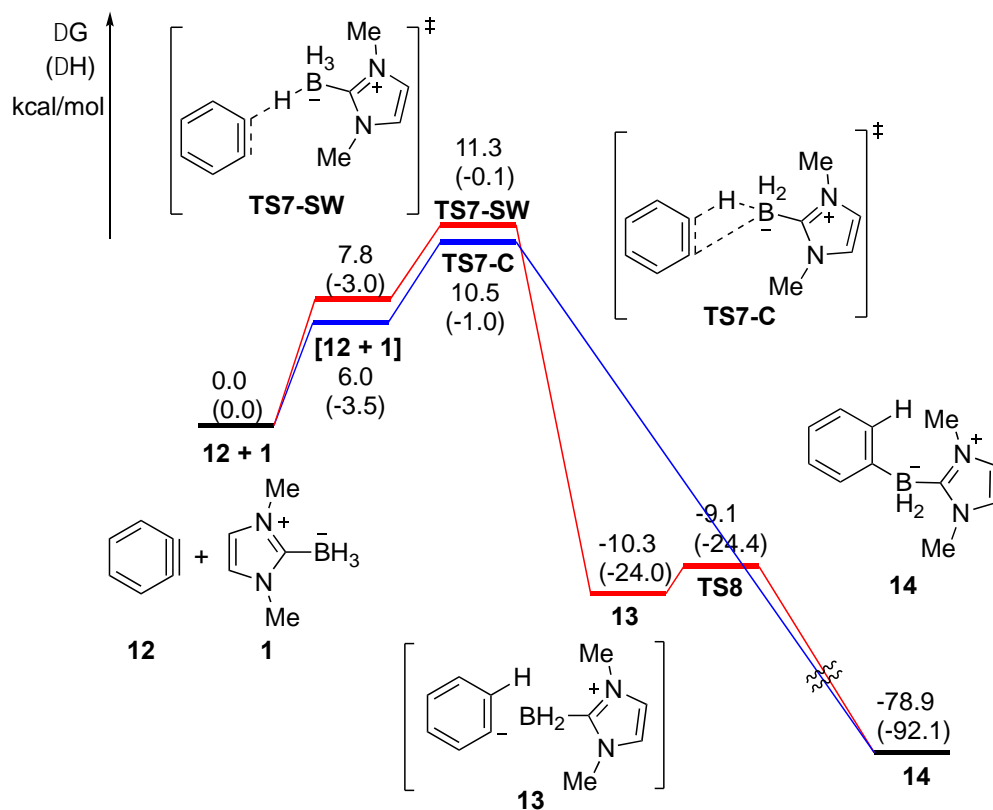


Figure 5-16 Calculated energy profile for hydride transfer mechanisms in benzyne hydroboration

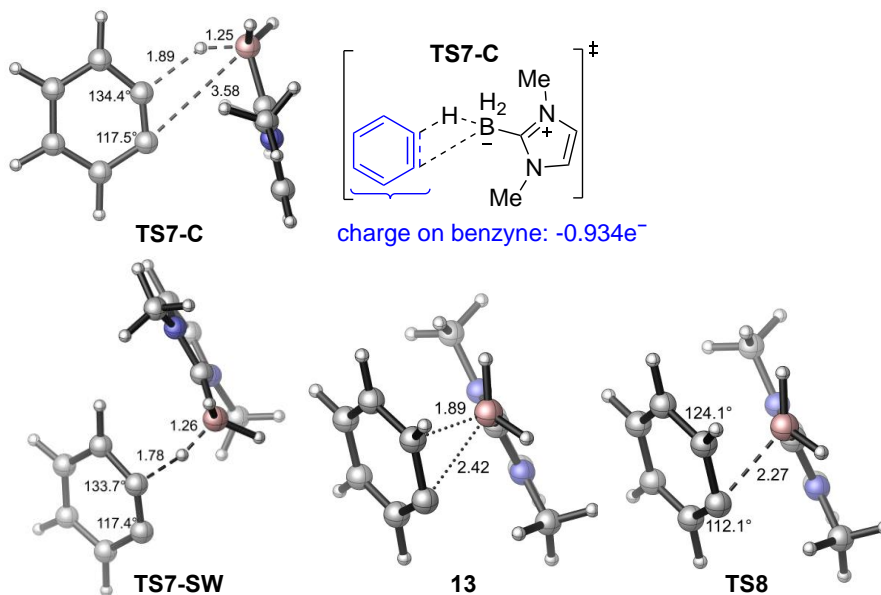


Figure 5-17 Optimized geometries of transition states and intermediates involved in hydride transfer mechanism of the benzyne hydroboration

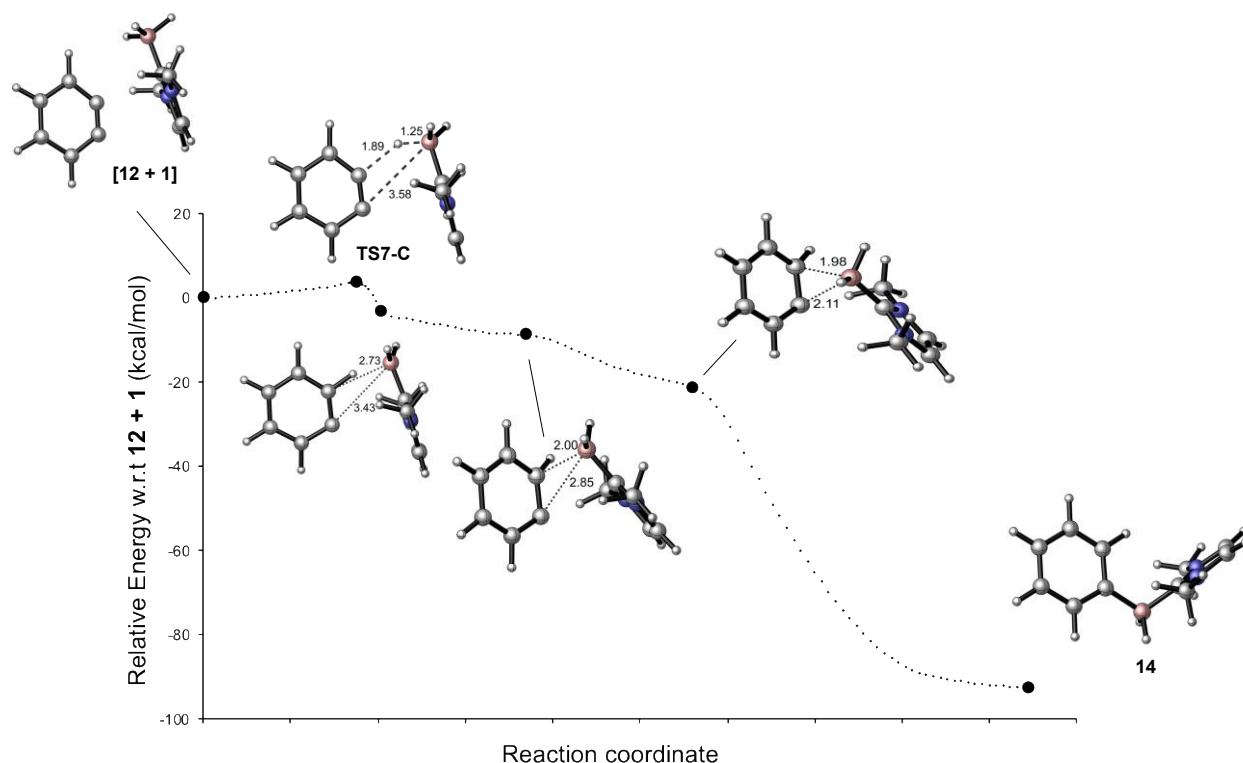
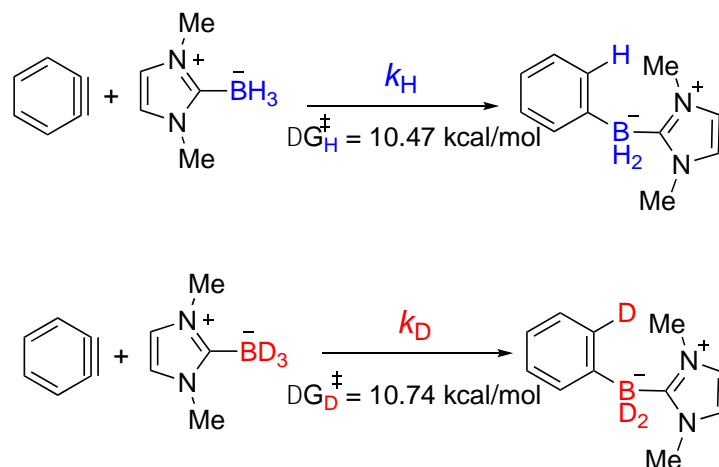


Figure 5-18 Intrinsic reaction coordinate (IRC) plot for the concerted transition states of benzyne hydroboration

2. Theoretical study on the kinetic isotope effect (KIE) in the benzyne hydroboration

The kinetic isotope effects (KIE) in the reaction of NHC-borane and benzyne was determined by experiment and computed by calculations (Figure 5-19). The computed KIE (1.22) was in good agreement with the experimental value (1.20), providing further support to the proposed hydride transfer mechanism. The relative small primary KIE for the B-H bond cleavage is due to the very early transition state.



$$KIE = \frac{k_H}{k_D} = e^{-\frac{\Delta G_H^\ddagger - \Delta G_D^\ddagger}{1.3642}} = 1.22 \text{ (Theoretically)}$$

Figure 5-19 Theoretical calculation of KIE for benzyne hydroboration with NHC-borane

3. Dissociation of ion-pair intermediate **13**

Regarding the stepwise mechanism, the dissociation of the ion-pair intermediate **13** is also considered in our calculation. As shown in Figure 5-20, the ion pair intermediate can either dissociate to two separate radicals (path 1) or to form a phenyl anion and an NHC borenium cation (path 2). Both of the two types of separate species are thermodynamically unfavored compared to the ion-pair intermediate **13**. Also, the intermediate **13** can be attacked by a THF molecule to form a THF-coordinated NHC borenium cation via a barrier of 9.6 kcal/mol (path 3). This process was less favorable than the direct C-B bond formation from **13** (the barrier is only 1.2 kcal/mol, path 4).

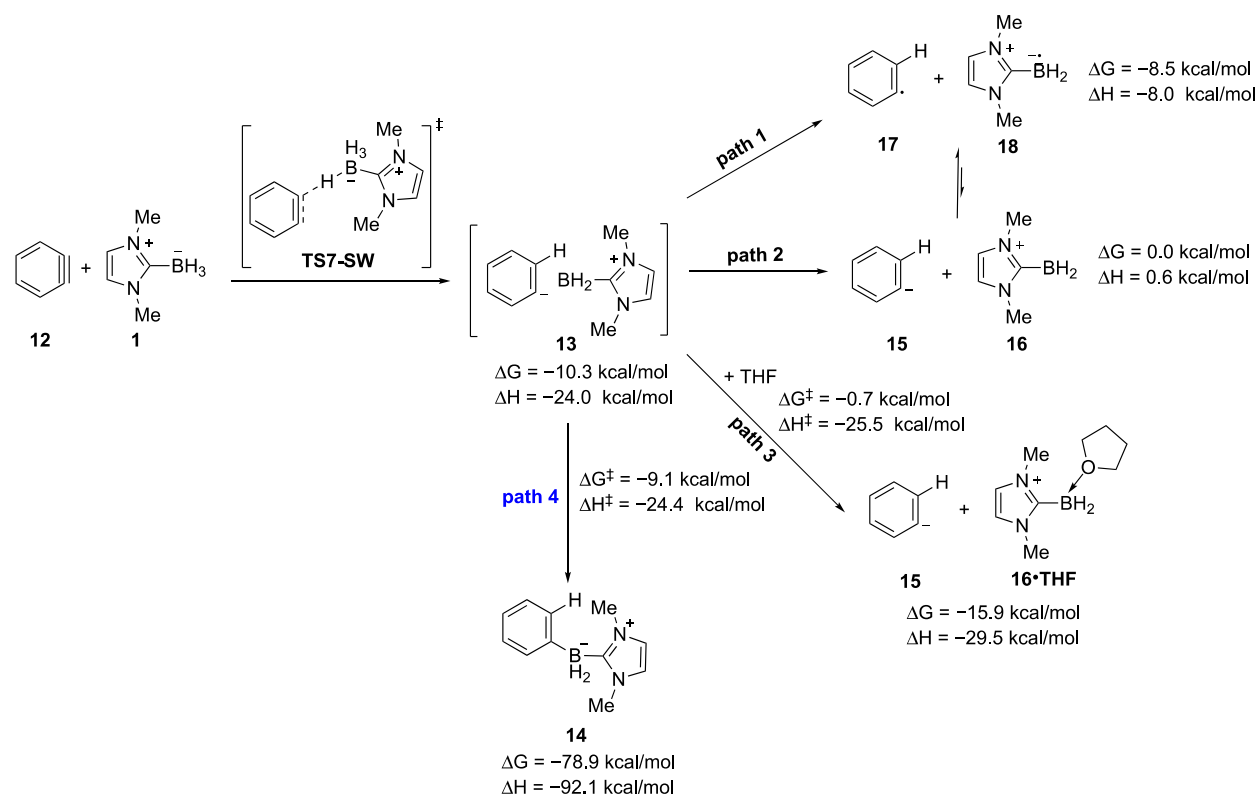


Figure S-20 Unfavored pathways that involved the dissociation of 13

4. Mechanism of hydrogen atom transfer

Other than the hydride transfer mechanism, the NHC-borane might be also likely to donate hydrogen atom to the benzyne to form two radical species **17** and **18** (path C in Figure 5-15). However, we were unable to locate the open-shell singlet transition state for this hydrogen atom transfer. By the contrast, the wave function for the close-shell hydride transfer transition state is already stable. In addition, we also checked the wave function stabilities for 35 complexes along the reaction coordinate of hydrogen atom transfer by fixing the breaking B-H bond (i.e. 5 bond lengths were evenly distributed from 1.2 Å to 2.0 Å) and the forming C-H bond (i.e. 7 bond lengths were evenly distributed from 1.6 Å to 2.8 Å). None of them led to a diradical species. As such, we confirmed the close-shell character of the species involved in the benzyne hydroboration with NHC-borane, and thereby rule out the hydrogen atom transfer mechanism.

5.3.5 Molecular dynamics of the hydride transfer mechanism: concerted or stepwise?

To calculate the time gap between C-H bond formation and C-B bond in the hydride transfer mechanism of benzyne hydroboration with NHC-borane, we performed quasi-classical Born-Oppenheimer molecular dynamics (BOMD) trajectory simulations for both **TS7-C** and **TS7-SW**. The initial geometries and velocities for the BOMD trajectories were generated from the normal mode sampling of **TS7-C** or **TS7-SW** at 298 K. A total of 100 trajectories were propagated using the classical equations of motion with energies and forces computed using M06-2X/6-31G(d) in THF with the SMD solvation model. Each trajectory consisted a forward and reverse segment along the vibration of the transition state. A full trajectory was retained if the forward and reverse segments connected reactants **1** and **12** with product **14**.

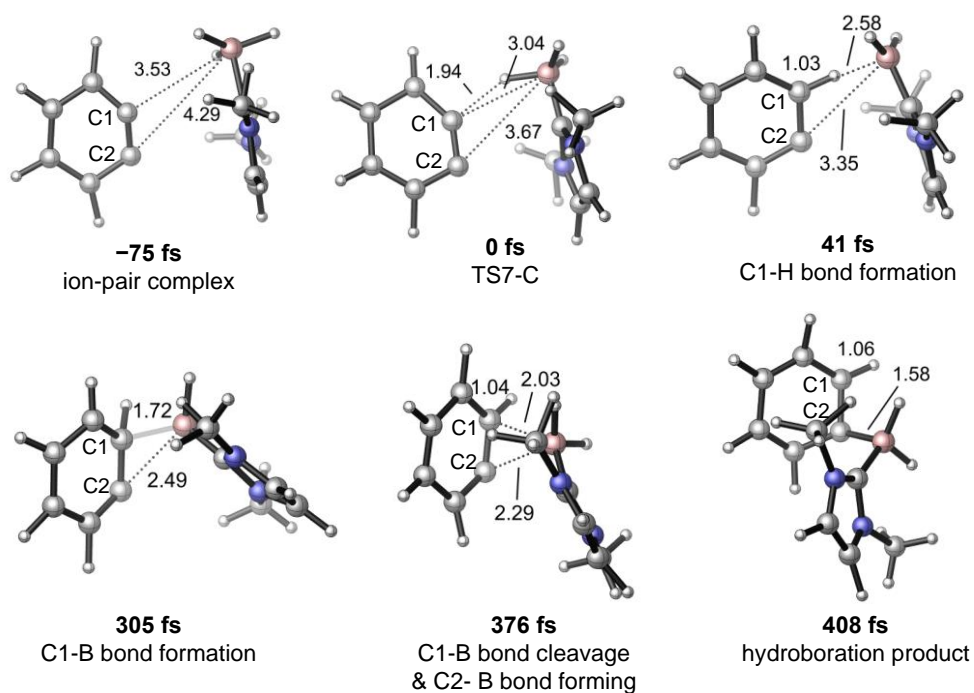
Out of the 100 trajectories calculated for **TS7-C**, there were 69 full trajectories, while 31 involved recrossings or simply unproductive trajectories. Similar to IRC calculation, all 69 productive trajectories led directly to the hydroboration product. Snapshots of a representative trajectory are shown in Figure 5-21A. The benzyne and the NHC-borane approach mutually from -75 fs to 0 fs, and reach 3.04 Å for C1-B bond, 3.67 Å for C2-B bond and 1.94 Å for C1-H bond. Here we define 1.1 Å as the distance at which the C-H bond is formed and 1.625 Å as the distance for the C-B bond formation. It is observed that the first bond (C1-H) is formed at 41 fs and the second bond (C2-B) is formed at 408 fs, leading to a 367 fs time gap between the formation of two bonds. This is much longer than the lifetime of a concerted transition state calculated from Eyring equation (60 fs at room temperature), and presents a typical dynamically-stepwise character.

Similarly, out of the 100 trajectories calculated for **TS7-SW**, there were 68 full trajectories, while 32 involved recrossings or simply unproductive trajectories. Interestingly, although in IRC calculation, there was a located intermediate **13** found after the hydride transfer from **TS7-SW** that

requires a low barrier of **TS8** to the product (Figure 5-16), all 68 productive trajectories can traverse through **TS8** barrier to form the final product. Snapshots of a representative trajectory are shown in Figure 5-21B. The benzyne and the NHC-borane approach mutually from -76 fs to 0 fs, and reach 2.97 Å for C1-B bond, 3.93 Å for C2-B bond and 1.85 Å for C1-H bond. We observed that the first bond (C1-H) is formed at 45 fs and the second bond (C2-B) is formed at 485 fs, leading to a 440 fs time gap between the formation of two bonds. This is also much longer than the lifetime of a concerted transition state, and even longer than the lifetime of **TS7-C**.

To monitor the dynamic behavior of all productive trajectories, we plotted the distribution of the timing for C1-H bond formation, and C2-B bond formation after hydride transfer transition states **TS7-C** and **TS7-SW**, respectively (Figure 5-22). For **TS7-C**, the average time for C1-H bond formation (i.e. hydride transfer) was 40.5 ± 14.7 fs, and the average time for the second bond (i.e. C2-B bond) formation was 419.8 ± 171.8 fs. For **TS7-SW**, the hydride transfer step takes similar time (41.6 ± 17.3 fs) to the **TS7-C**, but the second step of C2-B bond formation is slightly longer (435.7 ± 162.4 fs).

(A) A representative MD trajectory of **TS7-C**



(B) A representative MD trajectory of **TS7-SW**

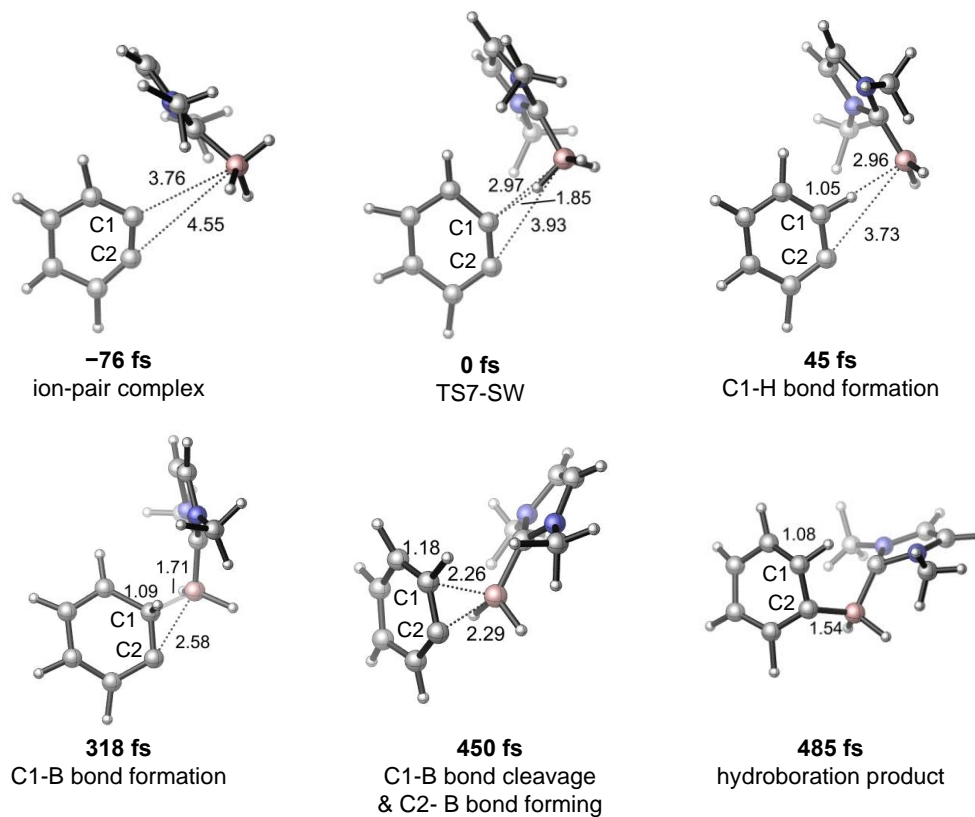
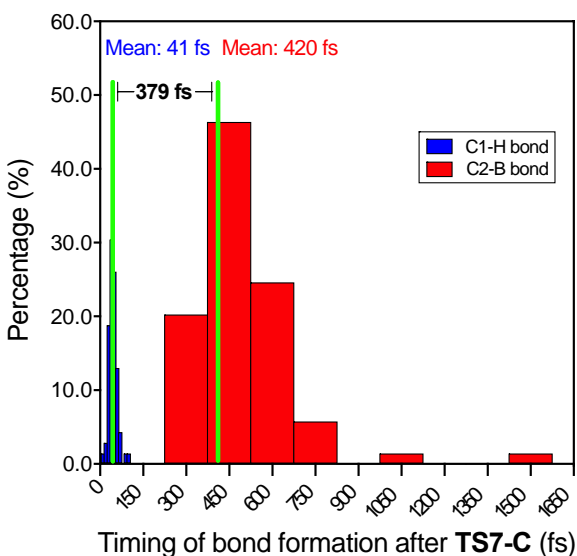


Figure 5-21 Two representative trajectories from BOMD simulation for TS7-C and TS7-SW

A. Timing of C1-H bond C2-B bond formation for **TS7-C**



B. Timing of C1-H bond C2-B bond formation for **TS7-SW**

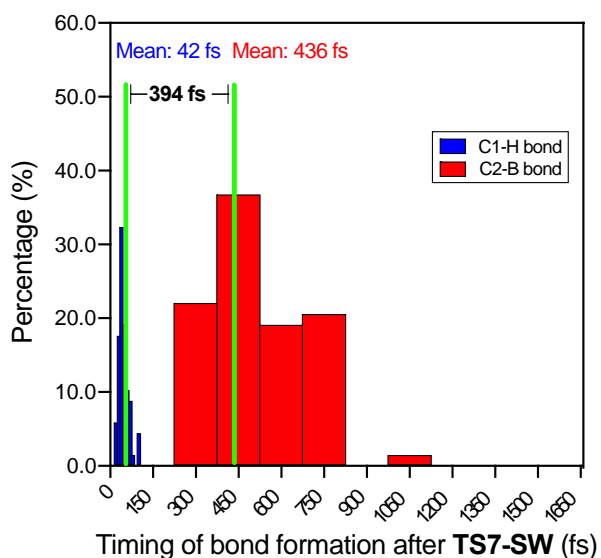
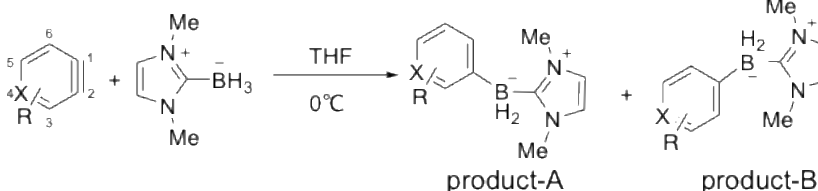


Figure 5-22 The distribution of bond formation timing for trajectories propagated from TS7-C and TS7-SW

5.3.6 Regioselectivity for substituted aryne hydroboration with NHC-boranes

Apart from unsubstituted benzyne, the NHC-borane can hydroborate various arynes to generate two possible products (Figure 5-23). Product A is generated if the hydride transfer occurs at the C-1, while Product B is generated if the hydride transfer occurs at the C-2. In general, for 3-substituted arynes or pyridyne (**17**, **18**, **23**), those bearing electron-withdrawing groups (EWG) such as -OMe, -Br, yield *ortho* products exclusively. In contrast, the *meta*- products dominate for the arynes bearing electron-donating group (EDG) at C-3 position, like -Me (**19**), -TMS (**20**), but with lower selectivity. Additionally, 4-OMe substituted aryne (**21**) leads to preferred *meta*- product, while unsubstituted 3,4-pyridyne (**22**) generates more *para*- product.



Entry	X	arynes	computed $\Delta\Delta G^\ddagger$ (kcal/mol)	experimental product ratio (A:B)
1		12 , R=H	0.0	no selectivity
2		17 , R=3-OMe	6.4	only A
3		18 , R=3-Br	3.8	only A
4	X = C	19 , R=3-Me	-0.3	30:70
5		20 , R=3-TMS, 5-Me	-0.04	20:80
6		21 , R=4-OMe	0.5	65:35
7	X = N	22 , R=H	1.1	15:85
8		23 , R=3-OMe	3.2	only A

Figure 5-23 Hydrosilylation of various arynes with NHC-borane

To investigate the origin of regioselectivity, we applied DFT calculations to compute the barriers of hydride transfer leading to product-A and product-B, respectively. The difference of the barriers in those two transition states ($\Delta\Delta G^\ddagger$) is able to estimate the observed regioselectivities. As shown in Figure 5-23, for 3-EWG substituted arynes (**17,18, 23**), $\Delta\Delta G^\ddagger$ are typically larger than 3 kcal/mol, which is in agreement with observed exclusive *ortho* regioselectivities. For 3-EDG substituted arynes (**19 & 20**), the hydride slightly prefers to attack C-2 position of aryne indicated by lower activation energy, leading to major *meta*- product. Meanwhile, the low selectivity for 4-OMe substituted aryne (**21**) is consistent with the subtle difference in computed activation energies. The only inconsistency of computed c against experimental data comes from the hydroboration of unsubstituted 3,4-pyridyne (**22**). $\Delta\Delta G^\ddagger$ of +1.1 kcal/mol suggests more *meta*-product should be produced. But experimentally, the ratio of *meta*-/*para*- products is 15:85. That

could be either due to the complexity of heterocyclic chemistry of pyridine, or the difficulty in separation of two products experimentally.

Our transition state theory suggests that the regioselectivity comes from the difference in activation barriers of hydride transfer to two competing aryne carbons, which is affected largely by aryne substituents. Kouk's group has successfully developed "aryne distortion model" and "charge-controlled model" to predict the regioselectivities of aryne nucleophilic addition from the ground state optimized aryne geometry. Here we will apply both models to study the aryne hydroboration with NHC-borane where the hydride acts as a nucleophile. Figure 5-24 shows the geometries of the transition states and the ground state aryne for **17** and **19**. In the case of **17**, **TS-9A** is favored over **TS-9B** by 6.4 kcal/mol, which indicates that hydride prefers to attack C-1 position. The lower barrier of **TS-9A** is attributed to the less distortion from the geometry of ground state aryne (**17**) to the aryne geometry in the **TS-9A** ($\Delta E_{\text{dist}} = 1.1$ kcal/mol) than that in **TS-9B** ($\Delta E_{\text{dist}} = 4.9$ kcal/mol). Geometrically, the triple-bond internal angles ($L_{\text{C-1}}$ & $L_{\text{C-2}}$) only change 1.7° and 4° from **17** to **TS-9A**, respectively; while from **17** to **TS-9B**, the changes of $L_{\text{C-1}}$ & $L_{\text{C-2}}$ are more significant: 13.6° and 11.2° , respectively. In addition to the analysis of transition state, we investigated the geometry and NPA charge of the triple bond in the ground state **17**. It is observed that with 3-OMe substituted, the C-1 carries more positive charges (+0.136), and more pre-distorted to linear than C-2, which allows to process greater p character in the in-plane π orbital. Those two characters may explain the preference of the site of attack at C-1 in **17**. Similarly, we applied transition state theory and the analysis of pre-distorted angles and charges to 3-Me benzyne (**19**). **TS-10B** is only 0.6 kcal/mol lower than **TS-10A**, leading to low observed regioselectivity (*ortho*-product: *meta*-product = 30:70). Meanwhile, the low regioselectivity for the

hydroboration of **19** can also be predicted by the subtle differences in pre-distorted angles and charges for C-1 and C-2.

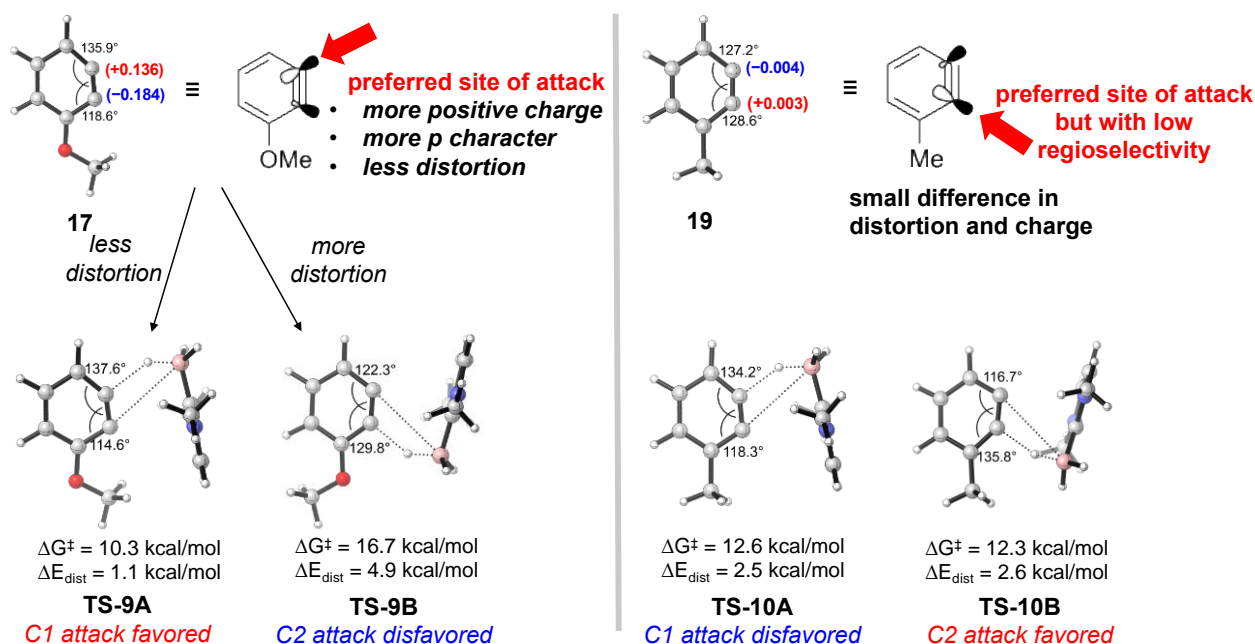


Figure 5-24 Competing transition states for hydroboration of 3-OMe benzyne (**17**) and 3-Me benzyne (**19**)

In the above two cases, we found that the difference in pre-distorted angles and charges of triple-bond in ground state arynes might be a good indicator for experimental regioselectivity. Thus, we calculated the pre-distorted angles (L_{C-1} , L_{C-2}) and charges (Q_{C-1} , Q_{C-2}) for all 8 arynes shown in Figure 5-23, and plotted the correlation between the calculated activation barriers difference ($\Delta\Delta G^\ddagger$) and the difference in pre-distorted angles (ΔL) and charges (ΔQ) (Table 5-1 and Figure 5-25). Good correlation between the calculated regioselectivities and the nature of ground state aryne validates that the hydride is prone to attack more positive, and more linear triple bond carbon. Notably, for pyridine (**7**) which regioselectivity is not correctly predicted by the difference in calculated activation energy, the calculated charges and pre-distorted angles also suggests the

opposite trend to the experimental observation. This implies that the hydroboration of pyridyne might follow different mechanism other than hydride transfer.

Table 5-1 Calculated pre-distorted angles and charges for C-1 and C-2 in arynes*

Entry	arynes	L_{C-1}	L_{C-2}	Q_{C-1}	Q_{C-2}	ΔL	ΔQ	computed $\Delta\Delta G^\ddagger$ (kcal/mol)	experimental product ratio (A:B)
1	12	127.4	127.4	-0.003	-0.003	0	0	0.0	no selectivity
2	17	135.9	118.6	0.136	-0.184	-17.3	-0.320	6.4	only A
3	18	134.3	119.6	0.131	-0.082	-14.7	-0.213	3.8	only A
4	19	127.2	128.6	-0.004	0.003	1.4	0.007	-0.3	30:70
5	20	121.0	134.8	-0.091	0.091	13.8	0.182	-0.04	20:80
6	21	126.2	128.8	-0.031	0.025	2.6	0.056	0.5	65:35
7	22	128.4	122.4	0.063	-0.075	-6	-0.138	1.1	15:85
8	23	132.8	117.4	0.143	-0.200	-15.4	-0.343	3.2	only A

* $\Delta\Delta G^\ddagger = \Delta\Delta G^\ddagger_{C-2} - \Delta\Delta G^\ddagger_{C-1}$; $\Delta L = L_{C-2} - L_{C-1}$; $\Delta Q = Q_{C-2} - Q_{C-1}$

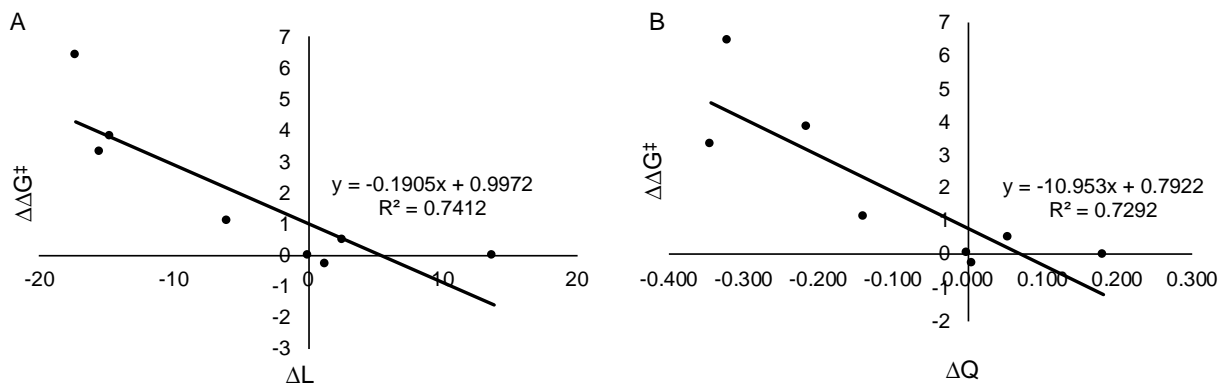


Figure 5-25 The correlation of the difference in activation barriers ($\Delta\Delta G^\ddagger$) with the difference in pre-distorted angles (ΔL) and charges (ΔQ) of ground state arynes

5.3.7 Reactivity difference between alkynes and arynes

To elaborate the reactivity difference between electron-deficient and electron-rich alkynes, and arynes in hydroboration with NHC-borane, we computed the transition states for hydroboration of acetylenedicarboxylate (**2**), 2-butyne (**24**), and benzyne (**12**) in the reaction with NHC-borane (**1**), respectively (Figure 5-26).

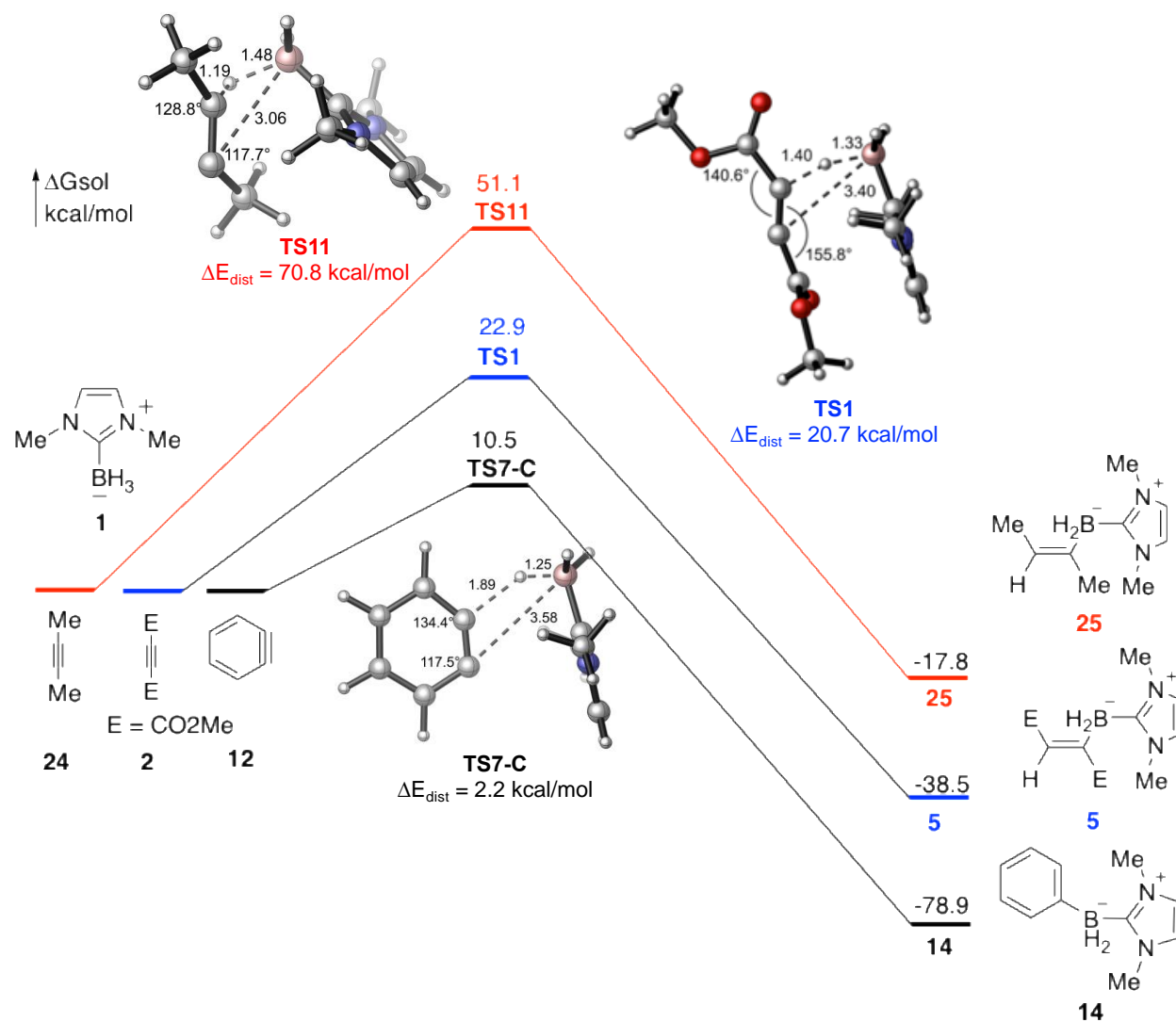


Figure 5-26 Calculated energy profiles for the hydroboration of benzyne, acetylenedicarboxylate, and 2-butyne with NHC-borane

We can see that benzyne is the most reactive with only 10.5 kcal/mol barrier, which is not likely due to an electronic effect given the NPA charge on triple-bond carbons is almost neutral (see Entry 1 in Table 5-1). The high reactivity of benzyne is likely attributed to the less distortion energy (2.2 kcal/mol) of benzyne compared to linear alkynes. The high barrier of 2-butyne hydroboration (55.1 kcal/mol) agrees with the fact that 2-butyne doesn't react with NHC-borane experimentally. The very late hydride transfer transition state (**TS11**), which has short C1-H

distance of 1.19Å, causes the huge distortion penalty. Regarding the electron-deficient alkyne (**TS1**), both advantageous electronic effect and less distortion penalty contributes to the higher reactivity over 2-butyne. Another interesting finding is that the trend in activation barriers of hydroboration is consistent with the trend of thermodynamic stabilities. The benzyne hydroboration product (**14**) is the most stable product compared to two alkenylborane products (**2** and **25**), which corresponds to the lowest barrier of hydride transfer.

5.4 Summary

In this Chapter, we applied DFT calculations and quasi-classical Born-Oppenheimer molecular dynamics (BOMD) simulations to study the mechanisms, dynamics, and chemo-, and regioselectivity of the hydroboration of alkynes and arynes with NHC-boranes.

Our computational studies elucidated that the hydride transfer is the predominating mechanism in the hydroboration of both alkynes and arynes with NHC-borane. The *trans*-selectivity in alkyne hydroboration is attributed to the lower barrier of *trans*-selective hydride transfer process over *cis*-hydride transfer. Also, the unusual *trans*-borirane is formed along with *trans*-alkenylborane via a bifurcation pathway governed by the dynamic behavior of the hydroboration reaction. On the other hand, the hydroboration of benzyne occurs via a highly asynchronous hydride transfer transition state. Molecular dynamics simulations validated the dynamically-stepwise nature of the transition state with very long time gap of roughly 380 fs between C1-H bond and C2-B bond formation. Furthermore, the regioselectivities of substituted arynes with NHC-boranes were investigated with “aryne distortion model” and “charge-controlled model”. Our calculations demonstrated that the hydride is prone to attack more positively charges,

more linear triple-bond carbon, and the difference between pre-distorted angles and charges on triple bond in the ground state aryne is able to predict the experimental observed regioselectivities. Finally, we investigated the origin of the reactivity difference between alkyne and arynes. The high reactivity of arynes is caused by the pre-distorted geometry of aryne which resembles the geometry in the transition state. The alkynes have larger distortion penalty than the aryne. But with the installment of electron-withdrawing groups, the electron-deficient alkynes have lower barriers for the hydride transfer transition state.

PUBLICATION LIST

1. **Mechanistically Guided Predictive Models for Ligand and Initiator Effects in Copper-Catalyzed Atom Transfer Radical Polymerization (Cu-ATRP).** C. Fang, M. Fantin, X. Pan, K. De Fiebre, M. L. Coote, K. Matyjaszewski, P. Liu. *J. Am. Chem. Soc.*, **2019** (In revision)
2. **β -Mannosylation via O-Alkylation of Anomeric Cesium Alkoxides: Mechanistic Studies and Synthesis of the Hexasaccharide Core of Complex Fucosylated N-Linked Glycans.** S. Meng, B. R. Bhetuwal, H. Nguyen, C. Fang, K. Saybolt, X. Li, P. Liu, J. Zhu. *J. Am. Chem. Soc.*, **2019** (Submitted)
3. **Sequence-Controlled Polymers Through Entropy-Driven Ring-Opening Metathesis Polymerization: Theory, Molecular Weight Control, and Monomer Design.** J. A. Nowalk, C. Fang, A. L. Short, R. M. Weiss, J. H. Swisher, P. Liu, T. Y. Meyer. *J. Am. Chem. Soc.*, **2019** (Accepted)
4. **Cis-Selective Metathesis to Enhance the Living Character of Ring-Opening Polymerization: A New Approach to Sequenced Copolymers.** A. L. Short, C. Fang, J. A. Nowalk, R. M. Weiss, P. Liu, T. Y. Meyer. *ACS Macro Lett.*, **2018**, 7, 858-862
5. **Methylene Blue Catalyzed Oxidative Cleavage of N-Carbonylated Indoles.** K. Wu, C. Fang, S. Kaur, P. Liu, and T. Wang. *Synthesis*, **2018**, 50, 2897-2907

6. **Ligand-Substrate Dispersion Facilitates the Copper-Catalyzed Hydroamination of Unactivated Olefins.** G. Lu, R.Y. Liu, Y. Yang, C. Fang, D. S. Lambrecht, S.L. Buchwald and P. Liu. *J. Am. Chem. Soc.*, **2017**, 139, 16548-16555
7. **Rhodium-Catalyzed Enantioselective Radical Addition of CX₄ Reagents to Olefins.** B. Chen, C. Fang, P. Liu and J.M. Ready. *Angew. Chem. Int. Ed.* **2017**, 56, 8780–8784 (*Highlighted in Synfacts*, **2017**, 13, 0954 & *XMOL*)
8. **Synthesis of Boriranes by Double Hydroboration Reactions of N-Heterocyclic Carbene Boranes and Dimethyl Acetylenedicarboxylate.** T. R. McFadden, C. Fang, S. J. Geib, E. Merling, P. Liu and D. P. Curran. *J. Am. Chem. Soc.*, **2017**, 135, 1726-1729.
9. **Mechanism of Photoinduced Metal-Free Atom Transfer Radical Polymerization: Experimental and Computational Studies.** X. Pan, C. Fang, M. Fantin, N. Malhotra, W. Y. So, L. A. Peteanu, A. A. Isse, A. Gennaro, P. Liu, and K. Matyjaszewski. *J. Am. Chem. Soc.*, **2016**, 138, 2411–2425. (*ESI: Highly Cited Paper*)
10. **Computational Study of Rh-Catalyzed Carboacylation of Olefins: Ligand-Promoted Rhodacycle Isomerization Enables Regioselective C–C Bond Functionalization of Benzocyclobutenones.** G. Lu, C. Fang, T. Xu, G. Dong, and P. Liu. *J. Am. Chem. Soc.*, **2015**, 137, 8274–8283.

PRESENTATION LIST (SELECTED)

1. C. Fang, K. De Fiebre, M. Fantin, X. Pan, K. Matyjaszewski, **Oral**: “Predictive Model for Catalyst Effect of Photo-Induced and Copper-Catalyzed Atom Transfer Radical Polymerization (ATRP) Reaction”. *2018 AIChE Annual Meeting*, Oct. 28-Nov. 2, **2018**, Pittsburgh, PA
2. C. Fang, K. De Fiebre, X. Pan, K. Matyjaszewski, P. Liu. **Poster**: “Computational Study of the Mechanism and Catalyst Effect in Copper-Catalyzed Atom Transfer Radical Polymerization”. *Gordon Research Conferences: Computational Chemistry*, July 22-27, **2018**, Mount Snow, Dover
3. C. Fang, K. De Fiebre, X. Pan, K. Matyjaszewski, P. Liu. **Poster**: “Computational Study of Copper-Catalyzed Atom Transfer Radical Polymerization and Catalyst Discovery via Virtual Screening”. *255th ACS National Meeting*, March 18-22, **2018**, New Orleans, LA
4. C. Fang, X. Pan, M. Fantin, A. Genaro, K. Matyjaszewski, P. Liu. **Poster**: “Computational Study of Copper-Catalyzed and Photo-induced Metal-Free Atom Transfer Radical Polymerization”. *254th ACS National Meeting*, Aug. 20-24, 2017, Washington, DC (*the ACS Outstanding Poster Award*)
5. C. Fang, T. R. McFadden, D. P. Curran, P. Liu, **Poster**: “Quasiclassical Molecular Dynamics Simulations to Study the Bifurcation Trajectory of Acetylenedicarboxylate Hydroboration with

NHC-Borane”. *PQI 2017: Quantum Solution*, April 26-28, 2017, Pittsburgh Quantum Institute
(the *PQI Poster Award*)

6. C. Fang, X. Pan, K. Matyjaszewski, and P. Liu. **Poster:** “Computational Study on the Mechanism of Photoinduced Metal-Free Atom Transfer Radical Polymerization”. *48th Midwest Theoretical Chemistry Conference*, June 9-11, 2016, UITT

7. C. Fang, P. Liu. Oral: “Computational Studies of Hydroboration Reactions with N-Heterocyclic Carbene Boranes.” *2015 Simulator's Meeting*, May 20, 2015, Carnegie Mellon University

REFERENCES

- ¹ Chen, C. *Nat. Rev. Chem.* **2018**, *2*, 6–14.
- ² Sauter, D. W.; Taoufik, M.; Boisson, C. *Polymers* **2017**, *9*, 185–198.
- ³ Sailors, H. R.; Hogan, J. P. *J. Macromol. Sci. Part A Chem.* **1981**, *15*, 1377–1402.
- ⁴ Becke, A. D. *J. Chem. Phys.* **2014**, *140*, 18A301.
- ⁵ Cohen, A. J.; Mori-Sanchez, P.; Yang, W. *Chem. Rev.* **2012**, *112*, 289–320.
- ⁶ Sperger, T.; Sanhueza, I. A.; Schoenebeck, F. *Acc. Chem. Res.* **2016**, *49*, 1311–1319.
- ⁷ Sperger, T.; Sanhueza, I. A.; Kalvet, I.; Schoenebeck, F. *Chem. Rev.* **2015**, *115*, 9532–9586.
- ⁸ (a) Becke, A. D. *J. Chem. Phys.* **1993**, *98*, 5648–5652; (b) Lee, C.; Yang, W.; Parr, R. G. *Phys. Rev. B* **1988**, *37*, 785–789; (c) Miehlich, B.; Savin, A.; Stoll, H.; Preuss, H. *Chem. Phys. Lett.* **1989**, *157*, 200–206.
- ⁹ (a) Harvey, J. N. *Annu. Rep. Prog. Chem., Sect. C: Phys. Chem.* **2006**, *102*, 203–226; (b) Schlangen, M.; Schwarz, H. *ChemCatChem* **2010**, *2*, 799–802; (c) Feng, X.; Gu, J.; Xie, Y.; King, R. B.; Schaefer, H. F. *J. Chem. Theory Comput.* **2007**, *3*, 1580–1587.

-
- ¹⁰ Schreiner, P. R.; Chernish, L. V.; Gunchenko, P. A.; Tikhonchuk, E. Y.; Hausmann, H.; Serafin, M.; Schlecht, S.; Dahl, J. E. P.; Carlson, R. M. K.; Fokin, A. A. *Nature* **2011**, *477*, 308–311.
- ¹¹ Zhao, Y.; Truhlar, D. G. *Theor. Chem. Acc.*, **2008**, *120*, 215-241.
- ¹² Chai, J.-D.; Head-Gordon, M. *Phys. Chem. Chem. Phys.* **2008**, *10*, 6615-6620.
- ¹³ Rassolov, V. A.; Ratner, M. A.; Pople, J. A.; Redfern, P. C.; Curtiss, L. A. *J. Comput. Chem.* **2001**, *22*, 976-984.
- ¹⁴ Ditchfield, R.; Hehre, W. J.; Pople, J. A., *J. Chem. Phys.* **1971**, *54*, 724-728.
- ¹⁵ Fuentealba, P.; Preuss, H.; Stoll, H.; Von Szentpály, L. *Chem. Phys. Lett.* **1982**, *89*, 418-422.
- ¹⁶ Zhao, Y.; González-García, N.; Truhlar, D. G. *J. Phys. Chem. A* **2005**, *109*, 2012–2018.
- ¹⁷ Zhao, Y.; Truhlar, D. G. *Acc. Chem. Res.* **2008**, *41*, 157–167.
- ¹⁸ Weigend, F.; Ahlrichs, R. *Phys. Chem. Chem. Phys* **2005**, *7*, 3297-3305.
- ¹⁹ (a) Tomasi, J.; Mennucci, B.; Cammi, R. *Chem. Rev.* **105**, *8*, 2999-3094; (b) Cramer, C. J.; Truhlar, D. G. *Chem. Rev.* **1999**, *99*, 2161-2200

-
- ²⁰ Barone, V.; Cossi, M. *J. Phys. Chem. A* **1998**, *102*, 1995-2001.
- ²¹ Marenich, A. V.; Cramer, C. J.; Truhlar, D. G. *J. Phys. Chem. B*, **2009**, *113*, 6378-6396.
- ²² Klamt, A.; Schüürmann, G. *J. Chem. Soc., Perkin Trans. 2*, **1993**, 0, 799-805
- ²³ Klamt, A. *J. Phys. Chem.* **1995**, *99*, 2224-2235.
- ²⁴ Marenich, A. V.; Cramer, C. J.; Truhlar, D. G. *J. Phys. Chem. B* **2009**, *113*, 6378–6396.
- ²⁵ Marcus, R. A. *J. Chem. Phys.* **1956**, *24*, 966-978.
- ²⁶ Hospital, A.; Goñi, J. R.; Orozco, M.; Gelpí, J. L. *Adv Appl Bioinform Chem.* **2015**, *8*, 37–47.
- ²⁷ (a) Karplus, M. *Acc. Chem. Res.* **2002**, *35*, 321-323; (b) Adcock, S. A.; McCammon, J. A. *Chem. Rev.* **2006**, *106*, 1589-1615
- ²⁸ Oyola, Y.; Singleton, D. A. *J. Am. Chem. Soc.* **2009**, *131*, 3130-3131.
- ²⁹ (a) Sun, L.; Hase, W. L. *Rev. Comput. Chem.* **2003**, *19*, 79-146. (b) Black, K.; Liu, P.; Xu, L.; Doubleday, C.; Houk, K. N. *Proc. Natl. Acad. Sci. U. S. A.* **2012**, *109*, 12860-12865. (c) Hong, Y. J.; Tantillo, D. J. *Nat. Chem.* **2014**, *6*, 104-111.

-
- ³⁰ (a) Zhao, L.; von Hopffgarten, M.; Andrada, D. M.; Frenking, G. Energy decomposition analysis. *WIREs Comput. Mol. Sci.* **2018**, DOI: 10.1002/wcms.1345; (b) Von Hopffgarten, M.; Frenking, G. *Wires Comput. Mol. Sci.* **2012**, 2, 43–62; (c) Phipps, M. J. S.; Fox, T.; Tautermann, C. S.; Skylaris, C.-K. *Chem. Soc. Rev.*, **2015**, 44, 3177-3211.
- ³¹ K. Morokuma, *J. Chem. Phys.* **1971**, 55, 1236-1244.
- ³² K. Kitaura, K. Morokuma, *Int. J. Quantum Chem.* **1976**, 10, 325-340.
- ³³ (a) T. Ziegler and A. Rauk, *Inorg. Chem.*, **1979**, 18, 1558–1565; (b) T. Ziegler and A. Rauk, *Inorg. Chem.*, **1979**, 18, 1755–1759; (c) T. Ziegler and A. Rauk, *Theor. Chim. Acta*, **1977**, 46, 1–10.
- ³⁴ Glendening, E. D. *J. Am. Chem. Soc.* **1996**, 118, 2473-2482
- ³⁵ Khaliullin, R. Z.; Cobar, E. A.; Lochan, R. C.; Bell, A. T.; Head-Gordon, M. *J Phys Chem A* **2007**, 111, 8753-65.
- ³⁶ Horn, P. R.; Mao, Y.; Head-Gordon, M. *Phys Chem Chem Phys* **2016**, 18, 23067-79.
- ³⁷ Su, P.; Li, H. *J. Chem. Phys.* **2009**, 131, 014102–014115.

-
- ³⁸ (a) Lu, G.; Liu, R. Y.; Yang, Y.; Fang, C.; Lambrecht, D. S.; Buchwald, S. L.; Liu, P. *J. Am. Chem. Soc.* **2017**, *139*, 16548-16555; (b) Thomas, A. A.; Speck, K.; Kevlishvili, I.; Lu, Z.; Liu, P.; Buchwald, S. L. *J. Am. Chem. Soc.* **2018**, *140*, 13976–13984; (c) Peverati, R.; Platt, S. P.; Attah, I. K.; Aziz, S. G.; El-Shall, M. S.; Head-Gordon, M. *J. Am. Chem. Soc.* **2017**, *139*, 11923-11932; (d) Fernandez, I.; Sola, M.; Bickelhaupt, F. M. *Chem. Eur. J.* **2013**, *19*, 7416–742.
- ³⁹ Alexopoulos, E. C. *Hippokratia* **2010**, *14*, 23–28.
- ⁴⁰ (a) Sigman, M. S.; Harper, K. C.; Bess, E. N.; Milo, A. *Acc. Chem. Res.* **2016**, *49*, 1292; (b) Zhao, S.; Gensch, T.; Murray, B.; Niemeyer, Z. L.; Sigman, M. S.; Biscoe, M. R. *Science* **2018**. DOI: 10.1126/science.aat2299; (c) Z. L.; Pindi, S.; Khrakovsky, D. A.; Kuzniewski, C. N.; Hong, C. M.; Joyce, L. A.; Sigman, M. S.; Toste, F. D. *J. Am. Chem. Soc.* **2017**, *139*, 12943–12946; (d) Niemeyer, Z. L.; Milo, A.; Hickey, D. P.; Sigman, M. S. *Nat. Chem.* **2016**, *8*, 610–617.
- ⁴¹ Wu, K.; Doyle, A. G. *Nat. Chem.* **2017**, *9*, 779-784.
- ⁴² (a) Matyjaszewski, K. *Macromolecules* **2012**, *45*, 4015-4039; (b) Braunecker, W. A.; Matyjaszewski, K. *Prog. Polym. Sci.* **2007**, *32*, 93-146; (c) Matyjaszewski, K.; Tsarevsky, N. V. *J. Am. Chem. Soc.* **2014**, *136*, 6513-6533; (d) Matyjaszewski, K. *Adv. Mater.* **2018**, *30*, 1706441.
- ⁴³ (a) O'Reilly, R. K.; Shaver, M. P.; Gibson, V. C. *Inorg. Chim. Acta* **2006**, *359*, 4417-4420; (b) Zhengbiao, Z.; Wei, Z.; Xiulin, Z.; Zhenping, C.; Jian, Z. *J. Polym. Sci., Part A: Polym. Chem.* **2007**, *45*, 5722-5730; (c) Nishiura, C.; Williams, V.; Matyjaszewski, K. *Macromol. Res.*

2017, *25*, 504-512; (d) Cao, J.; Jin, C.; Keda, Z. *J. Polym. Sci., Part A: Polym. Chem.* **2005**, *43*, 2625-2631; (e) Sebastien, M.; Tadeusz, B.; Rinaldo, P.; Przemysaw, K. *J. Appl. Polym. Sci.* **2007**, *105*, 278-281; (f) Kato, M.; Kamigaito, M.; Sawamoto, M.; Higashimura, T. *Macromolecules* **1995**, *28*, 1721-1723; (g) Xue, Z.; He, D.; Xie, X. *Polym. Chem.* **2015**, *6*, 1660-1687; (h) di Lena, F.; Matyjaszewski, K. *Prog. Polym. Sci.* **2010**, *35*, 959-1021.

⁴⁴ Pan, X.; Fang, C.; Fantin, M.; Malhotra, N.; So, W. Y.; Peteanu, L. A.; Isse, A. A.; Gennaro, A.; Liu, P.; Matyjaszewski, K. *J. Am. Chem. Soc.* **2016**, *138*, 2411-2425.

⁴⁵ (a) Pan, X.; Lamson, M.; Yan, J.; Matyjaszewski, K. *ACS Macro Letters* **2015**, *4*, 192-196; (b) Treat, N. J.; Sprafke, H.; Kramer, J. W.; Clark, P. G.; Barton, B. E.; Read de Alaniz, J.; Fors, B. P.; Hawker, C. J. *J. Am. Chem. Soc.* **2014**, *136*, 16096-16101; (c) Fors, B. P.; Hawker, C. J. *Angew. Chem. Int. Ed.* **2012**, *51*, 8850-8853; (d) Pan, X.; Tasdelen, M. A.; Laun, J.; Junkers, T.; Yagci, Y.; Matyjaszewski, K. *Prog. Polym. Sci.* **2016**, *62*, 73-125.

⁴⁶ (a) Zerk, T. J.; Bernhardt, P. V. *Coord. Chem. Rev.* **2017**, *375*, 173-190; (b) Pintauer, T.; Matyjaszewski, K. *Coord. Chem. Rev.* **2005**, *249*, 1155-1184.

⁴⁷ Matyjaszewski, K.; Patten, T. E.; Xia, J. *J. Am. Chem. Soc.* **1997**, *119*, 674-680.

⁴⁸ De Paoli, P.; Isse, A. A.; Bortolamei, N.; Gennaro, A. *Chem. Commun.* **2011**, *47*, 3580-3582.

-
- ⁴⁹ Lin, C. Y.; Coote, M. L.; Gennaro, A.; Matyjaszewski, K. *J. Am. Chem. Soc.* **2008**, *130*, 12762-12774.
- ⁵⁰ (a) Gillies, M. B.; Matyjaszewski, K.; Norrby, P.-O.; Pintauer, T.; Poli, R.; Richard, P. *Macromolecules* **2003**, *36*, 8551-8559; (b) Matyjaszewski, K.; Poli, R. *Macromolecules* **2005**, *38*, 8093-8100; (c) Guliashvili, T.; Percec, V. *J. Polym. Sci., Part A: Polym. Chem.* **2007**, *45*, 1607-1618.
- ⁵¹ Isse, A. A.; Gennaro, A.; Lin, C. Y.; Hodgson, J. L.; Coote, M. L.; Guliashvili, T. *J. Am. Chem. Soc.* **2011**, *133*, 6254-6264.
- ⁵² (a) Orlandi, M.; Coelho, J. A. S.; Hilton, M. J. F.; Toste, F. D.; Sigman, M. S. *J. Am. Chem. Soc.* **2017**, *139*, 6803–6806; (b) Orlandi, M.; Hilton, M. J.; Yamamoto, E.; Toste, F. D.; Sigman, M. S. *J. Am. Chem. Soc.* **2017**, *139*, 12688–12695; (c) Morales-Rivera, C. A.; Floreancig, P. E.; Liu, P. *J. Am. Chem. Soc.* **2017**, *139*, 17935-17944.
- ⁵³ (a) Straker, R. N.; Mekareeya, A.; Paton, R. S.; Anderson, E. A. *Nat. Commun.* **2016**, *7*, 10109–10118; (b) Kwon, D.; Fuller, J. T.; Kilgore, U. J.; Sydora, O. L.; Bischof, S. M.; Ess, D. H. *ACS Catal.* **2018**, *8*, 1138–1142; (c) Nielsen, M. C.; Bonney, K. J.; Schoenebeck, F. *Angew. Chem., Int. Ed.* **2014**, *53*, 5903–5906; (d) Bernales, V.; League, A. B.; Li, Z.; Schweitzer, N. M.; Peters, A. W.; Carlson, R. K.; Hupp, J. T.; Cramer, C. J.; Farha, O. K.; Gagliardi, L. *J. Phys. Chem. C* **2016**, *120*, 23576–23583; (e) Sinha, I.; Lee, Y.; Bae, C.; Tussupbayev, S.; Lee, Y.; Seo, M.; Kim, J.; Baik, M.; Lee, Y.; Kim, H. *Catal. Sci. Technol.* **2017**, *7*, 4375–4387.

-
- ⁵⁴ Frisch, M. J.; *et al.* Gaussian 09, Revision D.01; Gaussian, Inc.: Wallingford, CT, 2009.
- ⁵⁵ Saveant, J. M. *J. Am. Chem. Soc.* **1987**, *109*, 6788–6795.
- ⁵⁶ Bickelhaupt, F. M.; Houk, K. N. *Angew. Chem. Int. Ed.* **2017**, *56*, 10070-10086.
- ⁵⁷ Ess, D. H.; Houk, K. N. *J. Am. Chem. Soc.* **2007**, *129*, 10646-10647.
- ⁵⁸ Shao, Y.; *et al.* *Mol. Phys.* **2014**, *113*, 184-215.
- ⁵⁹ (a) Giri, R.; Brusoe, A.; Troshin, K.; Wang, J. Y.; Font, M.; Hartwig, J. F. *J. Am. Chem. Soc.* **2018**, *140*, 793-806; (b) Yu, H.-Z.; Jiang, Y.-Y.; Fu, Y.; Liu, L. *J. Am. Chem. Soc.* **2010**, *132*, 18078-18091; (c) Jones, G. O.; Liu, P.; Houk, K. N.; Buchwald, S. L. *J. Am. Chem. Soc.* **2010**, *132*, 6205-6213.
- ⁶⁰ Wiberg, K. B. *Tetrahedron*, **1968**, *24*, 1083-1096.
- ⁶¹ (a) Matsubara, H.; Ryu, I.; Schiesser, C. H. *Org. Biomol. Chem.* **2007**, *5*, 3320-3324; (b) Yorimitsu, H.; Shinokubo, H.; Matsubara, S.; Oshima, K. *J. Org. Chem.* **2001**, *66*, 7776-7785; (c) Yamamoto, K.; Li, J.; Garber, J. A. O.; Rolfes, J. D.; Boursalian, G. B.; Borghs, J. C.; Genicot, C.; Jacq, J.; van Gastel, M.; Neese, F.; Ritter, T. *Nature* **2018**, *554*, 511-514.

-
- ⁶² In a recent computational study on the mechanism of Rh-catalyzed atom transfer radical addition reaction, a bent Rh...Br...C geometry in a bromide atom transfer transition state was observed: Chen, B.; Fang, C.; Liu, P.; Ready, J. M. *Angew. Chem., Int. Ed.* **2017**, *56*, 8780–8784.
- ⁶³ Liu, F.; Yang, Z.; Yu, Y.; Mei, Y.; Houk, K. N. *J. Am. Chem. Soc.* **2017**, *139*, 16650-16656.
- ⁶⁴ Tang, W.; Matyjaszewski, K. *Macromolecules* **2007**, *40*, 1858-1863.
- ⁶⁵ Fantin, M.; Isse, A. A.; Bortolamei, N.; Matyjaszewski, K.; Gennaro, A. *Electrochimica Acta* **2016**, *222*, 393-401.
- ⁶⁶ The experimental activation free energies ($\Delta G_{\text{exp}}^{\ddagger}$) were calculated using the Eyring equation: $k_{\text{act}} = \frac{k_B T}{h} e^{\frac{-\Delta G_{\text{exp}}^{\ddagger}}{RT}}$, in which k_{act} values were determined by the most recent electrochemical measurements in ref 34. See: Eyring, H. *J. Chem. Phys.* **1935**, *3*, 107-115.
- ⁶⁷ Tang, W.; Kwak, Y.; Braunecker, W.; Tsarevsky, N. V.; Coote, M. L.; Matyjaszewski, K. *J. Am. Chem. Soc.* **2008**, *130*, 10702-10713.
- ⁶⁸ Tang, W.; Matyjaszewski, K. *Macromolecules*, **2006**, *39*, 4953-4959.
- ⁶⁹ Ribelli, T. G.; Fantin, M.; Daran, J.-C.; Augustine, K. F.; Poli, R.; Matyjaszewski, K. *J. Am. Chem. Soc.* **2018**, *140*, 1525-1534.

-
- ⁷⁰ The percent buried volume ($V_{\text{bur}}\%$) values were calculated using SambVca 2. See: Falivene, L.; Credendino, R.; Poater, A.; Petta, A.; Serra, L.; Oliva, R.; Scarano, V.; Cavallo, L. *Organometallics* **2016**, *35*, 2286-2293. A radius of 5.0 Å was used to define the coordination sphere around the metal center. The larger radius is necessary to properly describe the steric properties of the *N*-donor ligands, because the substituents involved in the steric interactions (e.g. the ethyl substituents on Et₆TREN) are not directly coordinated to the metal center.
- ⁷¹ Knuehl, B.; Pintauer, T.; Kajiwar, A.; Fischer, H.; Matyjaszewski, K. *Macromolecules* **2003**, *36*, 8291-8296.
- ⁷² (a) Meyer, T. J. *Accounts of Chemical Research* **1989**, *22*, 163-170; (b) Lalrempuia, R.; McDaniel, N. D.; Müller-Bunz, H.; Bernhard, S.; Albrecht, M. *Angew. Chem. Int. Ed.* **2010**, *49*, 9765-9768; (c) DiSalle, B. F.; Bernhard, S. *J. Am. Chem. Soc.* **2011**, *133*, 11819-11821.
- ⁷³ Kalyanasundaram, K. *Coordination Chemistry Reviews* **1982**, *46*, 159-244.
- ⁷⁴ Howerton, B. S.; Heidary, D. K.; Glazer, E. C. *J. Am. Chem. Soc.* **2012**, *134*, 8324-8327.
- ⁷⁵ (a) Kärkäs, M. D.; Matsuura, B. S.; Stephenson, C. R. J. *Science* **2015**, *349*, 1285-1286; (b) Le, C. C.; MacMillan, D. W. C. *J. Am. Chem. Soc.* **2015**, *137*, 11938-11941; (c) Nawrat, C. C.; Jamison, C. R.; Slutskyy, Y.; MacMillan, D. W. C.; Overman, L. E. *J. Am. Chem. Soc.* **2015**, *137*, 11270-11273; (d) Jin, J.; MacMillan, D. W. C. *Nature* **2015**, *525*, 87-90; (e) Terrett, J. A.; Cuthbertson, J. D.; Shurtleff, V. W.; MacMillan, D. W. C. *Nature* **2015**, *524*, 330-334; f) Prier,

C. K.; Rankic, D. A.; MacMillan, D. W. C. *Chem. Rev.* **2013**, *113*, 5322-5363; (g) Romero, N. A.; Margrey, K. A.; Tay, N. E.; Nicewicz, D. A. *Science* **2015**, *349*, 1326-1330; (h) Griffin, J. D.; Zeller, M. A.; Nicewicz, D. A. *J. Am. Chem. Soc.* **2015**, *137*, 11340-11348.

⁷⁶ Fors, B. P.; Hawker, C. J. *Angew. Chem. Int. Ed.* **2012**, *51*, 8850-8853.

⁷⁷ (a) Lalevée, J.; Peter, M.; Dumur, F.; Gigmes, D.; Blanchard, N.; Tehfe, M.-A.; Morlet-Savary, F.; Fouassier, J. P. *Chem. Eur. J.* **2011**, *17*, 15027-15031; (b) Lalevée, J.; Blanchard, N.; Tehfe, M.-A.; Morlet-Savary, F.; Fouassier, J. P. *Macromolecules* **2010**, *43*, 10191-10195; (c) Ogawa, K. A.; Goetz, A. E.; Boydston, A. J. *J. Am. Chem. Soc.* **2015**, *137*, 1400-1403; (d) Xiao, P.; Zhang, J.; Dumur, F.; Tehfe, M. A.; Morlet-Savary, F.; Graff, B.; Gigmes, D.; Fouassier, J. P.; Lalevée, J. *Prog. Polym. Sci.* **2015**, *41*, 32-66; (e) Perkowski, A. J.; You, W.; Nicewicz, D. A. *J. Am. Chem. Soc.* **2015**, *137*, 7580-7583.

⁷⁸ (a) Chen, M.; MacLeod, M. J.; Johnson, J. A. *ACS Macro Lett.* **2015**, *4*, 566-569; (b) Shanmugam, S.; Xu, J.; Boyer, C. *J. Am. Chem. Soc.* **2015**, *137*, 9174-9185; (c) Shanmugam, S.; Xu, J.; Boyer, C. *Chemical Science* **2015**, *6*, 1341-1349; (d) Xu, J.; Shanmugam, S.; Duong, H. T.; Boyer, C. *Polym. Chem.* **2015**, *6*, 5615-5624; (e) Shanmugam, S.; Boyer, C. *J. Am. Chem. Soc.* **2015**, *137*, 9988-9999; (f) Yeow, J.; Xu, J.; Boyer, C. *ACS Macro Lett.* **2015**, *4*, 984-990; (g) Xu, J.; Jung, K.; Atme, A.; Shanmugam, S.; Boyer, C. *J. Am. Chem. Soc.* **2014**, *136*, 5508-5519.

-
- ⁷⁹ (a) Werner, H.-J.; Knowles, P. J.; Knizia, G.; Manby, F. R.; Schütz, M. *WIREs Comput. Mol. Sci.* **2012**, 2, 242-253. (b) MOLPRO, version 2012.1, a package of ab initio programs, <http://www.molpro.net>.
- ⁸⁰ Isse, A. A.; Gennaro, A.; Lin, C. Y.; Hodgson, J. L.; Coote, M. L.; Guliashvili, T. *J. Am. Chem. Soc.* **2011**, 133, 6254-6264.
- ⁸¹ (a) Isse, A. A.; Sandonà, G.; Durante, C.; Gennaro, A. *Electrochim. Acta* **2009**, 54, 3235-3243; (b) Costentin, C.; Robert, M.; Savéant, J.-M. *J. Am. Chem. Soc.* **2003**, 125, 10729-10739; (c) Isse, A. A.; Gennaro, A. *J. Phys. Chem. A* **2004**, 108, 4180-4186; (d) Cardinale, A.; Isse, A. A.; Gennaro, A.; Robert, M.; Savéant, J.-M. *J. Am. Chem. Soc.* **2002**, 124, 13533-13539; (e) Andrieux, C. P.; Le Gorande, A.; Saveant, J. M. *J. Am. Chem. Soc.* **1992**, 114, 6892-6904; (f) Andrieux, C. P.; Gallardo, I.; Savaent, J. M.; Su, K. B. *J. Am. Chem. Soc.* **1986**, 108, 638-647.
- ⁸² Saveant, J. M. *J. Am. Chem. Soc.* **1987**, 109, (22), 6788-6795.
- ⁸³ Saveant, J. M. *J. Am. Chem. Soc.* **1992**, 114, (26), 10595-10602.
- ⁸⁴ Rehm, D.; Weller, A. *Isr. J. Chem.* **1970**, 8, 259-271.
- ⁸⁵ Isse, A. A.; Bortolamei, N.; De Paoli, P.; Gennaro, A. *Electrochim. Acta* **2013**, 110, 655-662.
- ⁸⁶ Böes, E. S.; Livotto, P. R.; Stassen, H. *Chem. Phys.* **2006**, 331, 142-158.

-
- ⁸⁷ (a) Pan, D.; Phillips, D. L. *J. Phys. Chem. A* **1999**, *103*, 4737-4743; (b) Okamoto, T.; Kuratsu, M.; Kozaki, M.; Hirotsu, K.; Ichimura, A.; Matsushita, T.; Okada, K. *Org. Lett.* **2004**, *6*, 3493-3496.
- ⁸⁸ Marenich, A. V.; Cramer, C. J.; Truhlar, D. G. *J. Phys. Chem. B* **2009**, *113*, 6378–6396
- ⁸⁹ Among the two low energy isomers of ion pair $2^{\bullet+}\text{Br}^-$, only the covalent isomer $2^{\bullet+}\text{Br}^- \text{-C}$ is considered in the calculations of the deactivation mechanisms. Due to the weak interactions between $2^{\bullet+}$ and Br^- in the ionic isomer of the ion pair, the reactivity of $2^{\bullet+}\text{Br}^- \text{-I}$ is expected to be similar to the separated catalyst radical cation and halide anion.
- ⁹⁰ Shine, H. J.; Silber, J. J.; Bussey, R. J.; Okuyama, T. *J. Org. Chem.* **1972**, *37*, 2691-2697.
- ⁹¹ Lutz, J.-F. *Macromol. Rapid Commun.* **2017**, *38*, 1700582.
- ⁹² Swisher, J. H.; Nowalk, J. A.; Washington, M. A.; Meyer, T. Y. In *Sequence-Controlled Polymers*; Wiley-VCH Verlag GmbH & Co. KGaA: **2018**; p 435.
- ⁹³ Cole, J. P.; Hanlon, A. M.; Rodriguez, K. J.; Berda, E. B. *J. Polym. Sci., Part A: Polym. Chem.* **2017**, *55*, 191.
- ⁹⁴ Lutz, J.-F.; Lehn, J.-M.; Meijer, E. W.; Matyjaszewski, K. *Nat. Rev. Mater.* **2016**, *1*, 16024.

-
- ⁹⁵ Lutz, J.-F.; Ouchi, M.; Liu, D. R.; Sawamoto, M. *Science* **2013**, *341*, 341.
- ⁹⁶ Zhang, J.; Matta, M. E.; Hillmyer, M. A. *ACS Macro Lett.* **2012**, *1*, 1383.
- ⁹⁷ Gutekunst, W. R.; Hawker, C. J. *J. Am. Chem. Soc.* **2015**, *137*, 8038.
- ⁹⁸ Weiss, R. M.; Short, A. L.; Meyer, T. Y. *ACS Macro Lett.* **2015**, *4*, 1039.
- ⁹⁹ Short, A. L.; Fang, C.; Nowalk, J. A.; Weiss, R. M.; Liu, P.; Meyer, T. Y. *ACS Macro Lett.* **2018**, *7*, 858-862.
- ¹⁰⁰ Pepels, M. P. F.; Hansen, M. R.; Goossens, H.; Duchateau, R. *Macromolecules* **2013**, *46*, 7668.
- ¹⁰¹ (a) Song, A.; Lee, J. C.; Parker, K. A.; Sampson, N. S. *J. Am. Chem. Soc.* **2010**, *132*, 10513-10520; (b) Rowley, C. N.; van der Eide, E. F.; Piers, W. E.; Woo, T. K. *Organometallics* **2008**, *27*, 6043-6045; (c) Lopez, S. A.; Houk, K. N. *J. Org. Chem.* **2013**, *78*, 1778-1783; (d) Adlhart, C.; Chen, P. *J. Am. Chem. Soc.* **2004**, *126*, 3496-3510.
- ¹⁰² Chatterjee, A. K.; Choi, T.-L.; Sanders, D. P.; Grubbs, R. H. *J. Am. Chem. Soc.* **2003**, *125*, 11360-11370.
- ¹⁰³ Anderson, D. R.; Ung, T.; Mkrtumyan, G.; Bertrand, G.; Grubbs, R. H.; Schrodi, Y. *Organometallics* **2008**, *27*, 563-566.

-
- ¹⁰⁴ Benitez, D.; Tkatchouk, E.; Goddard Iii, W. A. *Chem. Commun.* **2008**, 0, 6194-6196.
- ¹⁰⁵ Bahri-Laleh, N.; Credendino, R.; Cavallo, L. *Beilstein J. Org. Chem.* **2011**, 7, 40-45.
- ¹⁰⁶ Case, D. A.; Darden, T. A.; Cheatham, T. E., III; Simmerling, C. L.; Wang, J.; Duke, R. E.; Luo, R.; Walker, R. C.; Zhang, W.; Merz, K. M.; Roberts, B. et al. AMBER 12; University of California: San Francisco, 2012.
- ¹⁰⁷ Wang, J.; Wolf, R. M.; Caldwell, J. W.; Kollman, P. A.; Case, D. A. *J. Comput. Chem.* **2004**, 25, 1157-1174.
- ¹⁰⁸ Bayly, C. I.; Cieplak, P.; Cornell, W.; Kollman, P. A. *J. Phys. Chem.* **1993**, 97, 10269-10280.
- ¹⁰⁹ (a) Besler, B. H.; Merz, K. M.; Kollman, P. A. *J. Comput. Chem.* **1990**, 11, 431-439; (b) Singh, U. C.; Kollman, P. A. *J. Comput. Chem.* **1984**, 5, 129-145.
- ¹¹⁰ Watts, K. S.; Dalal, P.; Tebben, A. J.; Cheney, D. L.; Shelley, J. C. *J. Chem. Inf. Model.* **2014**, 54, 2680-2696.
- ¹¹¹ Schrödinger Release 2016-4: Maestro, Schrödinger, LLC, New York, NY, 2016
- ¹¹² Schafmeister, C. E. A. F.; Ross, W. S.; Romanovski, V. LEAP; University of California, San Francisco, 1995.

-
- ¹¹³ Sagui, C.; Darden, T. A. *Annu. Rev. Biophys. Biomol. Struct.* **1999**, 28, 155-179.
- ¹¹⁴ Ryckaert, J.-P.; Ciccotti, G.; Berendsen, H. J. C. *J. Comput. Phys.* **1977**, 23, 327-341.
- ¹¹⁵ Andrea, T. A.; Swope, W. C.; Andersen, H. C. *J. Chem. Phys.* **1983**, 79, 4576-4584.
- ¹¹⁶ Curran, D. P.; Solovyev, A.; Brahmi, M. M.; Fenster-bank, L.; Malacria, M.; Lacôte, E. *Angew. Chem. Int. Ed.* **2011**, 50, 10294–10317.
- ¹¹⁷ Brown, H. C.; Zweifel, G. *J. Am. Chem. Soc.* **1960**, 82, 4708.
- ¹¹⁸ (a) Prokofjevs, A.; Boussonnière, A.; Li, L.; Bonin, H.; Lacôte, E.; Curran, D. P.; Vedejs, E. *J. Am. Chem. Soc.* **2012**, 134, 12281–12288; (b) Pan, X.; Boussonnière, A.; Curran, D. P. *J. Am. Chem. Soc.* **2013**, 135, 14433–14437; (c) Boussonnière, A.; Pan, X.; Geib, S. J.; Curran, D. P. *Organometallics* **2013**, 32, 7445–7450.
- ¹¹⁹ McFadden, T. R.; Fang, C.; Geib, S. J.; Merling, E.; Liu, P.; Curran, D. P. *J. Am. Chem. Soc.* **2017**, 139, 1726–1729.
- ¹²⁰ Taniguchi, T.; Curran, D. P. *Angew. Chem., Int. Ed.* **2014**, 53, 13150–13154
- ¹²¹ (a) Pellissier, H.; Santelli, M. *Tetrahedron* **2003**, 59, 701–730; (b) Yoshida, H.; Ohshita, J.; Kunai, A. *Bull. Chem. Soc. Jpn.* **2010**, 83, 199–219; (c) Tadross, P. M.; Stoltz, B. M. *Chem. Rev.*

-
- 2012**, *112*, 3550–3577; (d) Bhunia, A.; Yetra, S. R.; Biju, A. T. *Chem. Soc. Rev.* **2012**, *41*, 3140–3152; (e) Dubrovskiy, A. V.; Markina, N. A.; Larock, R. C. *Org. Biomol. Chem.* **2013**, *11*, 191–218.
- ¹²² Horn, M.; Mayr, H.; Lacôte, E.; Merling, E.; Deaner, J.; Wells, S.; McFadden, T.; Curran, D. P. *Org. Lett.* **2012**, *14*, 82-85.
- ¹²³ Wang, X.; Li, Y.; Wu, Y. D.; Paddon-Row, M. N.; Rondan, N. G.; Houk, K. N. *J. Org. Chem.* **1990**, *55*, 2601–2609.
- ¹²⁴ (a) Ess, D. H.; Wheeler, S. E.; Iafe, R. G.; Xu, L.; Celebi-Olcum, N.; Houk, K. N. *Angew. Chem. Int. Ed.* **2008**, *47*, 7592-7601; (b) Rehbein, J., Carpenter, B. K. *Phys. Chem. Chem. Phys.*, **2011**, *13*, 20906–20922.
- ¹²⁵ Plata, R. E.; Singleton, D. A. *J. Am. Chem. Soc.* **2015**, *137*, 3811–3826.
- ¹²⁶ Ueng, S.-H.; Fensterbank, L.; Lacote, E.; Malacria, M.; Curran, D. P. *Org. Biomol. Chem.* **2011**, *9*, 3415.
- ¹²⁷ Walton, J. C.; Brahmi, M. M.; Monot, J.; Fensterbank, L.; Malacria, M.; Curran, D. P.; Lacôte, E. *J. Am. Chem. Soc.* **2011**, *133*, 10312.